LBNL-49310

# ERNEST ORLANDO LAWRENCE BERKELEY NATIONAL LABORATORY

# Ultrafast Infrared Studies of Ligand Rearrangements at Coordinatively Unsaturated Group 6 Transition Metal Complexes

Kenneth T. Kotz

**Chemical Sciences Division**

December 2001

Ph.D. Thesis

LOAN COPY
Circulates
For 4 weeks

Library Annex
Lawrence Berkeley National Laboratory

LBNL-49310
Copy 2

**DISCLAIMER**

This document was prepared as an account of work sponsored by the United States Government. While this document is believed to contain correct information, neither the United States Government nor any agency thereof, nor The Regents of the University of California, nor any of their employees, makes any warranty, express or implied, or assumes any legal responsibility for the accuracy, completeness, or usefulness of any information, apparatus, product, or process disclosed, or represents that its use would not infringe privately owned rights. Reference herein to any specific commercial product, process, or service by its trade name, trademark, manufacturer, or otherwise, does not necessarily constitute or imply its endorsement, recommendation, or favoring by the United States Government or any agency thereof, or The Regents of the University of California. The views and opinions of authors expressed herein do not necessarily state or reflect those of the United States Government or any agency thereof, or The Regents of the University of California.

Ernest Orlando Lawrence Berkeley National Laboratory
is an equal opportunity employer.

## DISCLAIMER

This document was prepared as an account of work sponsored by the United States Government. While this document is believed to contain correct information, neither the United States Government nor any agency thereof, nor the Regents of the University of California, nor any of their employees, makes any warranty, express or implied, or assumes any legal responsibility for the accuracy, completeness, or usefulness of any information, apparatus, product, or process disclosed, or represents that its use would not infringe privately owned rights. Reference herein to any specific commercial product, process, or service by its trade name, trademark, manufacturer, or otherwise, does not necessarily constitute or imply its endorsement, recommendation, or favoring by the United States Government or any agency thereof, or the Regents of the University of California. The views and opinions of authors expressed herein do not necessarily state or reflect those of the United States Government or any agency thereof or the Regents of the University of California.

LBNL-49310

# Ultrafast Infrared Studies of Ligand Rearrangements at Coordinatively Unsaturated Group 6 Transition Metal Complexes

Kenneth Thomas Kotz
Ph.D. Thesis

Department of Chemistry
University of California, Berkeley

and

Chemical Sciences Division
Ernest Orlando Lawrence Berkeley National Laboratory
University of California
Berkeley, CA 94720

December 2001

This work was supported by the Director, Office of Science, Office of Basic Energy Sciences, Chemical Sciences Division, of the U.S. Department of Energy under Contract No. DE-AC03-76SF00098.

**Abstract**

Ultrafast Infrared Studies of Ligand Rearrangements at Coordinatively Unsaturated Group 6 Transition Metal Complexes

by

Kenneth Thomas Kotz

Doctor of Philosophy in Chemistry

University of California; Berkeley

Professor Charles B. Harris, Chair

Organometallic compounds are important reagents for synthetic transformations of silanes and are known to cleave extremely stable (~100 kcal/mol) carbon-hydrogen bonds. These reactions proceed through intermediates that contain a coordinatively unsaturated transition metal fragment. Such electron deficient fragments are highly reactive and form weakly-bound complexes with inert solvent molecules. These weakly-bound fragments rearrange to form stable products on an ultrafast time scale (ps-ns).

The ligand dynamics of silanes and alcohols at group 6 metal hexacarbonyls have been researched in detail using femtosecond infrared spectroscopy. It was

found that a previously accepted intramolecular mechanism failed to describe the rearrangement dynamics for the different systems studied in this thesis. An alternative intermolecular mechanism was proposed to describe the experimental data.

A new site-diffusion model was created in an attempt to simulate the experimental data for the rearrangement of alcohols at photogenerated coordinatively unsaturated chromium pentacarbonyl molecules. This model was based on Langevin dynamics and incorporated quantum chemical site-specific binding energies for alcohols at chromium metal complexes. It was found that the differences in binding energies between the unique chemical sites within the alcohols led to the experimentally observed dynamics.

In order to obtain better data for the reactions studied in this thesis, a new femtosecond infrared spectrometer was constructed. This system consists of a series of lasers working together to generate and amplify femtosecond laser pulses. Laser pulses at 806 nm were amplified to 400 μJ at a 2 kilohertz repetition rate. The theory, design, construction, and initial characterization of this laser are thoroughly described.

**Ultrafast Infrared Studies of Ligand Rearrangements at Coordinatively Unsaturated Group 6 Transition Metal Complexes**

Copyright © 2001

by

Kenneth Thomas Kotz

The submitted manuscript has been authored by a contractor of the U.S. Government under contract No. DE-AC03-76SF00098. Accordingly, the U.S. Government retains a nonexclusive royalty-free license to publish or reproduce the published form of this contribution, or allow others to do so, for U.S. Government purposes.

# Table of Contents

**List of Figures** ..... v

**List of Tables** ..... ix

**Acknowledgements** ..... xi

**1 Introduction** ..... 1

1.1 Thesis overview ..... 1

**2 Femtosecond Infrared Studies of Ligand Rearrangement Reactions Involving Group 6 Transition Metal Carbonyls** ..... 4-44

2.1 Introduction ..... 4

2.2 Experimental ..... 10

2.2.1 Sample Handling ..... 10

2.2.2 Data Collection ..... 11

2.2.3 Data Analysis ..... 14

2.3 Results ..... 15

2.3.1 Metal Hexacarbonyls in Silanes ..... 15

2.3.2 $(\eta^6\text{-}C_6H_6)Cr(CO)_3$ in Triethylsilane .. 28

2.3.3 $Cr(CO)_6$ in Alcohols ..... 29

2.4 Discussion ..... 33

2.4.1 Metal Carbonyl Spectra ..... 33

2.4.2 Metal Carbonyl Kinetics ..... 35

2.4.3 Chain-Walk Mechanism ..... 36

2.4.4 Rearrangement Dynamics ..... 40

**3 A Brownian Dynamics Simulation of the Rearrangement of Ligands at Coordinatively Unsaturated Transition Metal Complexes** ..... 45-87

3.1 Introduction ..... 45

3.2 Basic Theory ..... 51

3.3 Site-specific Binding Energies ..... 54

3.3.1 Computational Details ..... 55

3.3.2 Characterization of the Computational Methods ..... 56

3.3.3 The $(CO)_5Cr$…(alcohol) Interaction Energy ..... 60

3.4 Simulation Engine ..... 62

3.4.1 Rearrangement Potential ..... 62

3.4.2 Numerical Integration of Langevin's Equation ..... 65

3.4.2 Simulation Parameters ..... 66

3.5 Simulation Results ..... 71

3.6 Discussion ..... 78

3.7 Conclusions and Future Development of the Model ..... 85

**4 Design and Construction of a Femtosecond Ti:Sapphire Laser System.** ..... 88-140

4.1 Introduction ..... 88

4.2 Ti:Sapphire Femtosecond Oscillator..... 92

4.2.1 Alignment of the Ti:Sapphire Oscillator..... 95

4.3 Pulse Stretcher and Compressor..... 98

4.3.1 Alignment and Optimization of the Compressor..... 107

4.3.2 Theoretical Considerations for Stretcher/Compressor Performance.. 108

4.4 Nd:YAG Pump Laser..... 110

4.4.1 Daily Operation..... 114

4.4.2 Cavity Alignment..... 116

4.4.3 Pumping Chamber Modifications..... 121

4.5 Ti:Sapphire Regenerative Amplifier..... 123

4.5.1 Cavity Alignment..... 127

4.5.2 Electronic Timing..... 133

4.6 Laser Performance..... 136

4.7 Conclusions..... 138

**Appendix Computer Code for the Brownian Motion Ligand Rearrangement Simulation.**..... 140-170

A1.1 Simulation Engine..... 140

A1.2 Differences in Code..... 162

A1.2.1 Generation of the Potential Energy Surface..... 163

A1.2.2 Calculating Hopping Statistics... 164

A1.3 Work-up of the Simulation Data..... 167

A1.4 Characterization of the Simulation Engine167

**References.** ..... 171-192

## List of Figures

Figure 2.1 Transient difference spectra in the CO stretching region for $Mo(CO)_6$ in neat triethylsilane at 13, 33, 66, 290, and 660 ps following 295 nm UV photolysis. ..... 18

Figure 2.2 Reaction sequence for metal hexacarbonyls following photodissociation of CO in neat triethylsilane solution ..... 19

Figure 2.3 Transient difference spectra in the CO stretching region for: (a) $Cr(CO)_6$ in triethylsilane; (b) $\eta^6$-$(C_6H_6)Cr(CO)_3$ in triethylsilane; and (c) $W(CO)_6$ in triethylsilane.21

Figure 2.4 Ultrafast kinetics of $Mo(CO)_6$ in neat triethylsilane after 295 nm UV photolysis. 25

Figure 2.5 Comparison of the ultrafast kinetics of the alkyl solvate $Cr(CO)_5$ in neat triethylsilane and in neat tri-n-propylsilane after 295 nm UV photolysis. ..... 26

Figure 2.6 Transient difference spectra in the CO stretching region for $Cr(CO)_6$ in neat 1-hexanol (solid gray line) at 1.65, 16.5, 33, 99, and 297 ps following 295 nm photolysis. ..... 30

Figure 2.7 Transient difference spectra in the CO stretching region for $Cr(CO)_6$ in neat 1-propanol (solid gray line) and 2-propanol (dotted black line) at 10, 33, 66, 198, and 660 ps following 295 nm photolysis. .... 32

Figure 2.8 Scheme of the chain-walk mechanism adapted to silanes. ..... 38

Figure 2.9 Scheme summarizing dissociative rearrangement at a coordinatively unsaturated transition metal center. ..... 41

Figure 3.1 An intramolecular rearrangement reaction mechanism for 1-propanol at $Cr(CO)_5$..... 47

Figure 3.2 A dissociative rearrangement reaction mechanism for 1-propanol at $Cr(CO)_5$..... 48

Figure 3.3 A schematic representation of the site-diffusion model. ..... 50

Figure 3.4 Symmetric double-well potential used to test the simulation engine ..... 52

Figure 3.5 Multi-site cosine potential for 1-propanol given in equation 2.6. ..... 69

Figure 3.6 Simulation decay traces and fits to the Williams-Watts fitting function for the alcohols: 1-propanol, 2-propanol, and ethanol. ..... 73

Figure 3.7 Picosecond infrared kinetics of $Cr(CO)_5$ in ethanol(top), 2-propanol(middle), and 1-propanol(bottom). ..... 75

Figure 3.8 Rearrangement times for 2-propanol versus average barrier height. ..... 79

Figure 3.9 Scheme demonstrating the scaling of the alcohol potentials. ..... 80

Figure 4.1 Overview of the solid-state femtosecond laser system. ..... 91

Figure 4.2 Femtosecond Ti:sapphire oscillator. .... 93

Figure 4.3 Telescopic grating stretcher. ..... 102

Figure 4.4 Grating pulse stretcher. ..... 103

Figure 4.5 Grating pulse compressor. ..... 106

Figure 4.6 Intra-cavity doubled Nd:YAG laser ..... 111

Figure 4.7 LBO crystal housing. ..... 115

Figure 4.8 Nd:YAG laser housing modifications. ... 122

Figure 4.9 Ti:sapphire regenerative amplifier. ... 124

Figure 4.10 Electronic connections. ..... 134

Figure 4.11 Pulse timing diagram. ..... 134

Figure 4.12 Laser output spectra after: oscillator, compressor, and unseeded regen. ..... 137

Figure A.1 Barrier crossing rate versus viscosity for the potential given in equation, A.1. . 169

Figure A.2 Williams-Watts function parameters with errorbars: $\tau$, and $\beta$, versus integration step-size for single-site methanol rearrangement runs. ..... 170

## List of Tables

Table 2.1 Fitted spectral positions. ..... 17

Table 2.2 Kinetic parameters for fits to equation 1.1. ..... 24

Table 3.1 B3LYP energies (kcal/mol) for the reaction: $M(CO)_5$ + (Solvent) → $M(CO)_5$(Solvent) at various correction levels. ..... 57

Table 3.2 MP2 energies (kcal/mol) for the reaction: $M(CO)_5$ + (Solvent) → $M(CO)_5$(Solvent) at various correction levels ..... 58

Table 3.3 Comparison of calculated binding energies (kcal/mol)of $W(CO)_5$(solvent) with previous work. ..... 59

Table 3.4 MP2 energies (kcal/mol) for the reaction: $M(CO)_5$ + (Alcohol) → $M(CO)_5$(Alcohol) at various correction levels ..... 61

Table 3.5 Parameters used in the simulation runs. 67

Table 3.6 Fits to the experimental femtosecond infrared data for the photolysis of $Cr(CO)_6$ in alcohols. ..... 76

Table 3.7 Williams-Watts fitting parameters from the stochastic simulations of the Cr(CO)5alcohol systems. ..... 81

Table 4.1 Optics legend for the Ti:sapphire oscillator ..... 93

Table 4.2 Optical path lengths for the Ti:sapphire oscillator ..... 93

Table 4.3 Optics legend for the grating pulse stretcher. ..... 103

Table 4.4 Optics legend for the grating pulse compressor. ..... 106

Table 4.5 Optics legend for the intra-cavity doubled Nd:YAG laser. ..... 111

Table 4.6 Optical path lengths for the intra-cavity doubled Nd:YAG laser. ..... 111

Table 4.7 Optics legend for the Ti:sapphire amplifier. ..... 124

Table 4.8 Optical path lengths for the Ti:sapphire regenerative amplifier. ..... 124

Table 4.9 Laser output parameters. ..... 137

## Acknowledgements

Many people have helped me during my years as a graduate student at Berkeley. First, I would like to thank my advisor, Charles Harris, for accepting me into his group. Next, I must thank Vijaya Narasimhan for all her help with the administrative challenges at Berkeley. I would like to thank all the former students and post-docs that I have worked with in the group. I would especially like to thank Haw Yang for all of his support and help with the research projects that appear in this thesis. He started the work that led to the second chapter in this thesis. Lastly, I would like to thank the National Science Foundation and LBL (Office of Basic Energy Science, Chemical Science Division, U.S. Department of Energy, Contract #DE-AC03-76SF00098) for funding my research at Berkeley.

# Chapter 1

# Introduction

## 1.1 Thesis Overview

Infrared spectroscopy is a powerful tool for both the quantitative and qualitative analysis of chemical compounds. The evolution of time-resolved infrared spectroscopy into the femtosecond domain has allowed researchers to directly study the primary events of chemical reactions in solution. The results from such studies can be used to determine a complete microscopic picture of a chemical reaction. In the past, our group has studied a wide range of chemical reactions with femtosecond infrared spectroscopy, including the mechanisms for C-H and Si-H bond cleavage by transition metal complexes[1-3]. In these studies, it was found that ligand dynamics at the transition metal center contributed significantly to the observed reaction mechanism.

The unanswered questions regarding ligand dynamics resulting from the bond activation studies have led to

the current work presented in this thesis. Chapter 1 contains the majority of the experimental work carried out in order to understand the detailed mechanism for the rearrangement of ligands at group 6 transition metal carbonyls[4]. In this chapter, a series of studies are presented in which the rearrangement of silanes and alcohols at coordinatively unsaturated group 6 transition metal complexes was studied using our ultrafast infrared spectrometer. This chapter thoroughly discusses the possible mechanisms for ligand rearrangement in these different systems.

In order to understand the processes involved in the rearrangements discussed in chapter 1, a new site-diffusion model was constructed and is presented in chapter 2. This model describes the rearrangement of ligands, specifically alcohols, at coordinatively unsaturated complexes as a diffusion process through a fluid of binding sites. The sites correspond to the different bonds of the alcohol to which a transition metal fragment can form a meta-stable intermediate in solution, e.g. the different C-H bonds along the alkyl chain of the alcohol. Because the binding energies of these intermediates are low, the lifetimes for these

complexes are short (50 ps-1 ns), and thus quantum chemical calculations are employed in order to provide site-specific details for binding energies that are used in the diffusion model. The results from this model are compared to the experimental data, and future developments of the rearrangement model are discussed.

Lastly, this thesis outlines the construction of a new femtosecond spectrometer in our laboratory based entirely on solid-state laser technologies. Solid-state lasers have many advantages over older dye-based systems[5]. These advantages, as well as the detailed design, construction, and operation of this laser are presented in the final chapter of this thesis.

# Chapter 2

# Femtosecond Infrared Studies of Ligand Rearrangement Reactions Involving Group 6 Transition Metal Carbonyls

## 2.1 Introduction

Hydrosilation is an important synthetic reaction for the generation of substituted silane molecules. Transition metal complexes are known to catalyze these reactions, often with silyl hydrides postulated as intermediates in this process[6-8]. Recent studies have shown that similar weakly-bound complexes between reactive transition metal complexes and solvent molecules play a role in the product formation of oxidative reactions[1, 9]. Group 6 metal carbonyls are known to catalyze the hydrosilation of alkenes. This makes them ideal candidates for studying the processes involved in such chemical reactions. Understanding the chemical physics behind the solvation and evolution of such silyl hydride intermediates is an important goal towards

understanding the general reactivity of hydrosilation transformations.

The detailed photochemistry of Group 6 metal carbonyls is well known[10]. Following irradiation by ultra-violet (UV) light, the ground state molecule is promoted into a carbonyl dissociative state. In solution, one CO ligand is lost within 400 fs[11-13]. Surrounding molecules solvate the unsaturated metal fragment within 1-2 ps[14, 15]. The metal-CO bond strength of these systems is typically about 35-45 kcal/mol[16], whereas the UV photons used in photolysis studies typically have ~100 kcal/mol. The excess 55-65 kcal/mol of energy that the excited unsaturated metal fragments contain is then dissipated to the solvent in tens to hundreds of picoseconds following CO dissociation[17]. The initial solvation of the bare metal fragment happens well before equilibrium of the chemical system has been established. In solutions which contain different types of ligands that can bind the unsaturated metal center, the structure of the initial solvation-complex that forms is dictated only by the statistical nature of the solvation process, not the thermodynamics of the equilibrated system. This initial

kinetic product rearranges to form the thermodynamic product on a time scale dictated by the rearrangement process itself.

Simon and co-workers studied this rearrangement process in detail for the initial coordination of alcohols with photogenerated $Cr(CO)_5$[14, 15, 18, 19]. In their system, photolysis of $Cr(CO)_6$ in neat alcohols produced pentacarbonyl fragments that coordinated to either the oxygen or the C-H bonds of the alcohol. The weaker alkyl complex rearranged over hundreds of picoseconds to form the more stable O-H bound complex. They proposed an intramolecular mechanism that accounted for the rearrangement dynamics of this process[19]. In this mechanism, the initial C-H complex rearranges through random walks along the alkyl backbone until the metal center encounters the strongly binding hydroxyl site. This "chain-walk" model seemed to accurately describe the rearrangement for many different alcohols. Their observations, however, were made in the visible region of the spectra where broad linewidths and complicated Frank-Condon overlap factors make it difficult to ascertain the exact structural nature of the reactive intermediates.

Other groups have also studied this rearrangement process. Using photoacoustic calorimetry (PAC), Burkey determined the bonding enthalpies of $M(CO)_5$ (M = Cr, Mo, and W) with alkanes and silanes[20]. He concluded that the pentacarbonyl-silane complexes are about twice as strong as that of alkane complexes. Dobson and co-workers have extensively studied the process of ligand rearrangement at unsaturated metal centers using PAC and UV-Visible (UV-Vis) flash photolysis techniques[21-30]. These researchers have recently concluded that the rearrangement of ligands at a $Cr(CO)_5$ center is most likely an intermolecular process, thus raising doubts as to the validity of the chain-walk mechanism[28]. Both the PAC experiments and the flash photolysis studies, however, lacked sufficient time resolution to observe the initial solvation and the subsequent rearrangement process immediately following CO dissociation on the picosecond time scale. With these restrictions, it was not possible to examine the microscopic role of the solvent in such rearrangement processes. It was also beyond the means of these researchers to examine the mechanism of rearrangement when it takes place on a time

scale comparable with energy relaxation of the non-equilibrated system.

It is well known that the infrared (IR) absorbances of metal carbonyls are strongly affected by changes in electronic structure at the transition metal center. Femtosecond time-resolved IR (fs-TRIR) absorption experiments on metal carbonyls have recently appeared in the literature[3, 11, 31-41]. The spectroscopic information contained in fs-TRIR spectroscopy allows direct measurement of ultrafast processes with a structurally sensitive probe. With the fs-TRIR technique, processes such as vibrational relaxation and ligand rearrangement can be unambiguously assigned following CO dissociation. Recent experiments carried out by Yang et al. have used ultrafast transient IR pulses to monitor the rearrangement of triethylsilane with the highly reactive 16-electron transition metal fragments, $(\eta^5\text{-}C_5H_5)M(CO)_2$ (M = Mn and Re)[3, 35]. In these experiments, the manganese and rhenium complexes were photogenerated from the tricarbonyl species $(\eta^5\text{-}C_5H_5)M(CO)_3$ (M = Mn and Re) and were initially solvated by the ethyl C-H bonds or the silyl Si-H bond. An excited triplet state was observed for the 16-electron

manganese dicarbonyl. The solvated manganese and rhenium dicarbonyls then rearranged from the alkyl solvated species to the stable silane adducts on nanosecond and microsecond time scales, respectively, via an intermolecular dissociative mechanism. Thus, competitive solvation led to different time scales for silyl hydride formation. These complex reaction pathways were elucidated by comparing the chemistry of two different group 7 complexes and through the use of ab initio methods to aid in the identification of intermediates and binding energies.

We have carried out a series of experiments in order to address the issues related to intermediate formation by highly reactive group 6 metal carbonyls. We have carefully studied the solvation of highly reactive 16-electron transition metal complexes and the formation of silyl-metal hydride complexes. To this end, we have fully examined Simon's alcohol solvation experiments, and our results provide new insights into the ligand dynamics for $Cr(CO)_5$. We have also studied the rearrangement dynamics for the series of metal carbonyls $M(CO)_6$ (M = Cr, Mo, and W) irradiated in triethylsilane. Our data suggest an intermolecular rearrangement, confirming the

results of Dobson and co-workers. Furthermore, the ligand dynamics for the group 6 metal complexes were remarkably similar, despite differences in binding energetics of the token ligands.

## 2.2 Experimental

Details of the experiment and chemical handling procedures have appeared elsewhere in the literature[2, 11]. In the sections that follow, only brief details particular to the systems studied herein are given.

### 2.2.1 Sample Handling

Metal hexacarbonyls, $M(CO)_6$ (M = Cr, Mo W), were purchased from Pressure Chemicals and were used without further purification. Benzene chromium tricarbonyl $(\eta^6\text{-}C_6H_6)Cr(CO)_3$ (98%) was purchased from Strem chemicals and was used without further purification. The solvents pentane (99% spectrophotometric grade) and hexanes (98.5% spectrophotmetric grade) were purchased from Aldrich, triethylsilane and tri-n-propylsilane were both purchased from Gelest. No differences were observed between experiments carried out in $Et_3SiH$ purchased from Gelest and those that were performed in $Et_3SiH$ that had been dried over an alumina column and distilled in an inert

atmosphere of nitrogen. Furthermore, previous studies of metal hexacarbonyls that were carried out in spectrophotometric grade alkanes purchased from manufacturers showed no signs of contamination due to handling under ambient conditions[11].

The metal carbonyl solutions were prepared with a concentration between 3 and 20 mmol and were placed in a demountable liquid IR flow cell (Harrick Scientific Corp.) fitted with $CaF_2$ windows. The flow cell thickness and the sample concentration were adjusted in order to optimize the signal arising from the transient species of interest. Samples purity was assessed regularly using static FTIR, and samples were changed periodically in order to ensure sample purity.

### 2.2.2 Data Collection

As mentioned above, the femtosecond IR laser system used in these studies has been previously described in detail. Briefly, the output from an 80 MHz Titanium:sapphire oscillator was amplified in two Bethune-cell dye amplifiers that were pumped by a 30 Hz Nd:YAG laser (Quanta-Ray GCR)[42]. These pulses were split into three lines. The first of these pulses was amplified in one Bethune-cell to a final energy of 5 μJ.

The other two lines were separately focused into sapphire windows generating white light continuum. From this white light, wavelengths for final amplification were selected by the appropriate band-pass filters each having a 10 nm full width at half maximum (FWHM). In these experiments, one pulse was selectively amplified at 590 nm in a three-stage Bethune-cell amplifier chain. This pulse was then sent through a variable delay line before being frequency doubled, producing ~6 μJ, 200 fs pulses, centered at 295 nm. The second pulse, centered at 690 nm, was similarly amplified to a final energy of 25 μJ. This latter pulse, along with the 800 nm pulse were difference frequency mixed by focusing into a $LiIO_3$ crystal, producing 80 fs pulses of ~1 μJ, tunable between 1800 $cm^{-1}$ and 2300 $cm^{-1}$.

The UV pulses were focused to a ~200 μm spot into the sample in order to initiate the chemical reactions. The IR pulses were split into a signal and a reference beam. Subsequent reaction dynamics were monitored by the IR signal pulse. The maximum time delay between the pump pulse and the probe pulse was limited to 700 ps by the length of the translation stage. To make sure that all signals were due to population dynamics, the pump and

probe pulse polarizations were set at the magic angle (54.7°) in all of these experiments. Both IR beams were then focused into an astigmatism-corrected spectrographic monochrometer (spectra-Pro-150, Acton Research Corp., 150 grooves/mm, 4.0 μm blazed). The dispersed pulses were imaged onto a focal-plane-array (FPA) detector (Talktronics, Inc.), which consists of a 256x256-element HgCdTe diode array (Ratheon Amber Co.). The frequency-dispersed images were digitized within two separate windows of 12x200 pixels on this diode array, allowing simultaneous normalization of a 170 nm wide spectrum. The data for the alcohol experiments that follow were recorded with an older data collection scheme[11]. Briefly, the IR pulses were split into a signal and a reference beam. Both the signal beam and the reference beam were then focused into a monochromator (CVI DK-240) and received by a pair of matched, liquid-nitrogen-cooled, HgCdTe detectors (Electro Optical Systems). The time-resolved IR spectra were collected by scanning the monochromator while fixing the time delay between the pump and the probe pulses. The kinetic traces were acquired by setting the monochromator at the desired wavelengths while varying the delay between pump and

probe. The typical spectral and temporal resolutions for this setup are 4 $cm^{-1}$ and 300 fs, respectively. A broad, frequency independent background signal due to the $CaF_2$ windows was subtracted from all of the transient spectra.

### 2.2.3 Data Analysis

Repeated measurements were used to obtain errors for the individual spectral points. The spectral points with errors were fit for each individual time slice to a sum of voight functions by a chi-squared fitting function. The errors for each peak were determined with a Monte-Carlo Bootstrap fitting procedure in which 200 simulated data sets were used to obtain error estimates[43-45]. The widths of the peaks did not significantly contribute to the dynamics of the integrated peak intensities within the error of the fitting procedure. The peak amplitudes were therefore used in the kinetic analysis of the population dynamics. The spectra at early times ($\Delta t < 14$ ps) could not be accurately fit because the peaks are very broad and featureless. For these early times, the amplitudes centered at later peak positions were used as kinetic points.

The kinetics at each spectral peak were fit to the function:

$$A(t) = c_0 + \sum_{i=1}^{N} c_i e^{-a_i t} \qquad 2.1$$

Where $A(t)$ is the recorded signal at time delay $t$ and $c_i$ and $a_i$ are constants. The number of exponential functions, $N$, was determined by the exact kinetic behavior for each individual peak, and will be described later in the text. The fitting function used was again a chi-squared fit using the fitted amplitudes and their associated errors. A numerical simplex algorithm written for Matlab was used to find the best fits, and the errors associated with the kinetic parameters were calculated based on standard procedures[43, 44].

## 2.3 Results

In the figures which appear below, the observed spectral changes the CO stretching region were recorded as difference spectra in which negative bands indicate depletion of parent molecules, while positive bands show the appearance of new chemical species.

### 2.3.1 Metal Hexacarbonyls in Silanes

The spectra for each of the different metal carbonyls, $M(CO)_6$ (M = Cr, Mo, or W), all have similar spectral features. The static IR spectra for the

different hexacarbonyls exhibit an intense $T_{1u}$ CO stretching band at 1987 $cm^{-1}$, 1989 $cm^{-1}$, and 1983 $cm^{-1}$ for chromium, molybdenum, and tungsten, respectively. Following UV irradiation, the static FTIR spectra of the individual hexacarbonyls exhibit two new stretching bands red shifted with respect to the parent $T_{1u}$ band. The two new bands arise from the A and E symmetry CO stretches of the pentacarbonyl silyl hydride complexes that have local $C_{4v}$ symmetry at the metal center. The peak positions can be found in table 2.1 and will be discussed below. The fs-TRIR transient absorption spectra following UV excitation for $Mo(CO)_6$ in triethylsilane are shown in figure 2.1. These spectra contain features that are present in all of the metal carbonyl systems studied in this chapter and will be used as a representative example of the time-resolved spectral behavior of these systems.

There are five salient features in which appear in the individual spectra of figure 2.1. The presence of each of these features can be attributed to the different pentacarbonyl molecules shown in figure 2.2. These pentacarbonyl fragments have approximate $C_{4v}$ symmetry and exhibit two carbonyl stretching bands of A and E symmetry, respectively. Because the silicon-hydrogen

| Compound | Ligand[a] | Band | Position ($cm^{-1}$)[b] |
|---|---|---|---|
| $Cr(CO)_5L$ | L=Et-$SiHEt_2$ | E(v=0→1) | 1955 |
| | | E(v=1→2) | 1945 |
| | | A(v=0→1) | 1938 |
| | L=$SiHEt_3$ | E(v=0→1) | 1951 |
| | | A(v=0→1) | 1947 |
| | L=n-PrSiH$(Pr)_2$ | E(v=0→1) | 1947 |
| | | A(v=0→1) | 1920 |
| | L=SiH$(n\text{-}Pr)_3$ | E(v=0→1) | 1940 |
| | | A(v=0→1)[c] | Not Resolved |
| $Mo(CO)_5L$ | L=Et-$SiHEt_2$ | E(v=0→1) | 1963 |
| | | E(v=1→2) | 1947 |
| | | A(v=0→1) | 1925 |
| | L=$SiHEt_3$ | E(v=0→1) | 1956 |
| | | A(v=0→1) | 1934 |
| $W(CO)_5L$ | L=Et-$SiHEt_2$ | E(v=0→1) | 1953 |
| | | E(v=1→2) | 1945 |
| | | A(v=0→1) | 1935 |
| | L=$SiHEt_3$ | E(v=0→1) | 1950 |
| | | A(v=0→1)[c] | Not Resolved |
| $(\eta^6\text{-}C_6H_6)Cr(CO)_2L$ | L=CO | E(v=0→1) | 1913 |
| | | E(v=1→2) | 1887 |
| | L=$(Et_3SiH)$[c] | A(v=0→1) | 1870 |

[a] Complexation to the unsaturated metal center occurs through the functional group at the beginning of the ligand description

[b] Uncertainties of ± 2$cm^{-1}$

[c] The alkyl and silyl bands could not be resolved for this peak.

**Table 2.1** Fitted spectral positions.

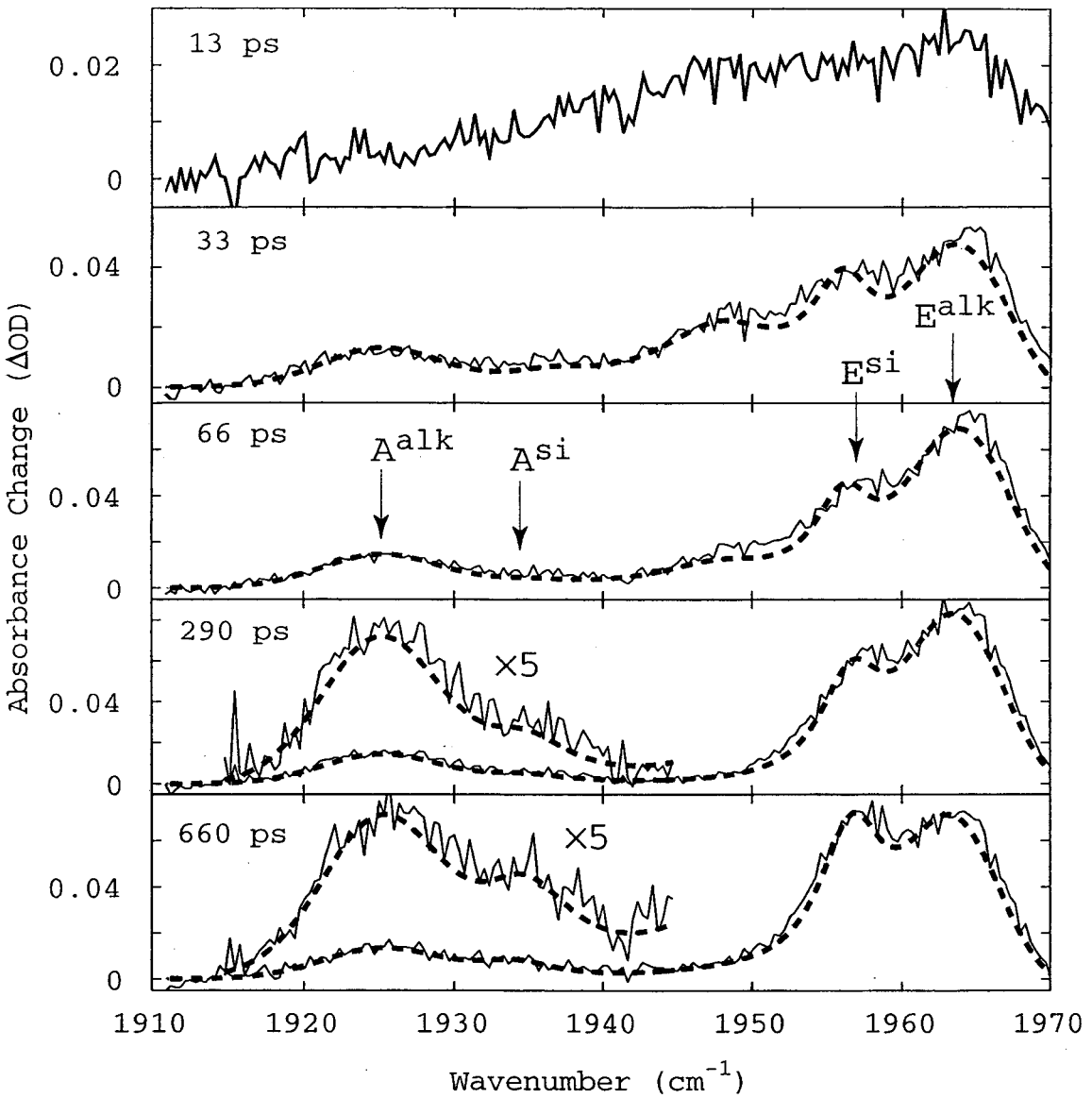


**Figure 2.1** Transient difference spectra in the CO stretching region for $Mo(CO)_6$ in neat triethylsilane at 13, 33, 66, 290, and 660 ps following 295 nm UV photolysis. The A and E CO stretching bands of the alkyl solvate or silyl adduct of $Mo(CO)_5$ are labeled. The fit of the data to equation 2.1 appears as a dashed line.

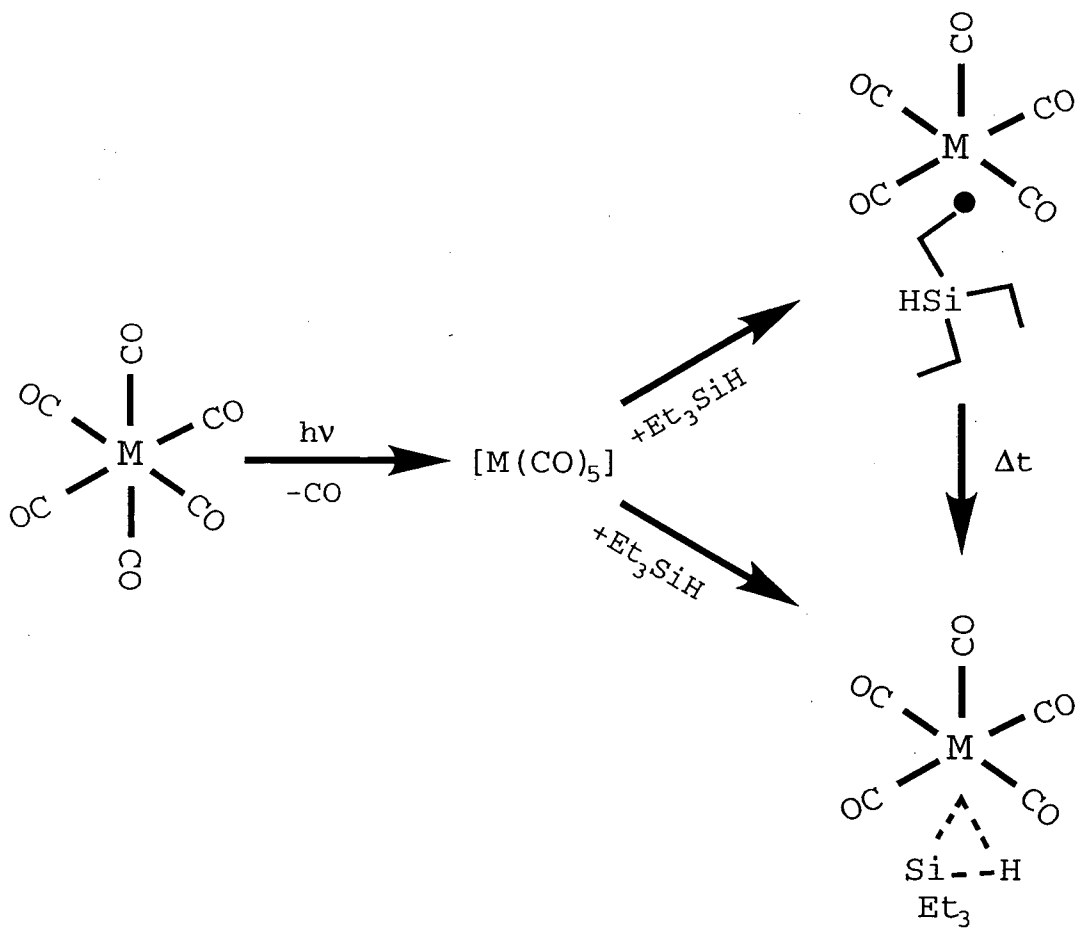


**Figure 2.2** Reaction sequence for metal hexacrbonyls following photodissociation of CO in neat triethylsilane solution.

bond is a better electron donor than the carbon-hydrogen bond, the E and A bands of the silyl complex typically appear frequency shifted with respect to those of the alkyl complex. In the ultrafast spectra of figure 2.1, the alkyl and silyl E bands, labeled $E_{alk}$ and $E_{sil}$ respectively, are more intense and appear to the blue of the alkyl and silyl A bands, labeled $A_{alk}$ and $A_{sil}$. The silyl E band appears as a shoulder on the red edge of the alkyl E band, whereas the silyl A band appears on the blue edge of the alkyl A band. There is also a feature that appears between the E and the A bands at early time delays between pump and probe. This feature decays away within 100 ps. Based on similar results from Heilweil et al., it is assigned to the hot band transition $\nu=1\rightarrow2$ of the alkyl E band[39-41, 46]. Two of the systems studied exhibited slight deviations from spectral behavior observed in the molybdenum spectra of figure 2.1. In the case of tungsten hexacarbonyl dissolved in triethylsilane, the silyl A and alkyl A bands could not be resolved from one another. This was also true for the A bands of $Cr(CO)_5$ in tri-n-propylsilane. Representative spectra for the discrepancies described above for two systems appear in figure 2.3.

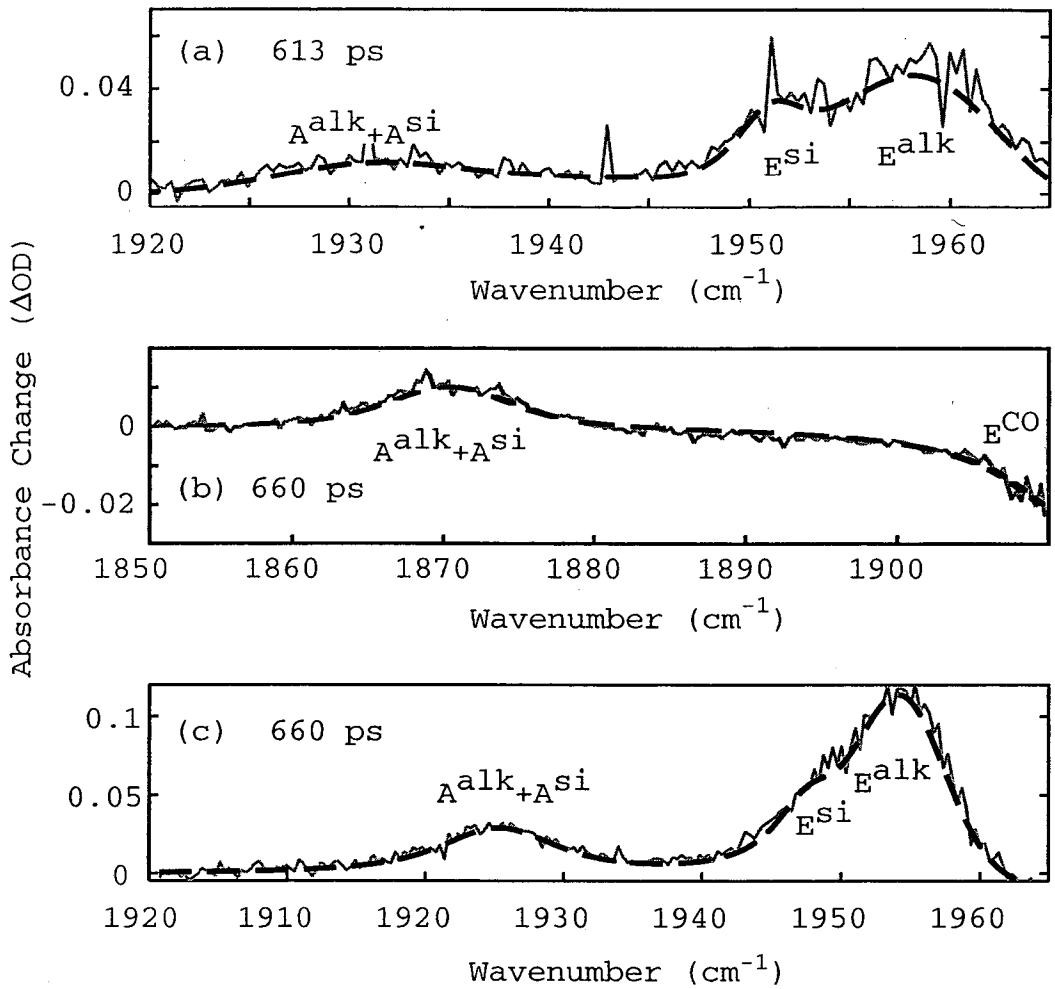


**Figure 2.3** Transient difference spectra in the CO stretching region for: (a) $Cr(CO)_6$ in triethylsilane; (b) $\eta^6$-$(C_6H_6)Cr(CO)_3$ in triethylsilane; and (c) $W(CO)_6$ in triethylsilane. The time delay between 295 nm UV pump and IR probe is shown for each window. The observed CO stretching bands of the products are labeled. The fit of the data to equation 2.1 appears as a dashed line.

The fitted peak positions and peak assignments for the features that appear in the different fs-TRIR transient spectra are compiled in table 2.1. The assignments for the $M(CO)_5$ (M = Cr, Mo, W) silyl E bands are based on literature values for similar silyl complexes[20]. The alkyl band assignments, including the hot band assignments, for all of the metal systems are found to agree with values reported in the literature for pentacarbonyls generated in neat alkanes[39]. The assignments for the silyl A bands of the pentacarbonyl complexes are based on analogy to the A alkyl bands.

The amplitudes for each of the spectral peaks in table 2.1 were fit to equation 2.1. The kinetic behavior of the individual peaks showed remarkable similarity amongst the different metal systems. The alkyl A and E bands for each of the metals were fit to a single growth on the picosecond time scale followed by a decay on the nanosecond time scale. The alkyl E hot bands were fit to a fast growth followed by a fast decay, both on the picosecond time scale. The numbers obtained from this latter decay, as well as the numbers obtained from the growth of the A and E bands were consistent with vibrational relaxation times for these systems[39, 46].

The silyl E bands exhibited bi-exponential growth. The first component was on the picosecond time scale, and again was indicative of fast vibrational relaxation. The second component was on the nanosecond time scale. A summary of the fitted parameter values can be found in table 2.2.

The kinetics for the $Mo(CO)_5$-triethylsilane alkyl and silyl E bands appear in figure 2.4. The alkyl A band exhibits an initial fast rise of 44 ps followed by a 1.6 ns decay. The silyl E band exhibits an initial rise of 22 ps, which is followed by a longer growth component of 2 ns. The similarity between the slow decay of alkyl band and the slow growth of the silyl band strongly suggests that these species are kinetically linked. This kinetic link is seen for all of the hexacarbonyl systems studied in this paper and reflects the interconversion between the alkyl and silyl complexes, on a nanosecond time scale. The kinetic traces for the chromium and tungsten complexes are similar to the molybdenum kinetics. Shown in figure 2.5, are the alkyl E band kinetics for $Cr(CO)_6$ dissolved in triethylsilane and tri-n-propylsilane. As can be seen in the figure, the two peaks decay with approximately the same rate.

| Metal Carbonyl | Ligand[a] | Band | Kinetic Description[b] | Fast Component Lifetime (ps) | Slow Component Lifetime (ns) |
|---|---|---|---|---|---|
| $Cr(CO)_5L$ | L=Et-$SiHEt_2$ | E(v=0→1) | Rise/Decay | 19 ± 2 | 4 ± 1 |
| | | E(v=1→2) | Rise/Decay[c] | | |
| | | A(v=0→1) | Rise/Decay | 19 ± 2 | 2.3 ± 0.8 |
| | L=$SiHEt_3$ | E(v=0→1) | Growth | <5[c] | 2.3 ± 10 |
| | | A(v=0→1) | Decay/Growth | 15 ± 3 | 4.3 ± 27 |
| | L=n-PrSiH(n-Pr)$_2$ | E(v=0→1) | Rise/Decay | 45 ± 5 | 2.4 ± 5 |
| | | A(v=0→1) | Rise/Decay | 50 ± 30 | 2.4 ± 1.1 |
| | L=SiH(n-Pr)$_3$ | E(v=0→1) | Growth | 60 ± 12 | 3 ± 11 |
| | | A(v=0→1) | Not Resolved | | |
| $Mo(CO)_5L$ | L=Et-$SiHEt_2$ | E(v=0→1) | Rise/Decay | 44 ± 8 | 1.6 ± 0.3 |
| | | E(v=1→2) | Rise/Decay | 15.6 ± 1.3 | 0.0296 ± 0.0012 |
| | | A(v=0→1) | Decay | 38 ± 7 | 1.9 ± 1.4 |
| | L=$SiHEt_3$ | E(v=0→1) | Growth | 22 ± 2 | 2 ± 7 |
| | | A(v=0→1) | Growth | 15 ± 17 | 2 ± 17 |
| $W(CO)_5L$ | L=Et-$SiHEt_2$ | E(v=0→1) | Decay | 48 ± 5 | 2.4 ± 0.4 |
| | | E(v=1→2) | Decay | <5[c] | 0.039 ± 0.001 |
| | | A(v=0→1) | Decay | 40 ± 20 | 4 ± 3 |
| | L=$SiHEt_3$ | E(v=0→1) | Growth | 22 ± 16 | 2 ± 5 |
| | | A(v=0→1) | Not Resolved | | |
| $(\eta^6-C_6H_6)-Cr(CO)_2L$ | L=CO | E(v=0→1) | Not Resolved | | |
| | | E(v=1→2) | Rise/Decay[d] | | |
| | L=alkyl + silyl $SiHEt_3$ | A(v=0→1) | Rise/Decay | 27 ± 7 | 2.6 ± 1.2 |
| | L=$SiHEt_3$ | E(v=0→1) | Growth | 22 ± 16 | 2 ± 5 |
| | | A(v=0→1) | Not Resolved | | |

[a] Complexation to the unsaturated metal center occurs through the functional group at the beginning of the ligand description

[b] Rise/Decay were fit to equation 1 with N=2, $c_1<0$, $c_2>0$; Growth were fit to equation 1 with N=2, $c_1<0$, $c_2<0$, $c_0>0$; Decay/Growth were fit to equation 1 with N=2, $c_1>0$, $c_2<0$, $c_0>0$

[c] These components could not accurately be fit

**Table 2.2** Kinetic parameters for fits to equation 2.1. Errors represent one standard deviation.

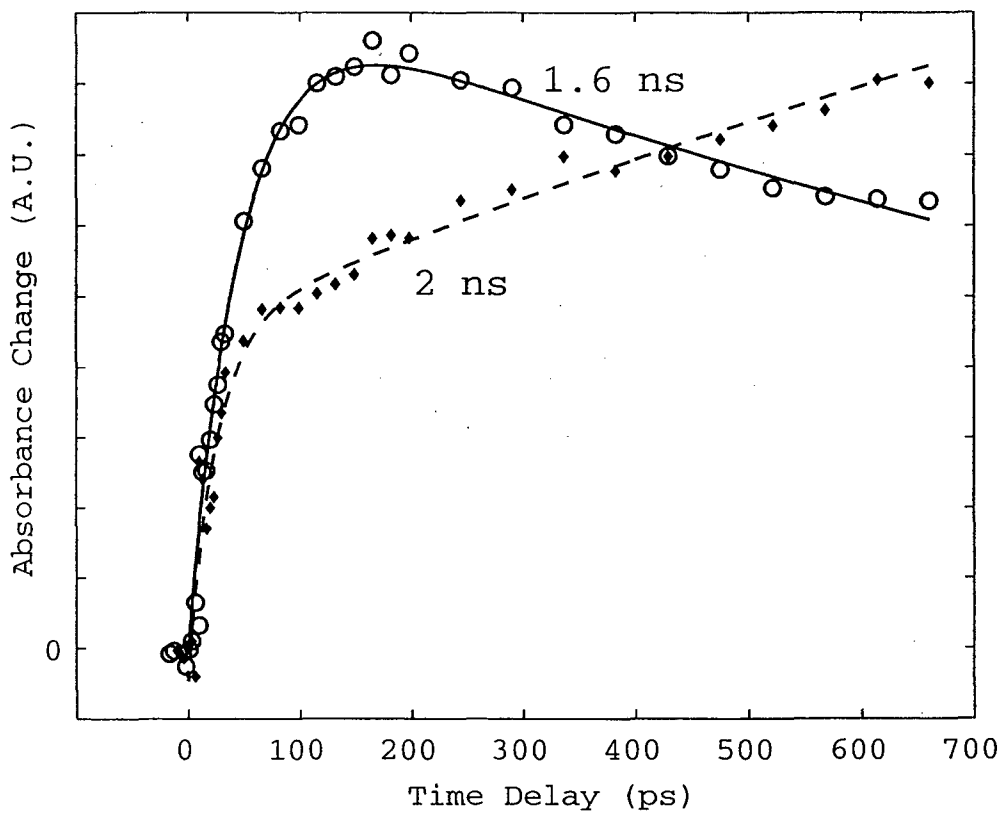


**Figure 2.4** Ultrafast kinetics of $Mo(CO)_6$ in neat triethylsilane after 295 nm UV photolysis observed at: 1963 $cm^{-1}$, the CO stretch of the alkyl solvate $Mo(CO)_5$ E band (open circles); 1956 $cm^{-1}$, the CO stretch of the silyl adduct $Mo(CO)_5$ E band (closed diamonds). The time constants for the exponential fits (smooth curves) are shown in the graph.

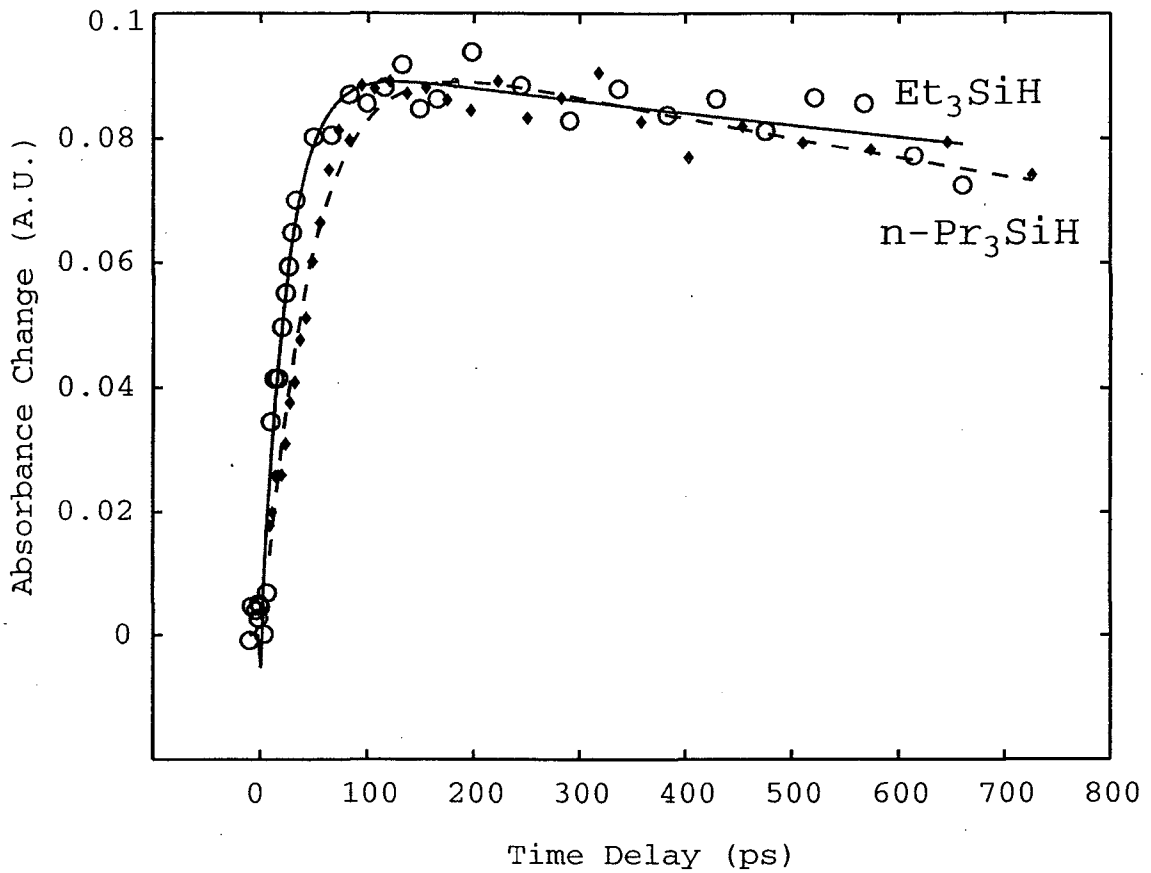


**Figure 2.5** Comparison of the ultrafast kinetics of the alkyl solvate $Cr(CO)_5$ in neat triethylsilane and in neat tri-n-propylsilane after 295 nm UV photolysis observed at: the CO stretch of the alkyl solvate $Cr(CO)_5$ E band in triethylsilane (open circles and solid line fit); the CO stretch of the alkyl solvate $Cr(CO)_5$ E band in tri-n-propylsilane $Cr(CO)_5$ (closed diamonds and dashed line fit)

The kinetics for the silyl A bands in the molybdenum and chromium systems exhibit interesting behavior. The kinetics for the silyl A band show an initial decay of approximately 15 picoseconds, followed by a growth of approximately 4 nanoseconds. Because the early time spectra are very broad, the kinetic data at early times (<20 ps) can not be resolved into peaks. This broadening has been attributed to overlap with excited lower frequency vibrational modes of the molecule and to anharmonic coupling to other intramolecular vibrational modes[39-41, 47]. It is possible that nearby bands are broadened and become overlapped with the A band. The initial decay can therefore be attributed to the narrowing of these nearby peaks. The time scale for this initial decay would then describe cooling of the low-frequency modes coupled to or overlapped with this carbonyl stretch. It is also possible that a separate band with the same frequency as the silyl A band is contributing to the initial decay. For the molybdenum pentacarbonyl, the alkyl E band has a hot band 16 $cm^{-1}$ red-shifted from the ground state vibrational transition. The silyl A band is red-shifted 22 $cm^{-1}$ from the silyl E band. It may be possible that the silyl E band $\nu=1\rightarrow2$

transition overlaps with the silyl A band. The decay of 15 picoseconds could then attributed to the vibrational cooling of the E $\nu=1\rightarrow2$ transition, and would be consistent with the cooling time for the alkyl adduct bands mentioned above. Neither explanation can be ruled out given the signal to noise of our data in this region. Regardless of the nature of the origin of this decay component, we believe that it is due to a process separate from the formation of the silyl A band. The data for the chromium silyl A band can be explained in a similar manner. The fit parameters described above also appear in table 2.2.

### 2.3.2 $(\eta^6\text{-}C_6H_6)Cr(CO)_3$ in Triethylsilane

Transient IR spectra for $(\eta^6\text{-}C_6H_6)Cr(CO)_3$ in triethylsilane were also recorded. The spectra exhibit overlapped silyl and alkyl A bands at 1870 $cm^{-1}$, one of the parent hot bands at 1887 $cm^{-1}$, and the parent bleach itself, which appears at 1913 $cm^{-1}$. The higher energy alkyl and silyl E bands, which can be found near 1923 $cm^{-1}$, were heavily overlapped with the blue edge of the parent bleach and could not be separated from one another or from the parent bleach itself. The peak assignments are based on literature values for this

compound and its adducts[48]. The product peaks at 1870 $cm^{-1}$ and 1923 $cm^{-1}$ are stable at room temperature and can be observed with static FTIR measurements. The decay observed in the ultrafast kinetics for this complex suggests that the alkyl peak directly overlaps the silyl band, and that the alkyl peak intensity is greater than that of the silyl peak intensity. These observations are consistent with the tungsten hexacarbonyl studies and the chromium hexacarbonyl study carried out in n-$Pr_3SiH$. A sample spectrum is shown in figure 2.3. The kinetic parameters for the decay of the parent bleach hot band and the parameters for the overlapping A bands can be found in table 2.2.

### 2.3.3 $Cr(CO)_6$ in Alcohols

The femtosecond dynamics following UV irradiation were recorded for $Cr(CO)_6$ dissolved in ethanol, 1-propanol, 2-propanol, and 1-hexanol. There are four discernable features in the fs-TRIR spectra for $Cr(CO)_6$ in 1-hexanol, shown in figure 2.6. The first is the parent bleach at 1985 $cm^{-1}$. The next feature is the peak at 1959 $cm^{-1}$, attributed to the complex between the pentacarbonyl fragment and the C-H bonds of the alcohol. This assignment was based on the peak position relative

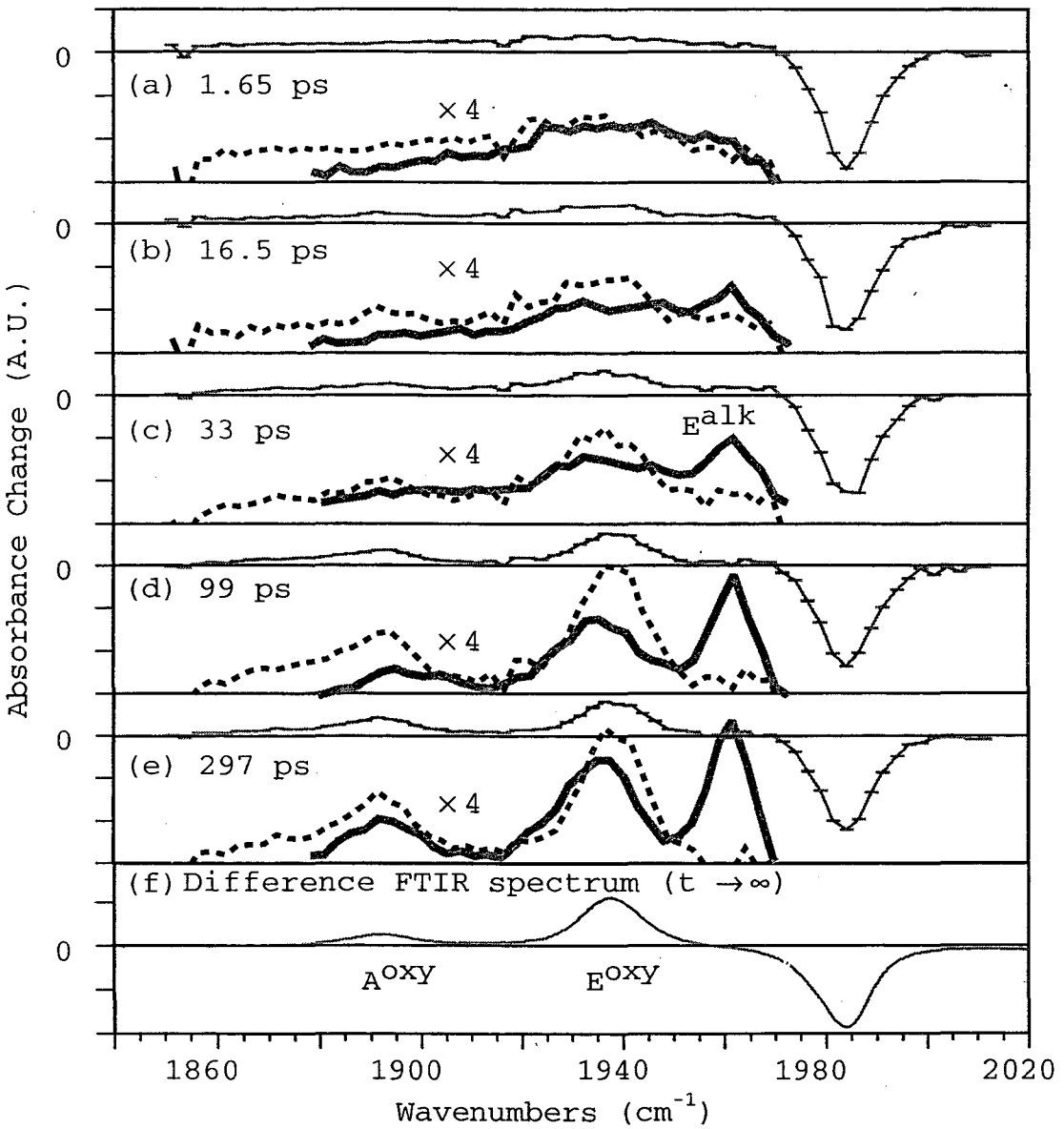


**Figure 2.6** Transient difference spectra in the CO stretching region for $Cr(CO)_6$ in neat 1-hexanol (solid grey line) at 1.65, 16.5, 33, 99, and 297 ps following 295 nm photolysis. The CO stretching bands of the alkyl solvate or hydroxyl adduct of $Cr(CO)_5$ are labeled. The insets at each of the time delays show data taken for $Cr(CO)_5$ in ethanol (dashed black line).

to the parent complex, and the peak position of the alkyl E band in alkane solution. The alkyl A band, expected to appear near 1940 $cm^{-1}$ was not observed because of the rather large intensity of the hydroxyl E band that appears in this region of the spectra. The peaks at 1896 $cm^{-1}$ and 1940 $cm^{-1}$, which can be observed in the static FTIR spectra, were due to the A and E bands respectively, of the long-lived hydroxyl-bound complex. In 1-hexanol the alkyl complex rearranged to the thermodynamically more stable hydroxyl complex on a time scale of 1.8 ns.

Figure 2.7 shows the fs-TRIR spectra for $Cr(CO)_6$ in 1-propanol solution and in 2-propanol solution. The features in these spectra are the same as those in 1-hexanol. The main difference between the propanol data and the hexanol data is the time scale for rearrangement between the alkyl and hydroxyl complexes. It is clear that this rearrangement in propanol occurs well before the final spectral trace of 660 ps. The rearrangement from alkyl to hydroxyl complexes occurs with time constants of 190 ± 10 ps in 1-propanol and 92 ± 17 ps in 2-propanol. Figure 2.6 also shows the fs-TRIR spectra of $Cr(CO)_6$ in ethanol. Unlike the propanol and hexanol data,

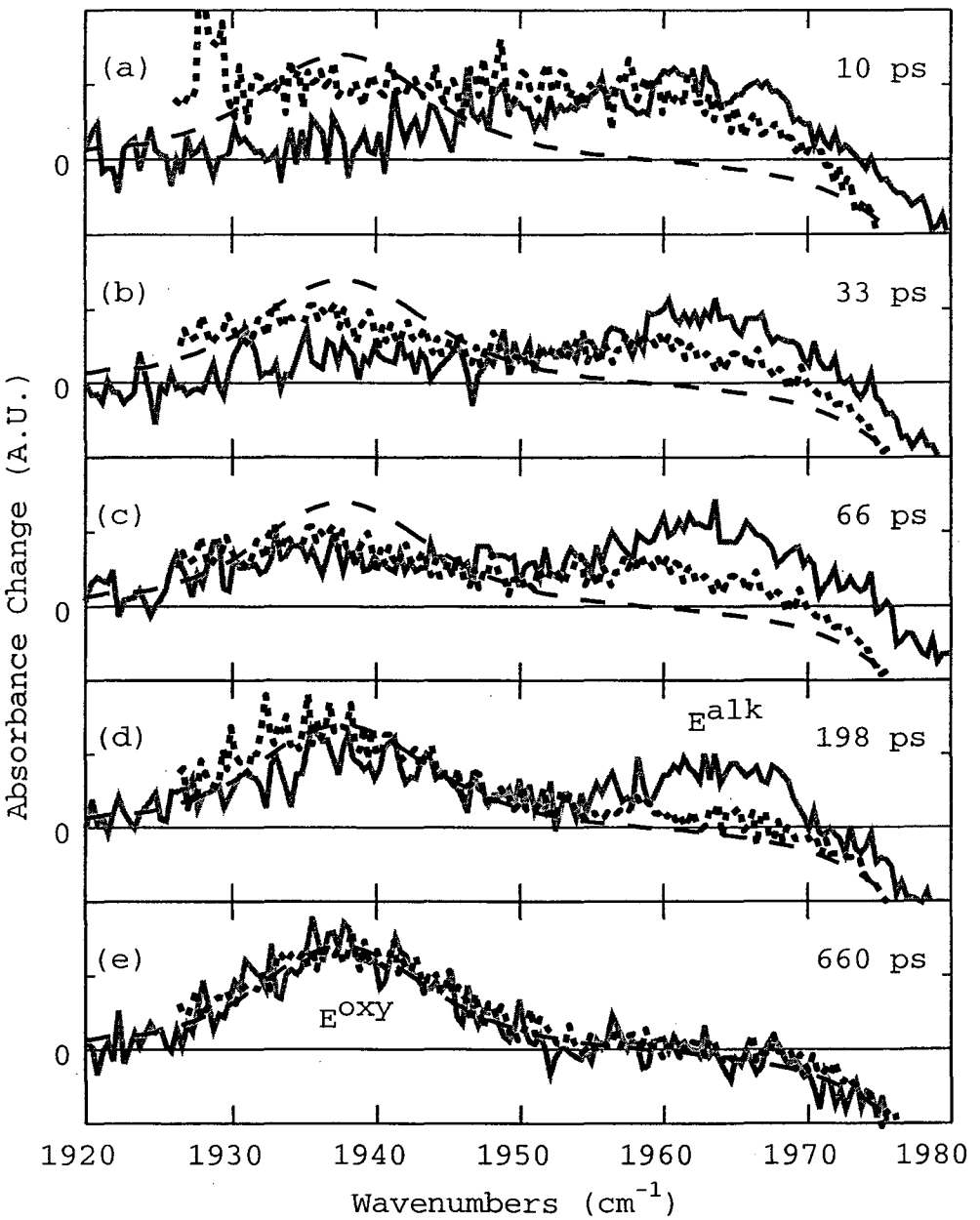


**Figure 2.7** Transient difference spectra in the CO stretching region for $Cr(CO)_6$ in neat 1-propanol (solid grey line) and 2-propanol (dotted black line) at 10, 33, 66, 198, and 660 ps following 295 nm photolysis. The CO stretching bands of the alkyl solvate or hydroxyl adduct of $Cr(CO)_5$ are labeled. Each spectrum shows the long-time FTIR product (black dashed line) as a guide.

the alkyl complex is not observed. This will be discussed later in the text. The formation of the hydroxyl complex occurs with a time constant of less than 50 ps.

## 2.4 Discussion

### 2.4.1 Metal Carbonyl Spectra

The fs-TRIR spectra from the different silane studies show remarkable similarities. In each of the systems, the E band of both the silane complex and the alkane complex can be resolved. An anharmonic shift of approximately 14 $cm^{-1}$ is observed for the alkyl E hot band. A possible shift of ~10 $cm^{-1}$ was observed for the silyl E hot band. These shifts are consistent with the 15 $cm^{-1}$ shift in the parent hexacarbonyl, and the shifts demonstrate the similarity between the vibrational potential wells of the pentacarbonyl and hexacarbonyl species[31, 46]. Similar spectral features have been observed in the IR by other researchers, but we believe that this is the first report of the simultaneous presence of the alkyl and silyl A bands for this series of metal carbonyls.

In a similar experiment, Heilweil's group noted the appearance of a previously unreported peak for the transient spectra of $Mo(CO)_6$ in n-hexane[39]. This peak appeared at 1941 $cm^{-1}$ and exhibited an exponential growth of 300 ps, which was different from the kinetics of either the A or E alkyl bands. We have carried out separate experiments in n-hexane that verify these results. Heilweil assigned the unknown peak to a singlet state complex with $D_{3h}$ symmetry. As can be seen in figure 2.1 the only peak near 1941 $cm^{-1}$ is the silyl A band at 1937 $cm^{-1}$, which exhibits much slower kinetics than those reported by Heilweil.

There are a number of possible explanations for the absence of this $D_{3h}$ peak in the silane studies. Preliminary ab initio calculations suggest that the most stable triplet $Mo(CO)_5$ structure has $D_{3h}$ symmetry. This is consistent with the results for the lowest energy triplet $Cr(CO)_5$ structure calculated by Hay[49]. Previous ultrafast experiments have concluded that the presence of electron donating ligands can quench the triplet states of 16-electron species[3, 41, 50, 51]. The presence of the Si-H binding site could therefore affect relaxation or even suppress the formation of the triplet $D_{3h}$ species

through an ultrafast spin-crossover process. If the proposed $D_{3h}$ species were a triplet rather than a singlet state, it might explain the absence of the 1941 $cm^{-1}$ peak in silanes. Further calculations on the electronic structure of $Mo(CO)_5$ are needed to differentiate these unique possibilities. Experiments carried out in other solvents may also be useful to fully understand the proposed $D_{3h}$ structure observed in alkanes.

### 2.4.2 Metal Carbonyl Kinetics

The kinetics for each of the spectral features amongst the different metal systems are also remarkably similar. As mentioned above, the kinetics suggest rearrangement from the alkyl complex to the silyl complex. The trend in rearrangement time scales follows the order Mo < Cr < W. This trend is consistent with the observed dissociation enthalpies of various alkanes from $M(CO)_5$ (M = Cr, Mo, W)[16]. As discussed above, the ultrafast spectra for the different alkyl complexes are spectroscopically similar to those in alkane solution. This suggests that the alkyl chains of silanes behave much like free alkane molecules. This has also been observed in previous silane studies[35]. The overall similarity in bond energetics, and similar kinetic rates

for the rearrangement process strongly suggests a similar mechanism for rearrangement from the alkyl to the silyl solvate for the different metal systems.

### 2.4.3 Chain-Walk Mechanism

The ultrafast rearrangement of alcohols with $Cr(CO)_5$ metal centers was previously studied by Simon and co-workers using picosecond UV-Vis spectroscopy[14, 15, 18, 19, 52]. They modeled the rearrangement as an intramolecular process by which a bound solvent molecule would change its coordination to the unsaturated metal center by walking along the backbone of the carbon chain[19]. They proposed the chain-walk mechanism to describe the rearrangement at alcohols based on the observation that the rearrangement time for 1-propanol was approximately 200 ps, whereas the rearrangement time in 2-propanol was identical to the rearrangement time in ethanol, ~80 ps. They found that a single pair of rate constants was able to fit the kinetic data for a series of linear alcohols with 2-8 carbons in the alkyl chain: (1) $k_{cc}=4*10^9\ s^{-1}$, the rate at which the molecule walked between methylene units of the alcohol backbone; and (2) $k_{co}=2*10^{10}\ s^{-1}$ the rate for walking onto the strong-binding hydroxyl site. Ultrafast studies in the UV-Vis, however,

can be obscured by the very complex potential energy surface of large molecules, and the visible probe used in such studies probes the Frank-Condon overlap between the ground state and complicated excited state electronic potential energy surfaces.

Our fs-TRIR results probe the actual populations of both the hydroxyl and silyl adducts. Because metal-carbonyl stretching frequencies are strongly affected by the electronic density at the metal center, both of these adducts can be unambiguously identified with IR spectroscopy. From our observations, it seems clear that there are distinct differences between the rearrangement times of ethanol, 1-propanol, and 2-propanol. The trends in rearrangement times between these solvents observed by Simon probably arose from changes in the Franck-Condon overlap due to vibrational cooling in the ground-state wells of the alkyl and hydroxyl complexes. Our IR data seems to call into question the fundamental experimental basis for the chain-walk mechanism.

The chain-walk mechanism also fails to accurately describe the silane data. The adaptation of the chain-walk mechanism to the silane rearrangement studies is depicted in figure 2.8. If we try to use the chain-walk

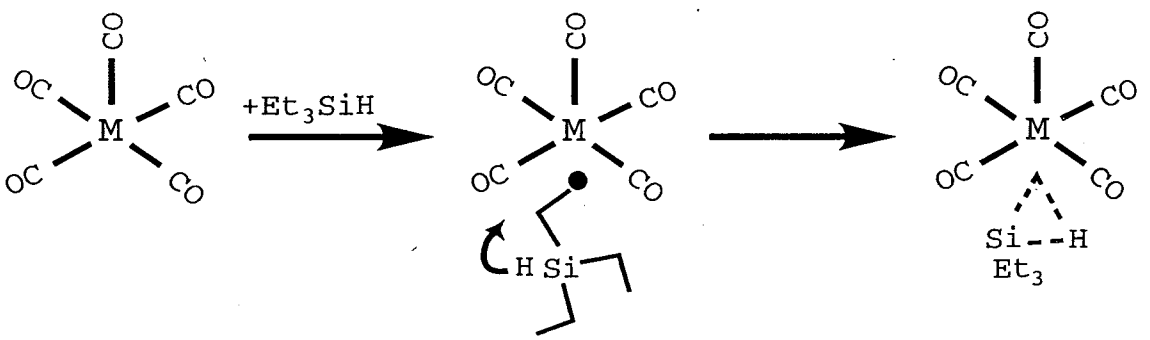


**Figure 2.8** Scheme of the chain-walk mechanism adapted to silanes

mechanism to describe the silane data, qualitatively, we see that the rearrangement time in triethylsilane should be similar to the rearrangement time for ethanol. Both involve a single walk from the weakly-bound sites to the stronger of the binding sites of the solvent. The main differences between the two solvents would appear as different initial coordination statistics, and differences in the rates for walking onto the strongly bound sites. Our data show that the rearrangement in triethylsilane is at least 20 times slower than in ethanol. One could argue that the rate to walk onto a hydroxyl site could be less than the rate to form a Si-H complex due to increased steric hindrance at the Si-H site as compared to the hydroxyl site. It could also be the case that the hydroxyl "hop" is facilitated by some sort of transition state stabilization by the hydroxyl moiety. In order to test the generality of the chain-walk, we conducted an experiment in a silane with longer alkyl chains substituted at the silicon atom. Based on the chain-walk mechanism, we would expect the alkyl complex in such a silane to rearrange at a noticeably slower rate when compared to triethylsilane. Our observations in figure 2.5, however, seem to indicate

that the alkyl solvate rearrangement times are approximately the same for either n-$Pr_3SiH$ or triethylsilane silane solvent. The chain-walk mechanism, therefore, seems to be unable to describe the rearrangement of silanes in chromium carbonyl complexes. These observations for rearrangement in silanes and alcohols lead us to conclude that the strictly intramolecular chain-walk mechanism proposed by Simon fails to describe the rearrangement of ligands at group 6, unsaturated transition metal complexes.

### 2.4.4 Rearrangement Dynamics

The mechanism describing ligand rearrangement at unsaturated metal centers has been thoroughly studied by Dobson's group. They proposed that the mechanism for rearrangement resembled the process shown in figure 2.9a, where M is chromium, $L_w$ is a weakly-binding token ligand, and $L_s$ is a strongly-binding, electron-donating ligand[28, 30]. This mechanism was found to fit their data for a large variety of ligands, $L_w$ and $L_s$. As was previously mentioned, these experiments lacked the time resolution to rule out the possibility of chain-walk, especially for weakly-bound ligands such as short chain alkanes. In light of the above discussion, it seems unlikely that

A. Dobson Mechanism:

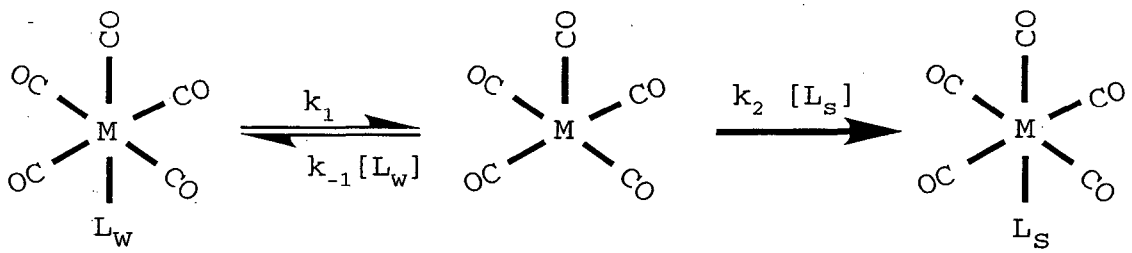


B. Silane Rearrangement:

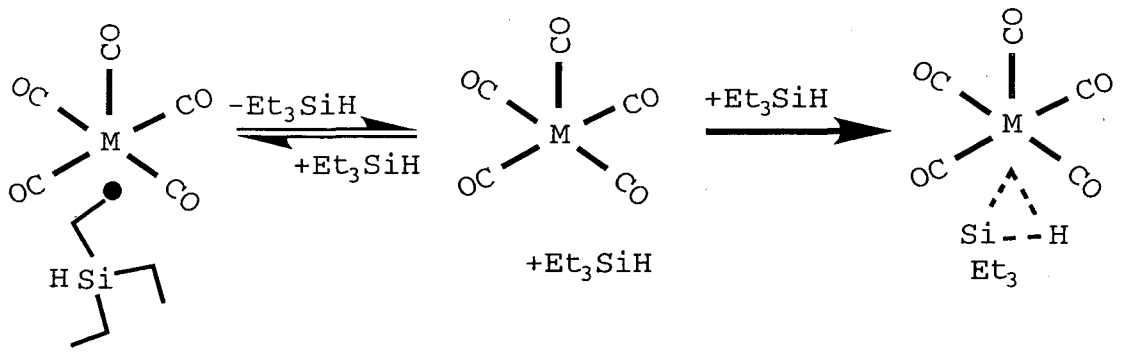


**Figure 2.9** Scheme summarizing dissociative rearrangement at a coordinatively unsaturated transition metal center in the case of: A) general rearrangement with weak and strong-binding ligands; and B) specific rearrangement with triethylsilane as the ligand.

chain-walk occurs in solution for the group 6 metal complexes. The mechanism proposed by Dobson and co-workers seems to accurately describe the ligand dynamics for chemical systems in this study. This mechanism adapted to the silane studies is shown in figure 2.9b, where $L_w$ has been changed to the ethyl ligand on the silane and $L_s$ has been become the silicon-hydrogen bond of the silane. Because the bare metal fragments are known to solvate extremely rapidly (~1-2 ps), the rates $k_{-1}$ and $k_2$ in Dobson's mechanism are expected to be extremely fast[52]. The overall mechanism should therefore be limited by the dissociation rate of the $L_w$ ligand, $k_1$. It is interesting to note that the rearrangement from an alkyl to a silyl complex for the group 7 complexes $(\eta^5\text{-}C_5H_5)M(CO)_2$ (M = Mn and Re) was also described as dissociative in nature[3, 53, 54]. In these latter systems, rearrangement times were orders of magnitude longer than those for the group 6 systems were. These differences can be attributed to the differences in binding enthalpies for the alkyl complexes between the group 6 and group 7 complexes[20, 55-57]. Data from section 2.3.2 also suggest that the rearrangement of the alkyl solvate at the 16-electron chromium metal center of

$(\eta^6\text{-}C_6H_6)Cr(CO)_3$ occurs with a barrier similar to that for the hexacarbonyl complexes, ~5.6-6.0 kcal/mol. We were able to deduce an approximate time scale of 4 ns for the rearrangement process of this half-sandwich complex. These observations, along with the data presented earlier, suggest the dissociative mechanism in figure 2.8 is somewhat general for the rearrangement of ligands at a variety of transition metal centers.

The interaction between the metal pentacarbonyls $M(CO)_5$ (M = Cr, Mo, and W) and the alkyl carbon-hydrogen bond is known to be weak (~7-9 kcal/mol)[20, 58-60]. With such small complexation energies comparable to that of solvent-solute interactions, it is expected that the potential of mean force should be largely affected. This results in the observed free energy barriers (5.5-6 kcal/mol) for the rearrangement process that are lower than the complexation energies (~7-9 kcal/mol). This barrier lowering can be attributed to the influence of the solvent molecules on the reaction pathway. One possible scenario describing this effect is the involvement of an additional solvent molecule in an associative manner in which the extra solvent molecule is contained in the transition state. The dynamic origin of

this barrier lowering is not clear at the microscopic level, but it is expected that the microscopic details of the solvation process contribute to the energetics of the rearrangement processes.

The next chapter discusses an alternative model that may provide greater insight into the mechanism of such ligand rearrangements.

This majority of the work in this chapter has been previously published as (reference [4]): Kotz, K.T.; Yang, H.; Snee, P.T.; Payne, C.K.; Harris, C.B. "Femtosecond Infrared Studies of Ligand Rearrangement Reactions: Silyl Hydride Products from Group 6 Carbonyls" *Journal of Organometallic Chemistry*, **2000**, *596*, 183-192.

# Chapter 3

# A Brownian Dynamics Simulation of the Rearrangement of Ligands at Coordinatively Unsaturated Group 6 Transition Metal Complexes

## 3.1 Introduction

In chapter 2, it was shown that previous models that described the dynamics for the rearrangement of weakly-bound ligands at coordinatively unsaturated transition metal complexes were inadequate[4]. In particular, it was shown that the intramolecular model proposed by Simon et al. failed to describe this rearrangement process for alcohols and silanes at group 6 metal complexes[19]. Other mechanisms have been suggested, namely a dissociative mechanism, but there has not been any attempts to model such a mechanism on a microscopic level and test its validity.

The experimental results of the last chapter were based on femtosecond infrared spectroscopy, which offers much better spectral resolution over UV-Vis

techniques[4]. The results for the rearrangement time scales for ethanol (<50 ps), 2-propanol (~100 ps), and 1-propanol (~190 ps) disagree with previous UV-Vis measurements[14, 15, 18, 19]. The proposed intramolecular chain-walk mechanism depicted in figure 3.1 predicts that a substantial amount of alkyl-bound metal-alcohol complexes, denoted $(CO)_5Cr(ROH)$, should exist appear immediately following photodissociation. This alkyl-complex, however was *not* observed in the femtosecond-infrared experiments in ethanol. In addition, the fitting parameters given by Simon et al. predict that the time scales for rearrangement in the 1-propanol system should be much greater (~200 ps) than that for the rearrangement in 2-propanol and ethanol (both ~50 ps)[19]. Again, our infrared data show that this is not the case[4].

In order to address the various issues mentioned above, an intermolecular site-diffusion model has been constructed. The model is based on the reaction scheme shown in figure 3.2. Following the photodissociation of a CO ligand from the parent $Cr(CO)_6$ molecule, the coordinatively unsaturated $Cr(CO)_5$ fragment can be solvated through a hydroxyl site of a surrounding alcohol

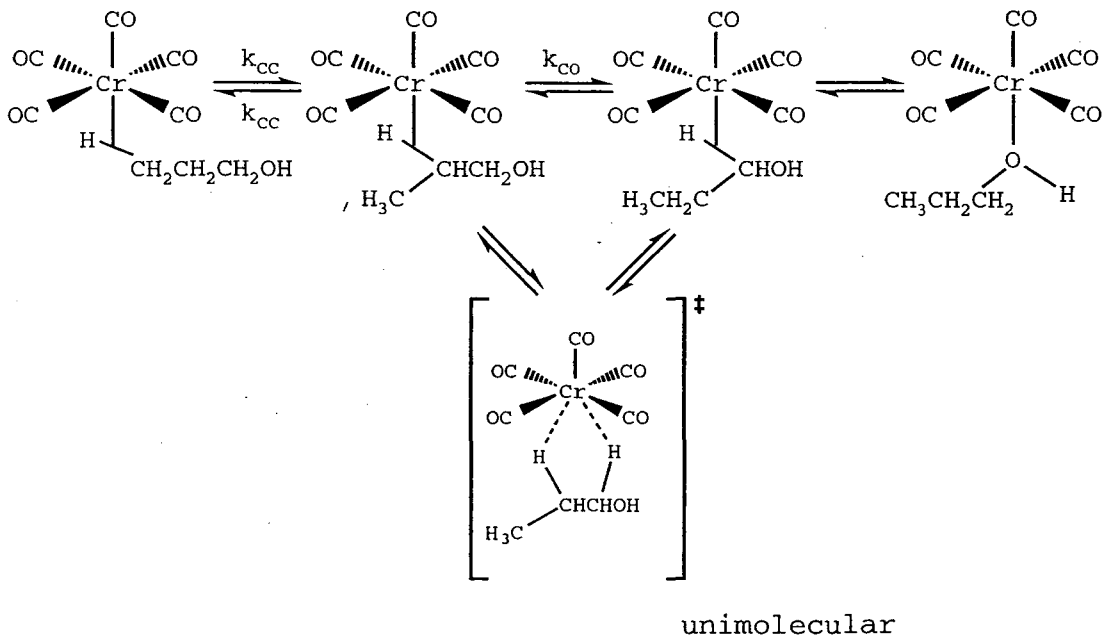


**Figure 3.1** An intramolecular rearrangement reaction mechanism for 1-propanol at $Cr(CO)_5$. The proposed transition state structure in the square brackets is one of many possible structures. The rate constants $k_{CC}$ and $k_{CO}$ are the constants used by Simon et al. in his mechanism[]. Note that this model assumes that the alcohol becomes strongly bound when it reaches α-carbon site. Furthermore, this model is strictly unimolecular in nature.

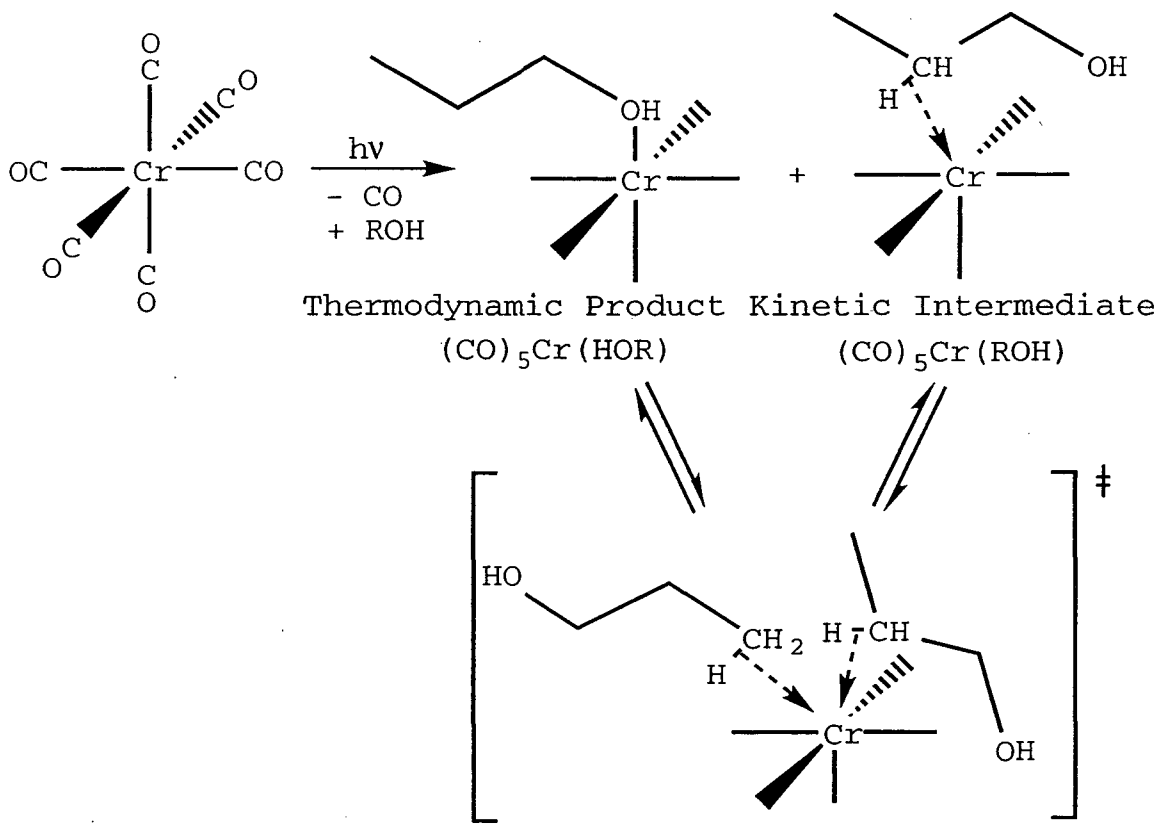


**Figure 3.2** A dissociative rearrangement reaction mechanism for 1-propanol at $Cr(CO)_5$. The proposed transition state structure in the square brackets is one of many possible structures.

molecule (1-propanol is shown as an example in figure 3.2), to form a thermodynamically stable complex denoted, $(CO)_5Cr(OHR)$, or it can be solvated through one of the carbon sites of the alkane chain of the alcohol to form the kinetic intermediate, $(CO)_5Cr(ROH)$. This latter kinetic product can then rearrange to form the thermodynamic product through an intermolecular pathway. The molecular details of the transition state in the rearrangement are not known, but one possibility is depicted in figure 3.2. One could picture this rearrangement as a diffusion process in which a $Cr(CO)_5$ complex randomly walks through a fluid containing binding-sites, which correspond to the alkyl and hydroxyl binding sites in alcohols, until a strongly-binding hydroxyl site is met. A scheme for such a process is shown in figure 3.3. As shown in figure 3.3, the different sites do not necessarily correspond to sites on the same alcohol, i.e. the diffusion is modeled as an intermolecular process.

The theoretical framework for the site-diffusion model is laid out in the next section of this chapter. It can be seen that site-specific binding energies will be needed in order to describe this site-diffusion

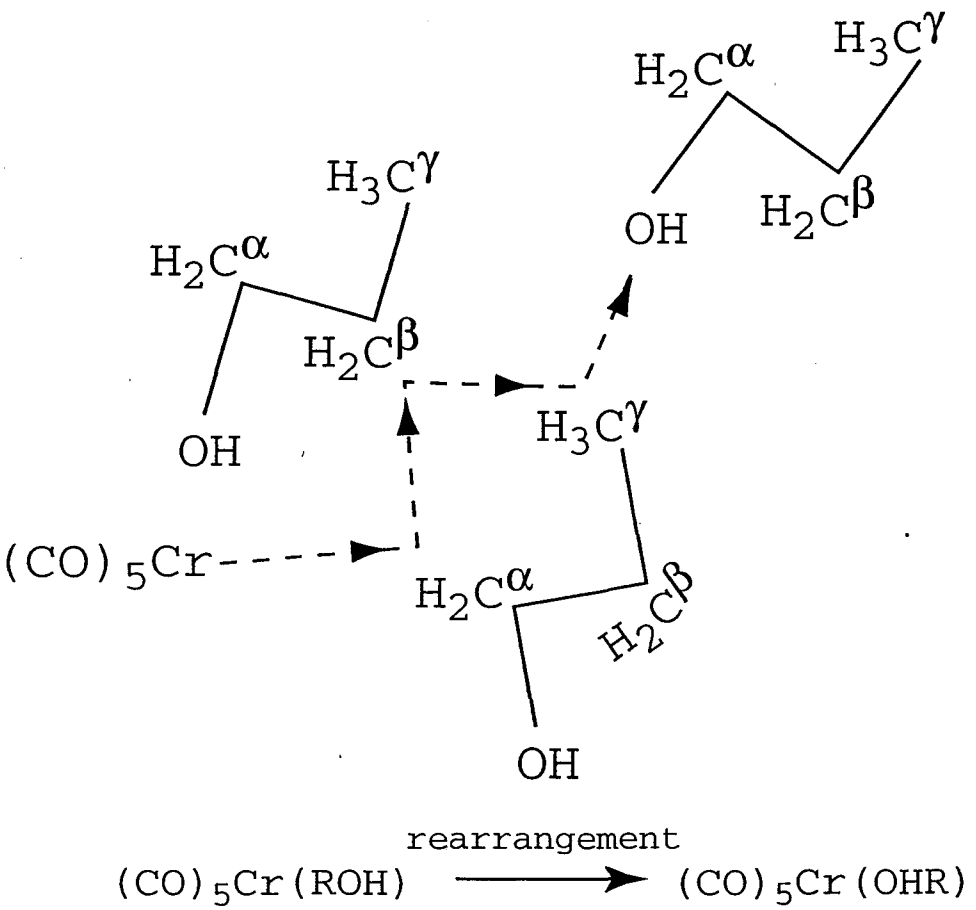


**Figure 3.3** A schematic represantation of the site-diffusion model. Here a $Cr(CO)_5$ complex hops from one carbon site to another in 1-propanol until it reaches a terminating hydroxyl binding site.

process. As mentioned in the previous chapter, alkyl-metal fragment binding energies in solution are on the order of 5-7 kcal/mol, and thus highly reactive and unstable. Therefore, we have chosen to use binding energies as calculated with ab initio methods. The details of such calculations are presented in section 3. Section 4 describes the computational engine and the detailed potentials used to model the diffusing particles. The remaining sections present the simulation results and discuss them in light of the experimental data laid out in chapter 1.

### 3.2 Basic Theory

In 1940, Hendrik Kramers published a paper outlining a theory for chemical reactions in solution[61]. An excellent review of Kramers' theory has been published by Hänngi et al. that describes the historical background, development, and current status of this theory[62]. Only a brief overview of the theory will be presented here.

Kramers' theory treats a chemical reaction as diffusion along a one-dimensional potential $V(x)$, where $x$ is the reaction coordinate. A sample double-well potential is shown in figure 3.4. In this potential model, products and reactants occur along the potential

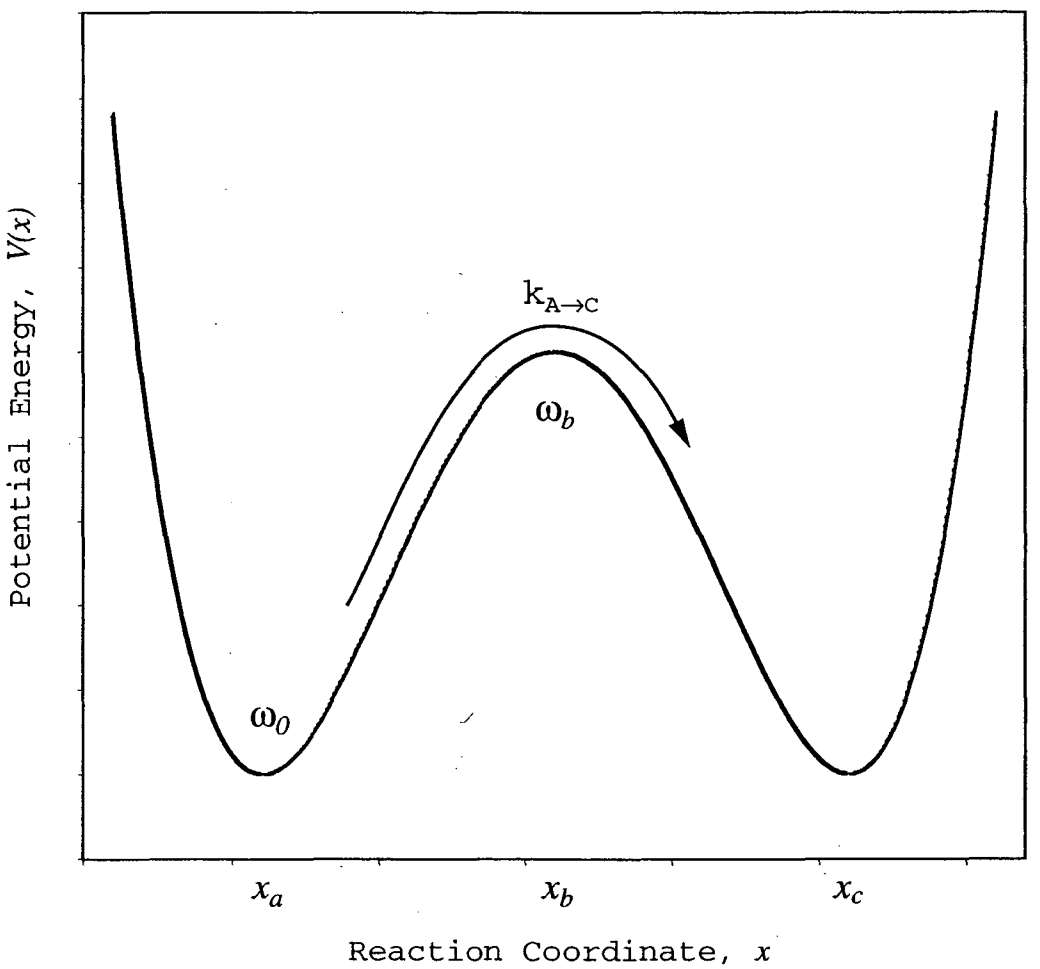


**Figure 3.4** Symmetric double-well potential used to test the simulation engine.

at $x_a$ and $x_c$ respectively, and must cross a barrier maximum of $U(x_b)$ at $x_b$. This local-maximum along the potential surface corresponds to the transition state of the chemical reaction. The dynamics of the simulation particles along this one-dimensional potential are assumed to conform to a Langevin equation:

$$m\frac{d^2}{dt^2}x = \frac{d}{dt}v = -\frac{d}{dx}V(x) - \gamma m\frac{d}{dt}x + F(t), \qquad 3.1$$

where $m$ is the mass of the diffusing particle. In solution phase, there are numerous degrees of freedom that can affect the rate of a chemical reaction. In Kramers' theory, these degrees of freedom are reduced to a damping rate, $\gamma$, and a random fluctuating force, $F(t)$, in equation 3.1. $F(t)$ describes random fluctuations exerted on the particle by the surrounding solvent molecules. This white noise source, $F(t)$, is assumed to have a zero mean and to obey the fluctuation-dissipation theorem:

$$\langle F(t)\rangle = 0, \qquad 3.2$$

$$\langle F(t)F(0)\rangle = 2m\gamma k_B T\delta(t). \qquad 3.3$$

Equation 3.1 along with the equation: $dx/dt = v$, define the equations of motion for the diffusing particle. The solution to these equations of motion can be obtained for

the simple potential shown in figure 3.4[62, 63]. In the high-friction limit ($\gamma > \omega_b$) the celebrated Kramers' result for the rate of reaction from reactants to products is:

$$k_{A\to C} = \frac{\lambda_+}{\omega_b}\left[\frac{\omega_0}{2\pi}e^{-\beta E_b}\right] \qquad 3.4$$

$$= \frac{\sqrt{(\gamma/2)^2+\omega_b^2}-\gamma/2}{\omega_b}\left[\frac{\omega_0}{2\pi}e^{-\beta E_b}\right] \qquad 3.5$$

where $\omega_0$ and $\omega_b$ are the are curvature at the bottom and the top of the potential, $V(x)$. This expression is derived assuming that the potential is piecewise parabolic at the top and bottom of the well. It further assumes that the reaction barrier is larger than $k_BT$. The constant friction, $\gamma$, is a result of Markovian dynamics for this system. The validity of these assumptions, and the application of the above equations to the current simulation will be discussed in the following sections.

### 3.3 Site-specific Binding Energetics

As mentioned in the introduction, ab initio and DFT have been extremely useful in clarifying the chemical structures of weakly-bound ligands at unsaturated transition metal complexes[2-4, 35, 36, 50, 55, 64]. Thus, to better understand the binding of alcohols to coordinatively unsaturated group 6 metal carbonyls, a series of computational studies were carried out.

### 3.3.1 Computational Details

For DFT calculations, the commercial software package, JAGUAR, was used[65]. The B3LYP exchange-correlation functional, which is known to give excellent results for transition metal complexes, was employed in all of the calculations[66-70]. Except for the bare pentacarbonyl metal fragments, which have obvious $C_{4v}$ symmetry, no symmetry constraints were placed on the molecules during geometry optimization. A frequency calculation was carried out after each geometry optimization to ensure that a minimum energy structure had been located. The frequency analyses were used to obtain thermodynamic properties, such as the zero point energy (ZPE) and the enthalpy, H, which were used in the following results. Ab initio calculations at the frozen-core second-order Møller-Plesset perturbation level of theory (MP2) were then carried out on these B3LYP structures using the GAMESS-US package[71]. Two basis sets were used in both DFT and ab initio calculations. Basis set I consisted of the 6-31G basis functions for H, C, and O, and the Los Alamos Effective Core Potential (ECP) for the transition metals Cr, Mo, and W with the outer-most core orbitals included in the valence

description[72-74]. Basis set II was the same as basis set I with polarization functions added on all atoms except the metals. The smaller basis set I was used for geometry optimizations and frequency calculations. For all calculations, the basis set superposition error (BSSE) was calculated using the scheme proposed by Xantheas, as well as the standard counter-poise correction scheme[75].

### 3.3.2 Characterization of the Computational Methods

The results for the DFT-B3LYP and the MP2 ab initio calculations are shown in tables 3.1 and 3.2, respectively. Both tables give the give the calculated interaction energy of the $(CO)_5M\ldots$(solvent) (M = Cr, Mo or W; solvent = $CH_4$, $C_2H_6$, $C_3H8$ or $CH_3F$) systems using different correction schemes. In the tables, ΔZPE and ΔH are the correction terms for zero point energy and enthalpy at 298.15 K. Table 3.3 compares the results from table 3.2 with other computational results and with gas-phase experimental values for complexation energies of alkanes with $W(CO)_5$ [60, 76]. The general trend of increasing complexation energy with increasing alkyl length is reproduced with our MP2 calculations. Furthermore, the MP2 results in table 3.2 suggest that

| $Cr(CO)_5$(Solvent) | ΔE | ΔE+ΔZPE | ΔE+ΔZPE+ΔH | CP+ΔZPE | CP+ΔZPE+ΔH | BSSE+ΔZPE | BSSE+ΔZPE+ΔH |
|---|---|---|---|---|---|---|---|
| ***Basis Set I*** | | | | | | | |
| Methane | -4.4 | -3.3 | -3.2 | -2.3 | -2.2 | -1.8 | -1.6 |
| Ethane | -5.3 | -4.5 | -4.2 | -3.3 | -3.0 | -2.6 | -2.3 |
| Propane | -5.6 | -4.8 | -4.4 | -3.2 | -2.8 | -2.6 | -2.2 |
| ***Basis Set II*** | | | | | | | |
| Methane | -4.0 | -3.0 | -2.9 | -2.5 | -2.4 | -1.9 | -1.7 |
| Ethane | -4.5 | -3.7 | -3.4 | -3.5 | -3.2 | -2.7 | -2.4 |
| Propane | -4.2 | -3.5 | -3.1 | -3.4 | -3.0 | -2.6 | -2.2 |
| $Mo(CO)_5$(Solvent) | | | | | | | |
| ***Basis Set I*** | | | | | | | |
| Methane | -2.8 | -3.9 | -3.6 | -3.1 | -2.8 | -2.5 | -2.3 |
| Ethane | -3.5 | -4.9 | -4.4 | -3.9 | -3.5 | -3.3 | -2.8 |
| Propane | -3.4 | -5.3 | -4.8 | -4.0 | -3.4 | -3.4 | -2.8 |
| ***Basis Set II*** | | | | | | | |
| Methane | -3.0 | -3.4 | -3.2 | -3.3 | -3.0 | -2.6 | -2.4 |
| Ethane | -3.6 | -3.8 | -3.4 | -4.1 | -3.6 | -3.4 | -2.9 |
| Propane | -3.6 | -3.8 | -3.3 | -4.1 | -3.6 | -3.4 | -2.8 |
| $W(CO)_5$(Solvent) | | | | | | | |
| ***Basis Set I*** | | | | | | | |
| Methane | -6.0 | -5.1 | -4.9 | -4.6 | -4.4 | -3.6 | -3.5 |
| Ethane | -7.0 | -6.4 | -6.0 | -5.8 | -5.4 | -4.7 | -4.4 |
| Propane | -7.2 | -6.7 | -6.3 | -5.8 | -5.3 | -4.7 | -4.3 |
| Fluoromethane ($CH_3F$) | -21.5 | -20.4 | -20.1 | -14.3 | -14.1 | -13.3 | -13.0 |
| ***Basis Set II*** | | | | | | | |
| Methane | -5.5 | -4.7 | -4.5 | -4.9 | -4.7 | -3.9 | -3.7 |
| Ethane | -6.0 | -5.4 | -5.0 | -6.0 | -5.7 | -4.9 | -4.5 |
| Propane | -5.7 | -5.2 | -4.8 | -6.0 | -5.6 | -4.8 | -4.4 |
| Fluoromethane ($CH_3F$) | -16.8 | -15.7 | -15.5 | -12.4 | -12.2 | -9.5 | -9.3 |

**Table 3.1** B3LYP energies (kcal/mol) for the reaction: $M(CO)_5$ + (Solvent) → $M(CO)_5$(Solvent) at various correction levels.

| $Cr(CO)_5$(Solvent) | ΔE | ΔE+ΔZPE | ΔE+ΔZPE+ΔH | CP+ΔZPE | CP+ΔZPE+ΔH | BSSE+ΔZPE | BSSE+ΔZPE+ΔH |
|---|---|---|---|---|---|---|---|
| ***Basis Set I*** | | | | | | | |
| Methane | -10.4 | -9.3 | -9.2 | -5.0 | -4.9 | -5.1 | -4.9 |
| Ethane | -12.7 | -11.9 | -11.6 | -7.0 | -6.7 | -6.8 | -6.5 |
| Propane | -13.5 | -12.8 | -12.4 | -7.3 | -6.9 | -7.2 | -6.8 |
| ***Basis Set II*** | | | | | | | |
| Methane | -11.2 | -10.2 | -10.1 | -6.4 | -6.3 | -6.4 | -6.2 |
| Ethane | -13.5 | -12.7 | -12.4 | -8.5 | -8.2 | -8.3 | -7.9 |
| Propane | -14.4 | -13.6 | -13.2 | -8.9 | -8.5 | -8.7 | -8.2 |
| $Mo(CO)_5$(Solvent) | | | | | | | |
| ***Basis Set I*** | | | | | | | |
| Methane | -10.1 | -9.3 | -9.1 | -5.0 | -4.7 | -4.7 | -4.4 |
| Ethane | -11.7 | -11.1 | -10.7 | -6.5 | -6.0 | -6.1 | -5.7 |
| Propane | -12.5 | -12.1 | -11.5 | -7.0 | -6.4 | -6.6 | -6.1 |
| ***Basis Set II*** | | | | | | | |
| Methane | -10.3 | -9.6 | -9.3 | -6.1 | -5.8 | -5.5 | -5.3 |
| Ethane | -11.8 | -11.3 | -10.8 | -7.6 | -7.1 | -7.0 | -6.5 |
| Propane | -12.7 | -12.3 | -11.7 | -8.2 | -7.7 | -7.6 | -7.0 |
| $W(CO)_5$(Solvent) | | | | | | | |
| ***Basis Set I*** | | | | | | | |
| Methane | -12.1 | -11.2 | -11.1 | -6.4 | -6.3 | -5.9 | -5.7 |
| Ethane | -14.2 | -13.6 | -13.2 | -8.4 | -8.1 | -7.8 | -7.5 |
| Propane | -15.4 | -14.9 | -14.4 | -9.0 | -8.6 | -8.5 | -8.0 |
| Fluoromethane ($CH_3F$) | -24.3 | -23.2 | -22.9 | -13.7 | -13.5 | -14.1 | -13.8 |
| ***Basis Set II*** | | | | | | | |
| Methane | -12.5 | -11.6 | -11.5 | -7.8 | -7.7 | -7.0 | -6.9 |
| Ethane | -14.6 | -14.0 | -13.7 | -10.0 | -9.7 | -9.1 | -8.7 |
| Propane | -15.7 | -15.2 | -14.7 | -10.6 | -10.2 | -9.7 | -9.3 |
| Fluoromethane ($CH_3F$) | -23.2 | -22.1 | -21.9 | -14.8 | -14.5 | -12.6 | -12.4 |

**Table 3.2** MP2 energies (kcal/mol) for the reaction:
$M(CO)_5$ + (Solvent) → $M(CO)_5$(Solvent) at various correction levels.

| | Values from Table 3.1 | Zaric-Hall ref.[58] | Experiment ref.[59,60] |
|---|---|---|---|
| Methane | 6.9 | 4.2 | <5 |
| Ethane | 8.7 | 7.0 | 7.4 ± 2 |
| Propane | 9.3 | 9.1 | 8.1 ± 2 |
| Fluoromethane($CH_3F$) | 12.4 | 10.6 | 11.2 ± 3 |

**Table 3.3** Comparison of calculated binding energies (kcal/mol) of $W(CO)_5$(solvent) with previous work.

the ($\Delta$BSSE + $\Delta$ZPE + $\Delta$H) with Basis Set II provides a superior procedure to that carried out with Basis Set I. In fact, the calculated binding energies with the Basis Set II/MP2 method lie within experimental errors with a systematic deviation of ~1 kcal/mol from the experimental averages[60].

The B3LYP approach does not appear to provide accurate numerical results for these systems. It fails to produce the trends in the experimental data, it tends to underestimate the weak metal-alkane interaction, and the BSSE is typically less pronounced in the B3LYP calculations when compared to the MP2 approach.

### 3.3.3 The $(CO)_5Cr$-(alcohol) Interaction Energy

For the construction of the potential energy curves used in the Brownian dynamics simulations, we carried out a series of MP2 calculations with Basis Set II for the complexation energy between $Cr(CO)_5$ and the alcohols: $CH_3OH$, $C_2H_5OH$, and $C_3H_7OH$. Binding energy calculations were carried out for each of the unique C-H bonds of the alcohols, and are shown in table 3.4. The observed trend in interaction energy decreases in the order of $C\text{-}H_\alpha$ > $C\text{-}H_\beta$ > $C\text{-}H_\gamma$. This can be understood by thinking of the relative electron availability at each site, $\alpha$, $\beta$ or $\gamma$.

| $Cr(CO)_5$...(Alcohol) | ΔE | ΔE+ΔZPE | ΔE+ΔZPE+ΔH | CP+ΔZPE | CP+ΔZPE+ΔH | BSSE+ΔZPE | BSSE+ΔZPE+ΔH |
|---|---|---|---|---|---|---|---|
| ***Basis Set I*** | | | | | | | |
| $Cr(CO)_5$...(α-Methanol) | -11.6 | -11.6 | -12.1 | -6.2 | -6.7 | -5.6 | -6.1 |
| $Cr(CO)_5$...($OHCH_3$) | -32.9 | -32.0 | -32.7 | -20.8 | -21.5 | -21.5 | -22.1 |
| $Cr(CO)_5$...(β-Ethanol) | -13.3 | -12.7 | -12.3 | -7.0 | -6.6 | -7.7 | -7.3 |
| $Cr(CO)_5$...(α-1-Propanol) | -14.7 | -14.1 | -13.6 | -8.0 | -7.5 | -8.0 | -7.6 |
| $Cr(CO)_5$...(β-1-Propanol) | -13.9 | -13.3 | -12.8 | -7.4 | -6.9 | -6.8 | -6.4 |
| $Cr(CO)_5$...(γ-1-Propanol) | -13.1 | -12.4 | -12.0 | -6.8 | -6.4 | -6.6 | -6.2 |
| $Cr(CO)_5$...(α-2-Propanol) | -14.7 | -14.4 | -13.9 | -8.4 | -7.9 | -7.3 | -6.7 |
| $Cr(CO)_5$...(β-2-Propanol) | -14.2 | -13.6 | -13.2 | -7.3 | -6.9 | -6.8 | -6.4 |
| ***Basis Set II*** | | | | | | | |
| $Cr(CO)_5$...(α-Methanol) | -13.2 | -13.2 | -13.7 | -7.9 | -8.4 | -7.6 | -8.1 |
| $Cr(CO)_5$...($OHCH_3$) | -31.0 | -30.1 | -30.8 | -21.2 | -21.9 | -20.6 | -21.3 |
| $Cr(CO)_5$...(α-Ethanol) | -14.6 | -14.0 | -13.5 | -8.7 | -8.3 | -8.2 | -7.8 |
| $Cr(CO)_5$...(β-Ethanol) | -14.1 | -13.5 | -13.0 | -8.3 | -7.9 | -7.7 | -7.3 |
| $Cr(CO)_5$...(α-1-Propanol) | -15.7 | -15.1 | -14.6 | -9.5 | -9.1 | -9.9 | -9.4 |
| $Cr(CO)_5$...(β-1-Propanol) | -15.5 | -14.9 | -14.4 | -9.0 | -8.6 | -9.1 | -8.7 |
| $Cr(CO)_5$...(γ-1-Propanol) | -14.2 | -13.5 | -13.1 | -8.5 | -8.1 | -8.4 | -7.9 |
| $Cr(CO)_5$...(α-2-Propanol) | -15.9 | -15.7 | -15.1 | -10.0 | -9.5 | -9.3 | -8.8 |
| $Cr(CO)_5$...(β-2-Propanol) | -14.9 | -14.3 | -13.9 | -9.0 | -8.5 | -8.3 | -7.9 |

**Table 3.4** MP2 energies (kcal/mol) for the reaction:
$Cr(CO)_5$ + (Alcohol) → $Cr(CO)_5$(Alcohol) at various correction levels

For example, compared to the $\beta$ carbon, the $\alpha$ carbon in 2-propanol has three electron rich groups (two -CH3 and one -OH group) such that the C-$H_\alpha$ bond has more available electron density to donate to the unsaturated $Cr(CO)_5$ molecule. The calculated values in table 3.4 were used to construct potentials that were used in the Brownian dynamics simulation. The construction of these potentials and the details of the simulation are given in the following sections.

## 3.4 Simulation Engine

The general theory of Brownian dynamics was outlined in section 2 of this chapter. Here, the details of the potential for the model rearrangement and the methods for solution of Langevin's equation are presented.

### 3.4.1 Rearrangement Potential

As mentioned above, the rearrangement of ligands is modeled as a site-diffusion process in which a $Cr(CO)_5$ fragment "hops" from one C-H group to another. For example, the $Cr(CO)_5$ fragment can bind to C-$H_\alpha$, C-$H_\beta$, C-$H_\gamma$ or OH groups of 1-propanol. In our model, the metal complex diffuses in a fluid of these binding sites until it lands on the hydroxyl end of the alcohol, where it

becomes bound. The trajectory for each metal fragment is described by a particle moving along a one-dimensional potential-of-mean-force $V(x)$ that consists of a series of wells which correspond to the unique binding sites mentioned above. The wells are modeled as a series of cosine wells of depth $2U_i$:

$$V(x) = U_i(\cos[(2x+1)\pi]-1), \qquad 3.6$$

where $i$ denotes the different binding sites: C-H($\alpha$, $\beta$, or $\gamma$) or OH[77]. Each well is spaced by 3.2 Å, the Van der Waals radius of a methyl group, taken from simulations carried out in our group and others[36, 78]. In principle, the values for the different $U_i$'s could be determined by fitting the simulation traces to experimental data. As will be seen in the following section, however, the available experimental results for the rearrangement process in the alcohols studied here are convolved with vibrational relaxation. This makes it difficult to quantitatively determine the time-dependent populations of the alkyl and hydroxyl bound metal complexes, especially at early times (<100 ps) following photodissociation of CO from the hexacarbonyl parent molecule.

Although we are not able to directly fit the simulated traces to experimental population dynamics in order to obtain values for the different $U_i$'s in equation 3.6, it is nevertheless possible to discuss qualitative features of the chosen potential model. The ab initio results in table 3.4 indicate that the gas-phase metal-C-H interaction differs with each type of C-H bond. This suggests that the $Cr(CO)_5$ in these simulations may experience a heterogeneous potential energy surface (PES) during the process of intermolecular rearrangement, in which the metal fragment dissociates from one carbon site and re-associates with another one until the metal encounters the strongly-binding hydroxyl site. In solution, the PES is modified by the fluctuating forces from the solvent molecules. Because metal-C-H binding energies are weak (~7-9 kcal/mol), the potential of mean force (PMF) that a $(CO)_5M$(solvent) complex experiences is greatly affected. This manifests itself in observed free-energy barriers of ~5.5-6 kcal/mol ($\Delta G^{\ddagger}$) for the rate-limiting rearrangement step in the silane Si-H bond activation by $M(CO)_5$ (M = Cr, Mo, and W) complexes[4].

In the current study, ab initio binding energies taken from table 3.4 are chosen to represent the

different $U_i$'s. Two different types of potentials are constructed: homogeneous and heterogeneous. In the heterogeneous case, the solution-phase PMF preserves the gas-phase 0.9-1.5 kcal/mol differences in the metal-C-H interaction energies for the different carbon sites. In the homogeneous case, the differences between the C-H sites for each specific solvent molecule are averaged out. In both cases, the absolute gas-phase differences in binding energies between the individual alcohols is preserved, i.e. the differences in the mean C-H binding energies between methanol, ethanol, 1-propanol, and 2-propanol as calculated from table 3.4 are preserved in the simulations. In addition, both potential models have their barriers shifted (by the random fluctuating force) with respect to the vacuum level. Details of how this shifting is accomplished are given below.

### 3.4.2 Numerical Integration of Langevin's Equation

The equations of motion were integrated numerically using two different methods. The first is based on the velocity Verlet algorithm, and the second is similar to Beeman's algorithm[79-81]. Beeman's integrator gives a more accurate equation for the velocities than Verlet's algorithm, and thus an improvement in energy

conservation[80]. Both methods are well known for the integration of Newton's equations of motion in molecular dynamics simulations, and both produced identical results within the error of the simulations. Code for the Verlet algorithm is given in appendix 1.

### 3.4.3 Simulation Parameters

The Brownian dynamics simulations were carried out for the alcohols: methanol, ethanol, 2-propanol, and 1-propanol. Table 3.5 contains various parameters used in the simulations. Assumptions were made as to the exact values for each of the parameters in the simulation. The friction constant, $\gamma$, was chosen such that $\gamma = k_B T / mD$, where $D$ is diffusion coefficient of the liquid[80, 82]. We obtained an expression for $\gamma$ in terms of the particle diameter, $d$, the particle mass, $m$, and the hydrodynamic viscosity, $\eta$:

$$\gamma = \frac{2\pi d\eta}{m}, \qquad 3.7$$

by solving the Navier-Stokes equation subject to "slip" boundary conditions[82]. The slip approximation appears to be valid for larger non-polar solutes in weakly-interacting solvents[83, 84]. Whether or not this is a valid assumption for these simulations will be discussed

| Binding site | $\eta$(cP) | $a$(Å) | $\gamma$(ps$^{-1}$) | $\Delta E_{hetero}$ (kcal/mol) | $\Delta E_{hetero}$ ($k_BT$) | $\Delta E_{homo}$ (kcal/mol) | $\Delta E_{homo}$ ($k_BT$) |
|---|---|---|---|---|---|---|---|
| OH | | | | 57.73 | 23.29 | 58.08 | 23.43 |
| $C^{\alpha}$-methanol | 0.54 | 3.0 | 6.43 | 2.51 | 1.01 | 2.85 | 1.15 |
| $C^{\alpha}$-ethanol | 1.07 | 3.0 | 12.69 | 1.34 | 0.54 | 0.59 | 0.24 |
| $C^{\beta}$-ethanol | | | | 0.05 | 0.02 | 0.59 | 0.24 |
| $C^{\alpha}$-1-propanol | 1.95 | 3.0 | 23.00 | 7.95 | 3.21 | 5.22 | 2.11 |
| $C^{\beta}$-1-propanol | | | | 5.02 | 2.02 | 5.22 | 2.11 |
| $C^{\gamma}$-1-propanol | | | | 1.67 | 0.67 | 5.22 | 2.11 |
| $C^{\alpha}$-2-propanol | 2.04 | 3.0 | 24.10 | 5.44 | 2.19 | 3.27 | 1.32 |
| $C^{\beta}$-2-propanol | | | | 1.67 | 0.67 | 3.27 | 1.32 |

**Table 3.5** Parameters used in the simulation runs. The $\Delta E_{hetero}$ and $\Delta E_{homo}$ are the barriers used in the simulations for the homogeneous and heterogeneous PMF runs, respectively. They were scaled from the values in table 3.4 as outlined in the text.

below. One assumes in the derivation of equation 3.7 that the diffusing particle is spherical. Using Van der Waals radius data along with bond distances from X-ray diffraction, the rough size of $Cr(CO)_6$ can be estimated to fit in a sphere about 8-8.4 Å in diameter. $Cr(CO)_5$, however, is not spherical, and for these simulations, a particle of 6.0 Å diameter was chosen. The bulk solvent viscosity data, in units of centipoise (cP), were taken from standard references[85, 86].

At the start of each simulation, a potential based on equation 3.6 was generated according to the number of unique chemical sites for the alcohol under study. A sample particle is placed in the potential assuming random statistical solvation. For example, figure 3.5 shows a sample heterogeneous potential for 1-propanol. The different wells in the figure correspond to the $C-H_\alpha$, $C-H_\beta$, $C-H_\gamma$, and OH binding sites. We chose two different approaches in counting the different binding sites, one based on the carbons and the other based on the number of hydrogens. If we assume that the number of carbon-sites determines how a particle solvates, then at the beginning of a trajectory, particles have a 25% chance of being randomly placed in the different 1-propanol wells (here

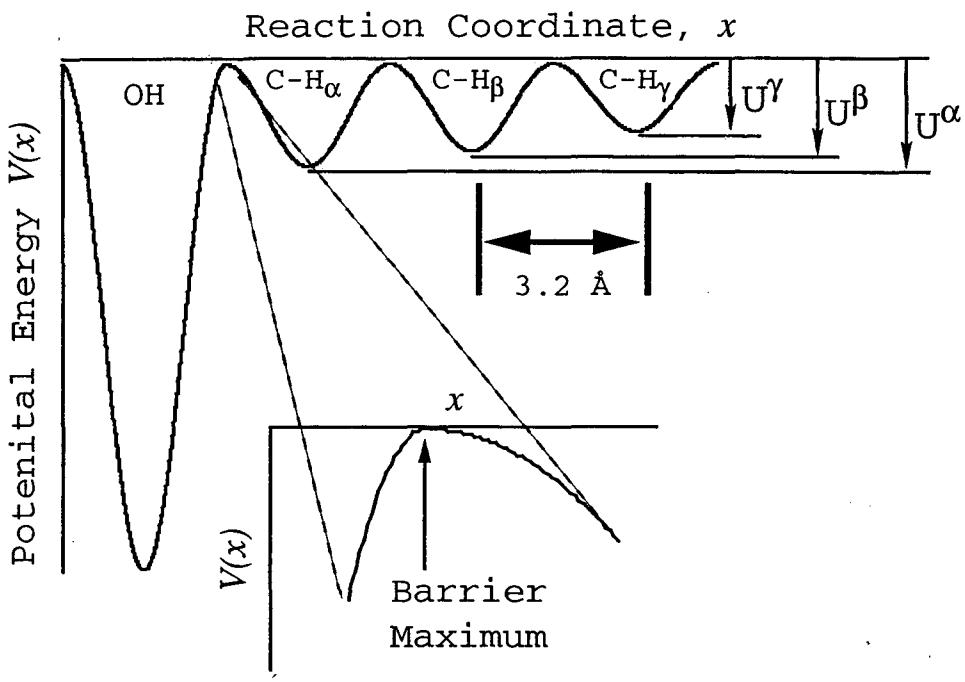


**Figure 3.5** Multi-site cosine potential for 1-propanol given in equation 3.6. The inset shows an expanded view of the potential near the C-$H_\alpha$-hydroxyl barrier.

we assume that the OH counts as a single binding-site). On the other hand, if we assume that it is the number of hydrogen sites that is important, then the particles have a 3/9 chance of binding to the C-$H_\gamma$, 2/9 chance at each of the methylene carbons(C-$H_\beta$ and C-$H_\alpha$), and a 2/9 chance of binding to the OH (because the OH has two lone-pairs of electrons).

The initial velocities of the particles is taken from a Boltzmann distribution at $T = 298.15K$, assuming that vibrational relaxation following solvation does not affect the solvent rearrangement. The Langevin equation is then numerically integrated as outlined above. For the $(CO)_5$Cr-alcohol system with metal-alkane interaction energies $>k_BT$, it is reasonable to separate the dynamics of the rearrangement process (tens to hundreds of picoseconds) from the solvent dynamics (few picoseconds). In this picture, each time a $Cr(CO)_5$ molecule crosses a potential barrier, it is reassigned to a new potential well. In other words, each barrier crossing along the potential $V(x)$ causes the particle to randomly re-solvate along the potential according to the same statistics as the initial PMF setup. This random changing of the potential surface essentially turns the potential into a

random variable, and, as mentioned above, makes the analytic solution for a rate expression, as well as other methods based on the numeric integration of the potential, impossible[62, 87]. Each trajectory is run until the particle becomes bound in the bottom 10% of the hydroxyl well potential. The data analyses were based on 6-10 simulations of 256 independent particles.

It is interesting to note that the random hopping along the potential surface can be removed from the simulation code. When this happens, the diffusing molecule is only allowed to jump to adjacent sites, as in an intramolecular model (see figure 3.1). Such hopping is denoted as non-random throughout the rest of this chapter. To summarize, six types of simulations were run. Three were run on homogeneous potentials, and three were run on heterogeneous potentials. The three on each potential energy surface can be broken into: (1)random hopping based on carbon statistics; (2)random hopping based on hydrogen statistics; and (3)non-random hopping based on carbon statistics.

### 3.5 Simulation Results

Sample simulations for the potential shown in figure 3.4 were run in order to directly compare results

from the numerical integration of equation 3.5 with Kramers' rate equation. These test runs and their fits are presented in appendix 1.

Figure 3.6 shows the normalized population decays of alkyl-bound $Cr(CO)_5$ particles in 1-propanol when modeled with a heterogeneous PMF. This trace exhibits non-single-exponential kinetics. The simulated kinetic traces were fit to the stretched exponential, or Williams-Watts function:

$$\phi(t) \approx e^{-(t/\tau_{WW})^{\beta}} = \int_0^{\infty} e^{-t/\tau} \rho_{WW}(\tau) d\tau , \qquad 3.8$$

where $\rho_{WW}$ is the Williams-Watts distribution function and $\beta_{WW}$ is the parameter characterizing the time-scale distribution, or heterogeneity[88]. The first and second moment of the distribution are given by:

$$\langle \tau \rangle_{WW} = \frac{\tau_{WW}}{\beta_{WW}} \Gamma\left(\frac{1}{\beta_{WW}}\right), \qquad 3.9$$

and

$$\langle \tau^2 \rangle_{WW} = \frac{\tau_{WW}^2}{\beta_{WW}} \frac{\Gamma(2/\beta_{WW})}{\Gamma(2)}, \qquad 3.10$$

where $\Gamma$ us the gamma function[88].

The femtosecond infrared spectra for the rearrangement of alcohols at a coordinatively unsaturated

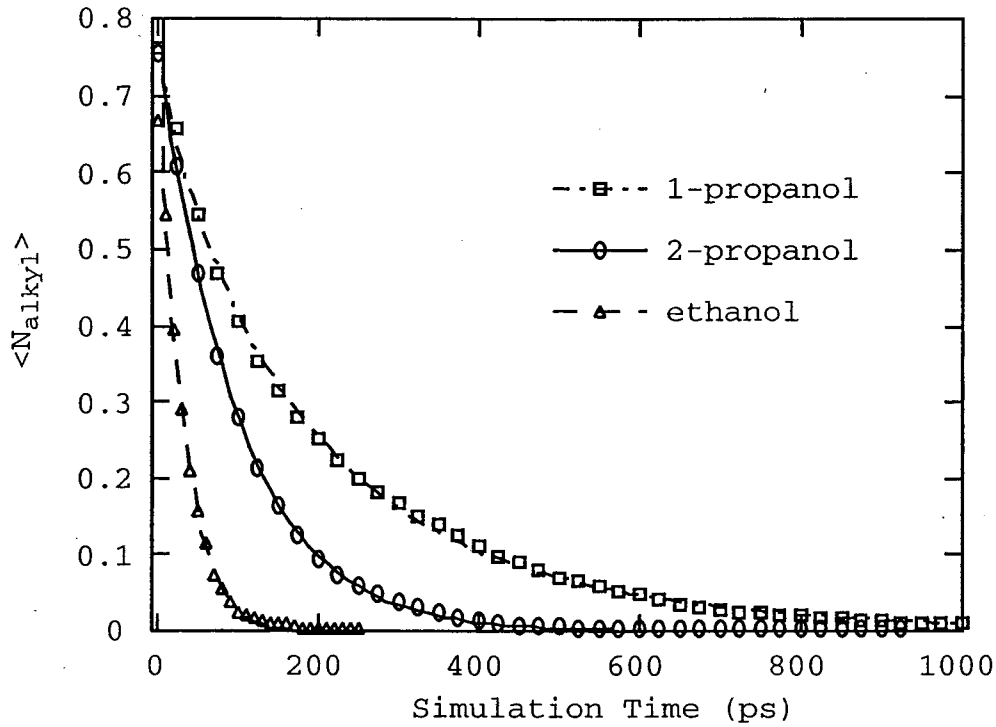


**Figure 3.6** Simulation decay traces and fits to the Williams-Watts fitting function for the alcohols: 1-propanol, 2-propanol, and ethanol. Simulations were run with random carbon hopping statistics and a heterogeneous PMF. The fit parameters can be found in table 3.7

$Cr(CO)_5$ molecule were presented in chapter 1. The kinetics for the alkyl and the hydroxyl bound peaks are shown in figure 3.7. The data were fit to both the Williams-Watts function (equation 3.8), as well as a bi-exponential function:

$$\Delta A(t) = a_1 e^{-t/\tau_1} + a_2 e^{-t/\tau 2}. \qquad 3.11$$

The fit parameters for the experimental data appear in table 3.6. The data in figure 3.7 had poor signal-to-noise (S/N), giving rise to the large error bars in the fit parameters, but a number of conclusions can be made from the fits. The first is that the data for both propanols have a short time component (<50 ps) followed by a long time component (100-200 ps). This short decay is most likely due to vibrational relaxation, as discussed in the previous chapter and other papers[1, 3, 4, 17, 39]. This suggests that the short-time relaxation component in 2-propanol could be due to vibrational relaxation of initially generated photoproducts. It must be noted, however, that the kinetics of 1-propanol show an initial fast *decay* followed by a long-time rise in the hydroxyl E-band. This short decay is probably due to overlap of the E-band with a $\nu=2\leftarrow1$ hot-band of the parent

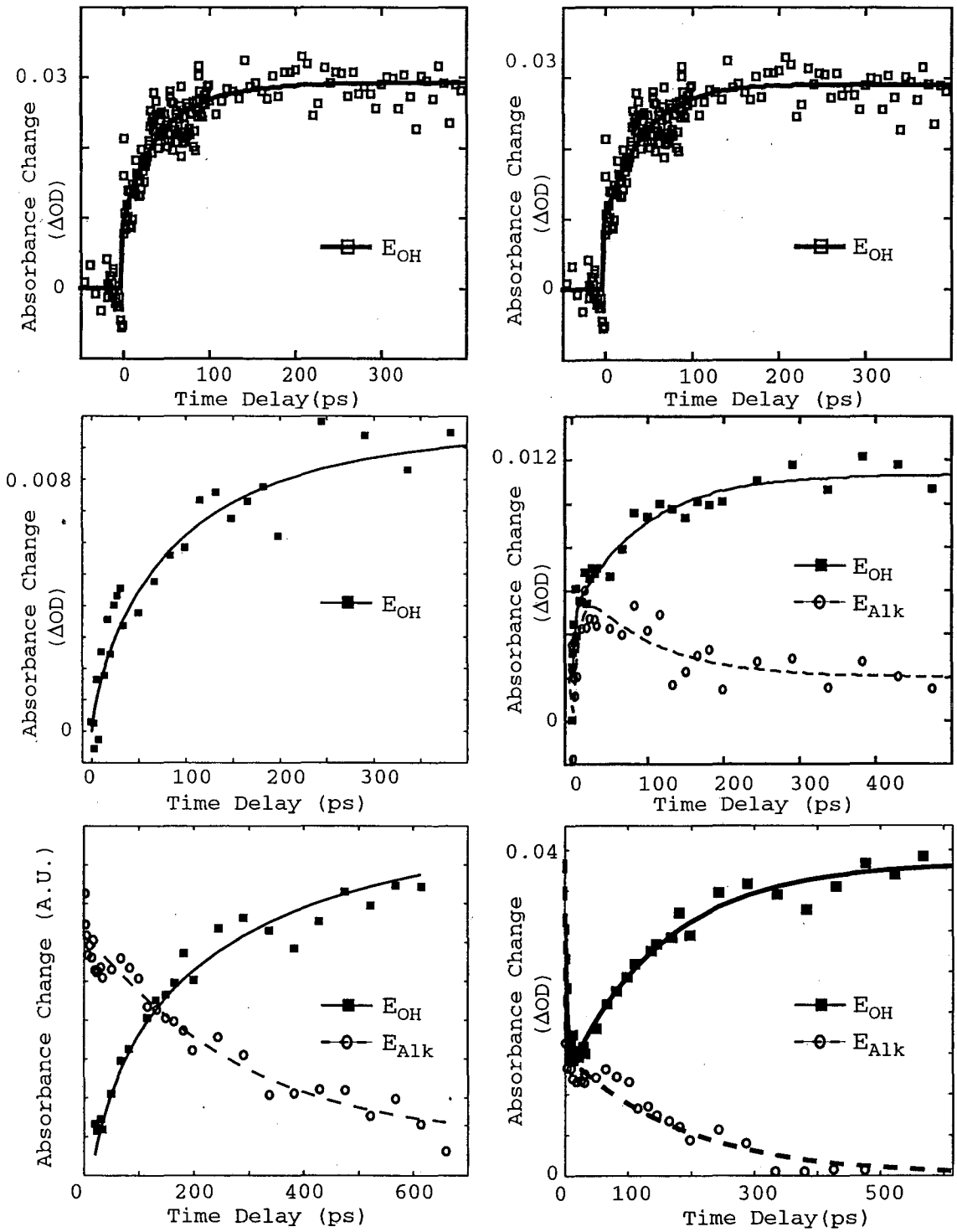


**Figure 3.7** Picosecond infrared kinetics of $Cr(CO)_5$ in ethanol(top), 2-propanol(middle), and 1-propanol(bottom). Figures on the left have been fit to the Williams-Watts function, those on the right to a bi-exponential function

Bi-Exponential Fits

| Alcohol | Band | $\tau_1$ (ps) $\pm \sigma(\tau_1)$ | $\tau_2$ (ps) $\pm \sigma(\tau_2)$ |
|---|---|---|---|
| Ethanol | hydroxyl E | 45 ± 9 | |
| 2-Propanol | hydroxyl E | 92 ± 17 | 2 ± 1 |
| 2-Propanol | alkyl E | 95 ± 38 | 9 ± 4 |
| 1-Propanol | hydroxyl E | 153 ± 32 | 4.4 ± 1.5 |
| 1-Propanol | alkyl E | 189 ± 9 | 1.0 ± 0.3 |

Williams-Watts Fits

| Alcohol | Band | $\tau$ (ps) $\pm \sigma(\tau)$ | $\beta \pm \sigma(\beta)$ | $\langle\tau\rangle$ | $\langle\tau^2\rangle$ | $\delta\tau$ |
|---|---|---|---|---|---|---|
| Ethanol | hydroxyl E | 42 ± 5 | 0.9 ± 0.1 | 46.2 | 2.5E+03 | 20 |
| 2-Propanol | hydroxyl E | 94 ± 35 | 0.7 ± 0.1 | 113.3 | 1.9E+04 | 76 |
| 1-Propanol | hydroxyl E | 177 ± 31 | 0.6 ± 0.1 | 301.3 | 2.2E+05 | 360 |
| 1-Propanol | alkyl E | 275 ± 37 | 1.1 ± 0.2 | 268.8 | 6.8E+04 | - |

**Table 3.6** Fits to the experimental femtosecond infrared data for the photolysis of $Cr(CO)_6$ in alcohols

hexacarbonyl. Another feature of the fits is the apparent kinetic coupling of the alkyl E-band decay to the hydroxyl E-band growth. This supports the idea of rearrangement of the alkyl-bound photoproducts to the stable hydroxyl-bound species as was thoroughly discussed in the previous chapter.

The experimental kinetic traces when fit to the Williams-Watts function all display heterogeneity in the distribution of time-scales ($\delta t$, given in table 3.6). This heterogeneity is due to the non-single-exponential behavior of the relaxation kinetics, but unfortunately we can not say for certain whether or not this heterogeneity is solely due to vibrational relaxation or due to the heterogeneity in the rearrangement process itself. This is because we can not accurately deconvolve the kinetics from the vibrational relaxation processes that contribute to them.

The potential well depths in the simulations were scaled such that the simulation traces for 2-propanol roughly matched the rearrangement times as measured with the femtosecond infrared apparatus. This was accomplished by varying the average 2-propanol binding energy in a series of simulations, as shown in

figure 3.8. The average barrier that corresponded to a 100 picosecond decay was then chosen as a reference energy. The binding energies of all the other alcohols energies were then scaled to this reference by simply adding the differences between gas-phase ab initio energies of the alcohol (ethanol or 1-propanol) and 2-propanol. This process is depicted in figure 3.9 for a heterogeneous potential. These scaled energies for the different alcohols, which appear in table 3.5, were then plugged into the simulation engine. The resulting fits of the decay traces to the Williams-Watts function are listed in table 3.7.

### 3.6 Discussion

There are a number of trends that can been seen in the simulation data of table 3.7. The obvious trend is that the mean relaxation times in the simulation, $<\tau>_{WW}$, match well with experimental fits found in table 3.6. This suggests that the site-specific binding energies between the alcohols leads to the differences in relaxation times amongst the alcohols ethanol, 1-propanol, and 2-propanol. This furthermore supports the theory that the rearrangement proceeds via a dissociative mechanism. It was not possible to observe a

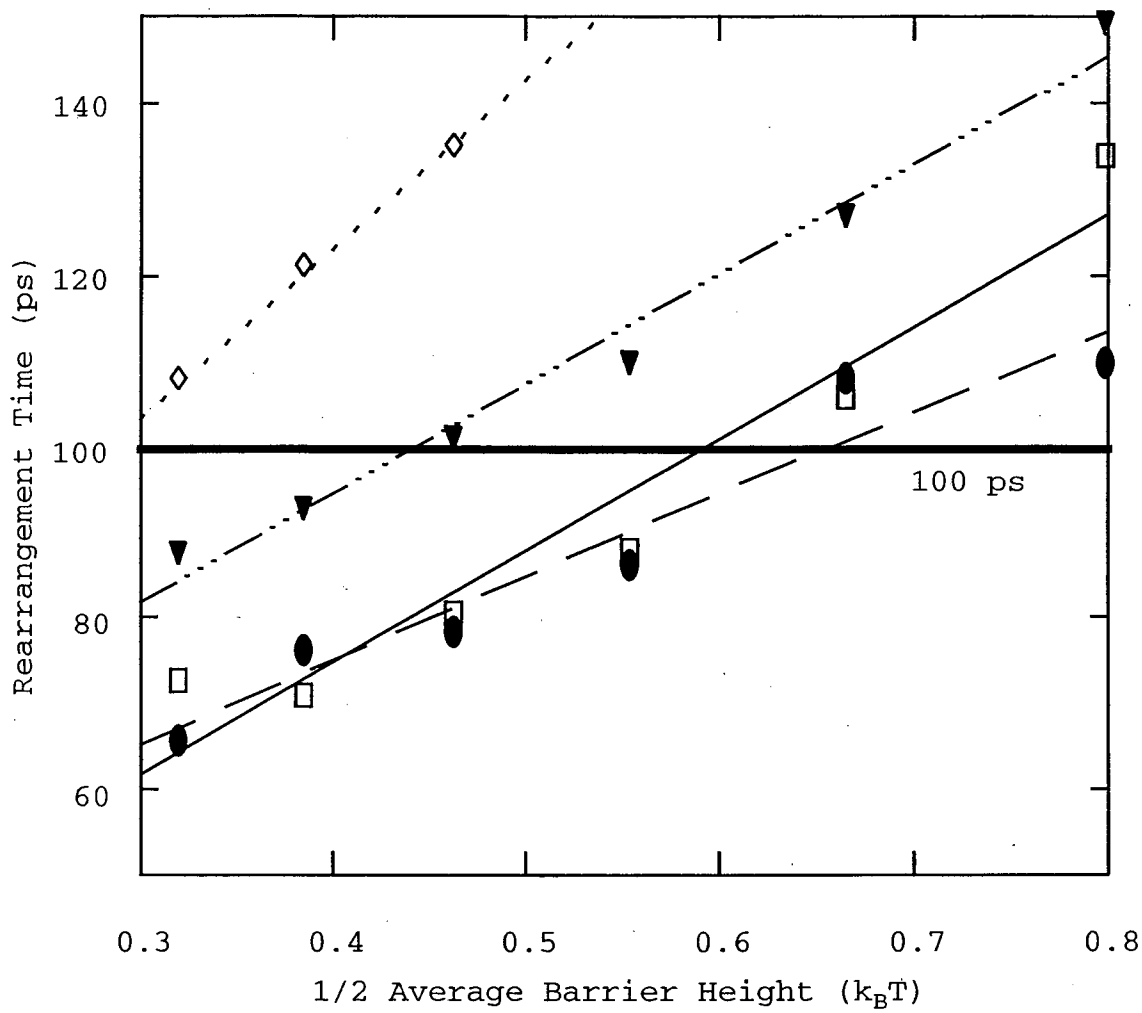


**Figure 3.8** Rearrangement times for 2-propanol versus average barrier height for random carbon statistics with a heterogeneous PMF, —□—; random carbon statistics with a homogeneous PMF, —●-; non-random carbon statistics with a heterogeneous PMF, - - ◇ - -; non-random carbon statistics with a homogeneous PMF, —▼- - -. Lines through the data points are least-squares linear fits.

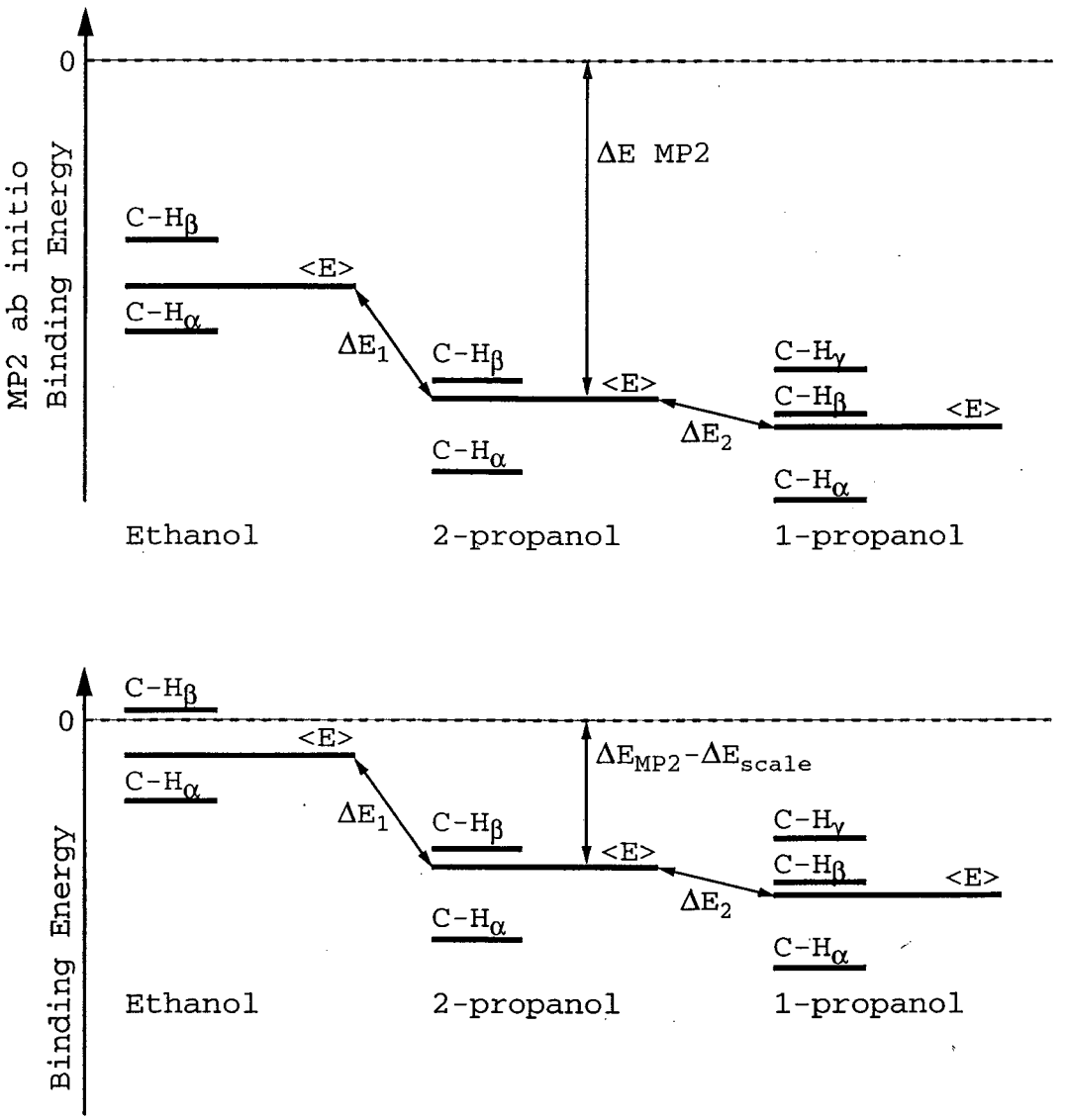


**Figure 3.9** Scheme demonstrating the scaling of the alcohol potentials. The top figure shows the energy levels determined from ab initio MP2 calculations. In the bottom diagram, the 2-propanol barrier has been scaled by $\Delta E_{scale}$. The other alcohols have been scaled the same amount, keeping the differences $\Delta E_1$ and $\Delta E_2$ constant. In the heterogeneous PMF, the differences between the unique sites, C-$H_\alpha$, C-$H_\beta$, and C-$H_\gamma$, and the average energy, <E>, have been preserved.

| Alcohol | $\tau_{WW} \pm \sigma(\tau_{WW})$ | $\beta_{WW} \pm \sigma(\beta_{WW})$ | $<\tau>$ | $<\tau^2>$ | $\delta\tau$ |
|---|---|---|---|---|---|
| **Heterogeneous Potentials** | | | | | |
| *Random Carbon Statistics* | | | | | |
| Methanol | 20.2 ± 0.7 | 0.99 ± 0.07 | 20.2 | 4.1E+02 | 2 |
| Ethanol | 32.3 ± 1.1 | 1.00 ± 0.06 | 32.3 | 1.0E+03 | 2 |
| 2-Propanol | 95.5 ± 1.2 | 0.99 ± 0.02 | 96.0 | 9.3E+03 | 11 |
| 1-Propanol | 165.0 ± 3.3 | 0.80 ± 0.01 | 187.1 | 4.5E+04 | 102 |
| *Random Hydrogen Statistics* | | | | | |
| Ethanol | 36.8 ± 0.6 | 1.00 ± 0.03 | 36.9 | 1.4E+03 | 1 |
| 2-Propanol | 101.2 ± 1.0 | 1.00 ± 0.02 | 101.2 | 1.0E+04 | 2 |
| 1-Propanol | 176.4 ± 4.1 | 0.83 ± 0.02 | 195.6 | 4.8E+04 | 96 |
| *Non-Random Carbon Statistics* | | | | | |
| Methanol | 13.4 ± 0.7 | 0.98 ± 0.08 | 13.5 | 1.9E+02 | 2 |
| Ethanol | 40.5 ± 0.5 | 1.00 ± 0.02 | 40.5 | 1.6E+03 | 0 |
| 2-Propanol | 137.3 ± 2.9 | 0.96 ± 0.02 | 140.0 | 2.0E+04 | 30 |
| 1-Propanol | 386.2 ± 6.1 | 0.94 ± 0.01 | 397.2 | 1.7E+05 | 102 |
| **Homogeneous Potentials** | | | | | |
| *Random Carbon Statistics* | | | | | |
| Methanol | 20.2 ± 0.7 | 0.99 ± 0.07 | 20.2 | 4.1E+02 | 2 |
| Ethanol | 33.6 ± 0.8 | 1.00 ± 0.05 | 33.7 | 1.1E+03 | 2 |
| 2-Propanol | 95.8 ± 1.1 | 1.00 ± 0.02 | 95.9 | 9.2E+03 | 5 |
| 1-Propanol | 152.1 ± 2.4 | 0.99 ± 0.03 | 152.5 | 2.3E+04 | 13 |
| *Random Hydrogen Statistics* | | | | | |
| Ethanol | 35.5 ± 0.8 | 1.00 ± 0.04 | 35.5 | 1.3E+03 | 2 |
| 2-Propanol | 103.7 ± 1.0 | 1.00 ± 0.02 | 103.8 | 1.1E+04 | 3 |
| 1-Propanol | 162.6 ± 2.7 | 0.95 ± 0.01 | 166.7 | 2.9E+04 | 40 |
| *Non-Random Carbon Statistics* | | | | | |
| Methanol | 13.4 ± 0.7 | 0.98 ± 0.08 | 13.5 | 1.9E+02 | 2 |
| Ethanol | 35.7 ± 1.0 | 1.00 ± 0.05 | 35.7 | 1.3E+03 | 2 |
| 2-Propanol | 127.4 ± 2.0 | 0.99 ± 0.02 | 127.9 | 1.6E+04 | 12 |
| 1-Propanol | 307.2 ± 5.0 | 0.97 ± 0.02 | 311.0 | 9.9E+04 | 53 |

**Table 3.7** Williams-Watts fitting parameters from the stochastic simulations of the $Cr(CO)_5$alcohol systems. All relaxation times are given in picoseconds. The width of the time-scale distribution is given by, $\delta\tau = \sqrt{\langle\tau^2\rangle - \langle\tau\rangle^2}$ .

significant change between the random-carbon and random-hydrogen solvation statistics, and thus the exact statistical nature the solvation process with respect to the nature of the binding-sites could not be determined.

One interesting observation, with respect to rearrangement times, is the extremely rapid rearrangement in ethanol. The simulation predicts that rearrangement occurs within 30-40 ps. This is consistent with the observed 42 ps recovery shown in figure 3.8. It also explains the absence of the alkyl peak from the ethanol data. As mentioned previously, it can be difficult to measure the presence of a molecular species when it is highly vibrationally excited. This is because many vibrational hot-bands can be excited, the molecule can couple to low-frequency modes, and many other bands can generally overlap with the peak of interest, and thus our experimental measurement is coupled to the vibrational relaxation process. The time-scale for vibrational cooling is on the order of 20-100 ps for these group 6 metal hexacarbonyl systems, and if the model is correct, we may not be able to observe the alkyl peak since it decays away on a time-scale roughly the same as the vibrational relaxation process.

Another observation is that the $\beta$ parameters for the heterogeneous PMF are generally < 1, but in the simulations with a homogeneous PMF, the simulation traces appear to be single-exponential ($\beta_{WW}$~1 in table 3.7). This latter observation is expected for such a homogeneous medium. The widths of the time-scale distributions, $\delta\tau$, from table 3.7 are greater for the 1-propanol systems than for the other alcohols. This can be understood by the fact that there are three different carbon sites, whereas ethanol or 2-propanol have only two unique carbon binding sites.

One weakness in the model is the scaling the potentials. As can be seen from table 3.5, the barriers for the simulation runs had to be scaled to extremely low values. Furthermore, in preserving the spacing between the unique carbon sites, the C-$H_\beta$ potential barrier in ethanol became unbound (positive in energy) for all the heterogeneous PMF simulations. These latter simulations were run with effective potential energy barrier of 0.01 $k_BT$ for this C-$H_\beta$ site. The physical interpretation for this, however, is that the C-$H_\beta$ energy level does not really bind to the $Cr(CO)_5$ complex, and thus ethanol does not randomly solvate. The resulting kinetics are

remarkably similar to those of methanol, which has only two binding sites. It should be noted that the simulations employing the intramolecular rearrangement mechanism (non-random hopping), based on carbon statistics were not scaled low-enough in energy to give a 100 ps decay for the 2-propanol runs. If we had attempted this, both ethanol sites would have become nearly unbound ($\Delta E_{binding} \leq 0.02\ k_B T$). Another scaling method could be employed, perhaps one which also scales the energy spacing between the sites each alcohol or one in which the energy is scaled with a constant multiplicative factor. We could also consider re-calculating the ab initio results with larger basis sets or different methods in an effort to obtain more accurate gas-phase energies upon which to base our potential energy surfaces. This, however, would still require an ad hoc method for scaling the energies as discussed above.

The simulations, however, provide insight into the differences between the random-carbon and non-random-carbon (inter vs. intramolecular) hopping mechanisms. The simulations were run with friction constants of $4\ ps^{-1} \leq \gamma \leq 24\ ps^{-1}$, and barriers on the order of 0.5-1 $k_B T$. The potential curvature, $\omega_b$, is defined as:

$$\omega_b = \sqrt{\frac{2}{m} V''(x)\big|_{x=barrier}}\,, \qquad 3.12$$

$$\omega_b = \left(\frac{2\pi}{l}\right)\sqrt{\frac{2U_i}{m}}\,, \qquad 3.13$$

where $m$ is the particle mass, $l$ is the spacing between the cosine wells, and $U_i$ is the well depth. It can be seen that the maximum value that $\omega_b$ could take would be on the order of 3 $ps^{-1}$, and thus the propanol runs lie in the over-damped regime ($\gamma >> \omega_b$) [89]. In this strong-friction regime, Kramers' result predicts that the rate $\propto 1/\gamma$ [62]. The results in table 3.7 can be scaled by the viscosity in order to compare the differences between 1-propanol and 2-propanol for the non-random hopping simulations. One finds that if the 2-propanol relaxation time is scaled to 100 ps, the resulting 1-propanol rearrangement takes place on a time scale of 250 ps, which is significantly larger than the experimental result of 150-200 ps. This furthermore suggests that the rearrangement mechanism is dissociative in nature.

### 3.7 Conclusions and Future Development of the Model

The results presented in this chapter and the previous one have shown that the rearrangement of ligands at transition metal complexes most likely proceeds through an intermolecular mechanism. More work needs to

be done, however, to determine whether the rearrangement dynamics can be described as diffusive motion along a simple (or complex) one-dimensional potential energy surface. There are many unanswered questions and assumptions in the present model which need to be addressed further. These include the parameters for the PMF and the friction. Future work could focus on determining more realistic parameters for the hopping distance, the particle size, and scaling of the potential energy surface. The exact statistics of the hopping can also be altered to take into account possible non-random or preferential solvation amongst the sites. It was mentioned above that we assumed the vibrational relaxation of the $Cr(CO)_5$ molecule does not affect the rearrangement dynamics. This could be explored more carefully by allowing the particle or the surrounding solvent molecules to change temperature throughout the simulation. The computer code can easily be modified to incorporate all these changes.

We would also like to address the generality of this model. Further site-specific ab initio calculations are needed on other systems for which we currently have experimental data, including: the rearrangement of

silanes at group 6 hexacarbonyls and $Cr(CO)_5$ in 1-hexanol. It will be interesting to see if the model can be extended to include larger solvent molecules that have much longer solvent-rearrangement times (ns and longer). In addition, the experimental data in figure 3.8 had a very low S/N ratio. Perhaps with more accurate data, we can better evaluate our rearrangement model.

# Chapter 4

# Design and Construction of a Femtosecond Ti:Sapphire Laser System

## 4.1 Introduction

The dye laser system that was used to collect the data presented in chapters 2 and 3 was a difficult system to use. The basic design suffered from two main limitations. The first was the noise of the IR probe signal. The peak-to-peak root mean squared noise was consistently measured at 30%. With a repetition rate of only 30 Hz, multiple days (or weeks) of data collection were required in order to obtain a single kinetic trace. The time required to obtain such a trace limited our overall signal detection limits to about 2-5 mOD. The smallest signal that was ever observed on this system had a measured absorption change of 1 mOD, and it was not possible to obtain kinetics for this peak.

The second limitation of the dye system was due to the liquid dye amplifiers themselves. The original design of the laser incorporated a complex dye

amplification system which, in theory, could be tuned simply by changing dyes. In practice, however, the residual dye remained in the system, and efficiency at newly introduced dyes was never achieved. The reasons for this were probably threefold. First, the stimulated emission cross-section is unique for each dye. The laser beam size must be the correct size with the correct energy density in order to obtain optimum amplification[90, 91]. The amplification stages used in this laser were rarely adjusted when dyes were changed, and never optimized for each individual dye. Secondly, the residual dye in the system as well as the other contaminates in the system could perhaps have acted as fluorescence quenchers for the dye solution. Lastly, the pump laser used to pump the dyes had a poor spatial mode, and was not energetic enough to saturate all the amplifiers, thus further contributing to noise in the system.

Solid-state laser systems have distinct advantages over dye systems. They are extremely low-maintenance, they can be very compact, and they are not plagued with issues such as dye circulation, concentration, and contamination. Solid-state laser materials typically

have much higher saturation fluences, and high damage thresholds[92]. With the advent of chirped-pulse-amplification (CPA), solid-state laser amplifiers became extremely practical devices for the amplification of ultrafast laser pulses[93]. The idea of CPA is to increase the energy of an ultrafast pulse while at the same time avoiding optical damage due to extremely high energy densities. This is achieved by broadening the pulse in time by applying a frequency chirp[94, 95]. The lengthening of the pulse in time lowers the peak power of the pulse to limits that avoid optical damage in the amplifier. Following amplification, the broadened pulse is recompressed back to femtosecond duration.

Many groups have developed all-solid-state femtosecond laser systems, and the reader is referred to an excellent review of solid-state laser technology by Backus et al.[5]. The laser system built in our lab is based on a design from former Professor Yongqin Chen's group at UC Berkeley[96]. A schematic of the laser system is shown in figure 4.1. It consists of a Ti:sapphire oscillator, a stretcher, a Ti:sapphire regenerative amplifier, a compressor, and a pump laser

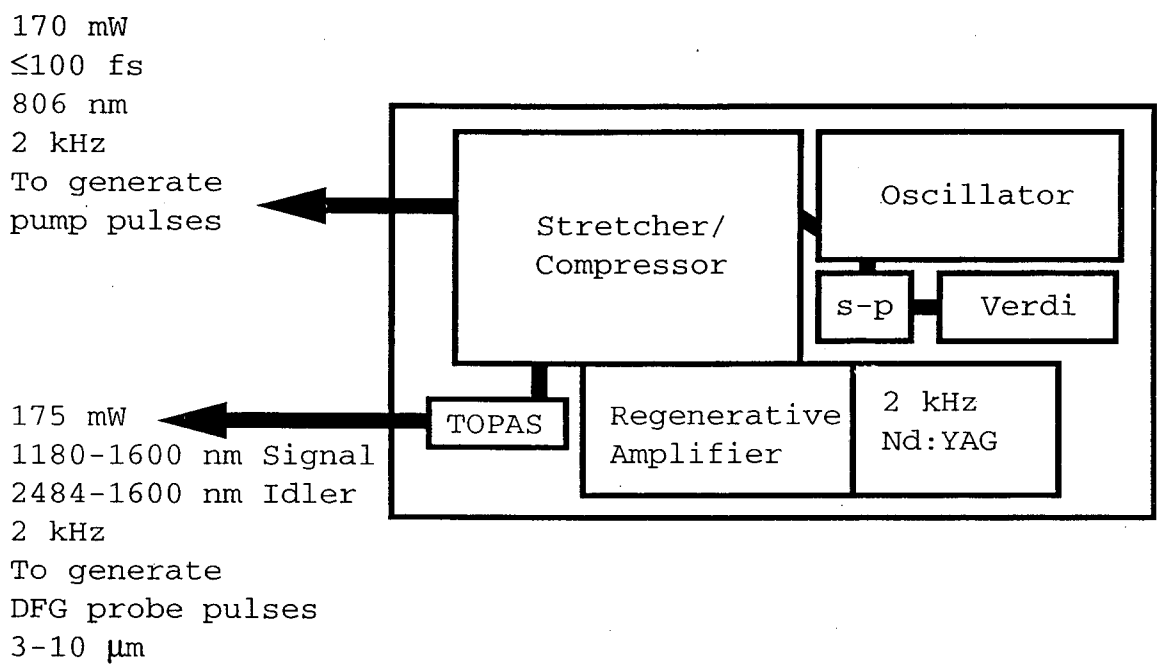


**Figure 4.1** Overview of the solid-state femtosecond laser system

for the amplifier. The rest of this chapter will discuss the design, construction and operation of these elements.

## 4.2 Ti:Sapphire Femtosecond Oscillator

Titanium-doped sapphire is an ideal solid-state laser material. It exhibits a gain bandwidth from 700 nm to 1100nm, with a maximum of 790 nm, and it has high thermal conductivity[92]. Furthermore, in 1990, Spence et al. were able to generate 60 fs laser pulses with Ti:sapphire without the use of any active or passive mode-locking components, such as acousto-optic crystals or saturable absorber jets, respectively[97]. The mechanism for this self-mode-locking is due to the intensity-dependent index of refraction in Ti:sapphire. The Kerr nonlinearity of the laser crystal results in self-focusing of the internal cavity modes at high focused light intensities leading to unique mode shapes for cw and pulsed modes. The laser cavity can thus be designed to favor cw or pulsed, mode-locked operation by favoring one spatial mode over the other.

The Ti:sapphire femtosecond master oscillator used in our system (figure 4.2) was based on the design from the Murnane and Kapteyn group[98]; the reader is referred to table 4.1 for detailed descriptions of the optical

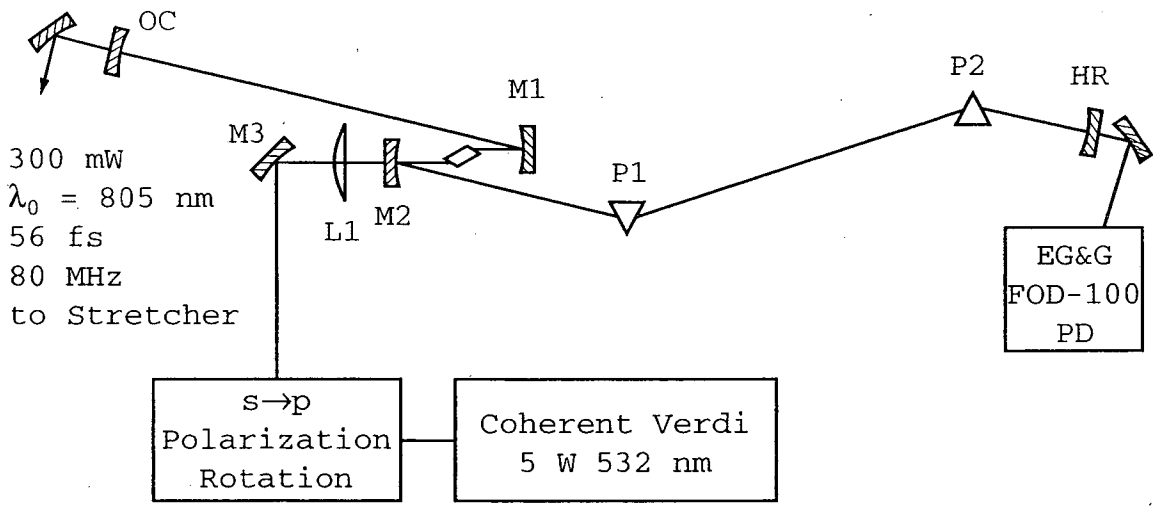


**Figure 4.2** Femtosecond Ti:sapphire oscillator (not to scale)

| Optic | Description |
|---|---|
| OC | 90% Reflective output coupler centered at 800 nm |
| M1, M2 | High power pump mirror; >99% reflectivity at 800 nm, AR coated 400-550 nm |
| crystal | Ti:sapphire crystal; Length 4.75 mm, FOM > 300, n = 1.76, $\theta_{brewster}$ = 60.3°, 0.15% Titanium doped $Al_2O_3$ by weight |
| P1, P2 | Fused silica prisms, Cut at 69.0° |
| HR | Single stack high power reflector; >99% reflectivity centered at 800 nm |
| L1 | 12.5 cm fl plano-convex lens, AR coated 400-550 nm |
| M3 | Protected aluminum mirror |
| s→p | Polarization Rotator, protected aluminum mirrors |

**Table 4.1** Optics legend for the Ti:sapphire oscillator

| Optical Path Length | Distance Between Optics (cm) |
|---|---|
| OC-M1 | 60.1 |
| M1-crystal | 5.3 |
| crystal-M2 | 5.2 |
| M2-P1 | 30.0 |
| P1-P2 | 57.5 |
| P2-HR | 10.5 |
| L1-crystal | 14.0 |

**Table 4.2** Optical path lengths for the the Ti:sapphire oscillator

components. The Ti:sapphire laser has a standard z-shape cavity composed of four mirrors, two prisms, and the laser crystal itself. The short Ti:sapphire crystal (Atramet) is placed between two curved mirrors (Spectra-Physics) and is pumped by 5 W of 532 nm light from a diode-pumped, intra-cavity doubled Nd:YVO laser (Coherent Verdi 5W). The polarization of the Verdi output is rotated by 90° with a pair of mirrors (Newport) and then focused through one of the curved mirrors into the Ti:sapphire crystal with a 12.5 cm focal length (f.l.) lens (Newport). The two arms of laser cavity on either side of the curved mirrors are of different lengths. The longer arm contains the two prisms (R. Matthews Optical Works) and a high reflector (CVI). The shorter arm contains the 10% output coupler (CVI). The curved mirrors, the crystal, and the lens are placed on a precision optical rail. By adjusting the distance between the optics along this rail, one can change the focal parameters of the cavity in order to favor the cw or the pulsed, mode-locked mode as will be described below.

### 4.2.1 Alignment of the Ti:sapphire Oscillator

The basic design and alignment of the laser is outlined in a technical communication from the Murnane and Kapteyn group[98]. The precise distances between the optics outlined in this aforementioned paper have been altered in our laser and are listed in table 4.2. The cavity alignment proceeds as follows.

1. First, the cw laser output power is maximized to approximately 600 mW. In this configuration, the cw cavity mode should be spatially overlapped with the pump beam in the vertical and horizontal direction, and it should diverge upon exiting the output coupler. Translating the curved mirror, M1 with respect to M2, controls the collimation of the beam and the general beam shape. When adjusting M1, it is necessary to optimize the position of the crystal between the M1 and M2, as well as the distance between L1 and the crystal.

2. The prism, P1, closest to the laser crystal is then translated such that the apex of the prism is clipping the cw beam. This reduces the output power to approximately 250-300 mW, and it changes the shape of the cw mode. The prism, P2, closest to the high reflector is then translated so that its apex begins to tune the

cavity frequency to the red. At this point, the cavity is ready to be mode-locked.

3. Mode-locking in this laser is not self-starting and requires an external noise spike. This is accomplished by translating either prism in and out of the beam (push the prism translation stage and let go). Optimization of the cavity for stable mode-locked operation is accomplished by adjusting P1, P2, the distance between M1 and M2, and the position of the crystal between M1 and M2. The P1 adjustment is the major adjustment for favoring the mode-locked mode to the cw mode. The P2 adjustment changes the amount of dispersion compensation in the cavity and thus affects stability and bandwidth of the laser output. The high reflector and output coupler adjust power and mode overlap between the cavity mode and the pump laser. The position of the crystal between the mirrors mainly changes mode-locked pulse stability and power.

4. Wavelength tuning is accomplished by placing razor blades that are mounted on translation stages on either side of the beam between P2 and the high reflector. Translating the razor blades on either side of the beam effectively cuts out either the blue or red end of the

spectrum and shifts the center wavelength. The high reflector and prism, P2, need to be optimized after adjusting the cavity spectrum with the razor blades.

When the cavity alignment is optimized, the mode-locked mode is near $TEM_{00}$, is smaller than the cw mode, and has approximately 5-10% greater average power output than the cw mode. The mode-locked laser operates at 88.1 MHz, with an average power between 280 and 340 mW. Peak-to-peak power fluctuations of 1-2% are measured with a fast photodiode (EG&G FOD-100, -90V Bias; < 1ns rise-time) and a digital oscilloscope (Tektronix). The pulse width is typically 60-70 fs, but can be recompressed further with a prism pair outside the cavity. The center wavelength of the mode-locked pulse is most stable and gives the highest power when the cavity is tuned to 806 nm. Once started, the laser will remain mode-locked for at least an entire day. Long-term power drifts and instability in the oscillator occur when the room temperature shifts throughout the day. Dust and air currents also affect laser stability. To minimize dust, an air filter (Envirco, MAC 10, 2x4 ft. HEPA filter) is mounted above the laser table, and to minimize air currents, the laser is further enclosed in a box.

Using the plans from the Murnane and Kapteyn group, an oscillator can easily be assembled and optimized for mode-locked operation within a week. Daily alignment consists mainly of adjusting the cavity high-reflector and the translation of the prisms in order to optimize the mode-locked power. This day-to-day alignment requires approximately 10-15 minutes after the Verdi pump laser has warmed-up (~20 minutes).

### 4.3 Pulse Stretcher and Compressor

As discussed in section 4.1, the femtosecond pulses from the oscillator are broadened in the time domain before amplification. This pulse broadening is accomplished using dispersive optics such as grating and prism pairs. The concepts behind dispersive pulse shaping are thoroughly discussed in a number of papers, texts, and recent reviews on ultrafast laser spectroscopy[5, 94, 95, 99-102]. The basic idea of pulse broadening will be discussed below.

Due to the uncertainty principle, ultrafast optical pulses have a finite, broad spectral bandwidth. For Gaussian-shaped pulses of the form:

$$E(t) = \xi_0 e^{-(t/\tau_G)^2} e^{i\omega_0 t}, \qquad 4.1$$

where $\omega_0$ is the center carrier frequency of the pulse, $\tau_G$ is the Gaussian pulse width, and $\xi_0$ is the electric field intensity, it can be shown that[99]:

$$\Delta\nu \cdot \tau_p \geq 0.441, \qquad 4.2$$

where $\tau_p$ and $\Delta\nu$ are the FWHM of the Gaussian intensity and spectral envelopes, respectively, and $\tau_p$ is just $\sqrt{2\ln 2}\tau_G$. The Fourier transform of equation 4.1 describes the ultrafast Gaussian pulse in the spectral domain:

$$S(\omega) = \int_{-\infty}^{\infty} E(t)e^{-i\omega t}dt = s(\omega)e^{i\sigma(\omega)}, \qquad 4.3$$

where $s(\omega)$ is the spectral amplitude and $\sigma(\omega)$ is the spectral phase of the pulse. The effect of dispersive optics on the pulse can then conveniently be described with the optical transfer equation:

$$S'(\omega) = S(\omega)H(\omega) = s(\omega)h(\omega)e^{i[\sigma(\omega)+\eta(\omega)]}. \qquad 4.4$$

Here, $S(\omega)$ is the spectral description of the input Gaussian pulse and $S'(\omega)$ is the pulse after it has passed through an optical system with an optical transfer function $H(\omega)$. The resultant pulse can then be described in the time domain through the reverse Fourier transform of $S'(\omega)$. It can be seen that it is the spectral phase of

the optical system, $\eta(\omega)$ which leads to pulse broadening in the time domain[99].

As mentioned above, pulse stretching and compression is done with dispersive optics. To properly describe temporal pulse shaping with equations 4.1-4.4 it is necessary to have the correct spectral phase functions of the optical transfer functions for the stretcher and compressor. Commonly, all that is required is a Taylor series expansion of the spectral phase function around the carrier frequency $\omega_0$:

$$\phi(\omega) = \phi(\omega_0) + \phi'(\omega)(\omega - \omega_0) + \frac{1}{2}\phi''(\omega)(\omega - \omega_0)^2 + \frac{1}{6}\phi'''(\omega)(\omega - \omega_0)^3 + \ldots \qquad 4.5$$

In the equation above, $\phi'$, $\phi''$, and $\phi'''$ are derivatives of the spectral phase function, $\phi(\omega)$, with respect to frequency and are referred to as the group delay, the group velocity dispersion (GVD), third-order dispersion (TOD), etc.

The details for a grating compressor were worked out by Treacy in 1969[95], and convenient expressions for spectral dispersion out to fourth order can be found elsewhere in the literature[5]. Treacy found that the GVD introduced with a grating pair was always negative.

Martinez, however, later determined that the sign of the dispersion in a grating pair could be controlled by placing a telescope between the gratings[94]. A schematic of this telescopic system is shown in figure 4.3. It can be shown that the GVD introduced by this configuration is:

$$\phi''\big|_{\omega_0} = -\frac{\omega_0}{c}\left(\frac{d\alpha}{d\omega}\bigg|_{\omega_0}\right)^2 (2z), \qquad 4.6$$

where c is the speed of light, and $d\alpha/d\omega$ is the angular dispersion of the grating. The point of dispersion at the grating surface, z in the above equation, is defined with respect to the focal points of the lenses in figure 4.3. If the grating surface is placed between the lens and f, its focal point, then z is defined as negative, and a positive GVD results from equation 4.6.

A schematic of the actual stretcher used in our solid-state laser system appears in figure 4.4. The stretcher employs all-reflective optics, described in table 4.3, in order to minimize dispersion. The stretcher also uses a large diameter parabolic mirror (Edmund Scientific) instead of lenses in order to avoid spherical aberations. The system is folded with the folding mirror, FM (JML Optics). This allows us to use

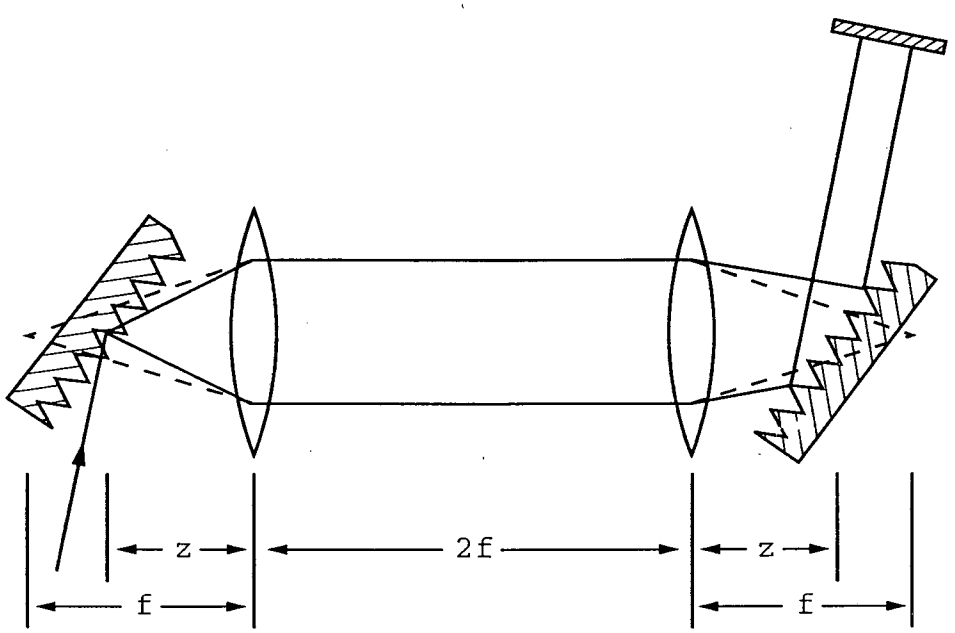


**Figure 4.3** Telescopic grating stretcher (not to scale)

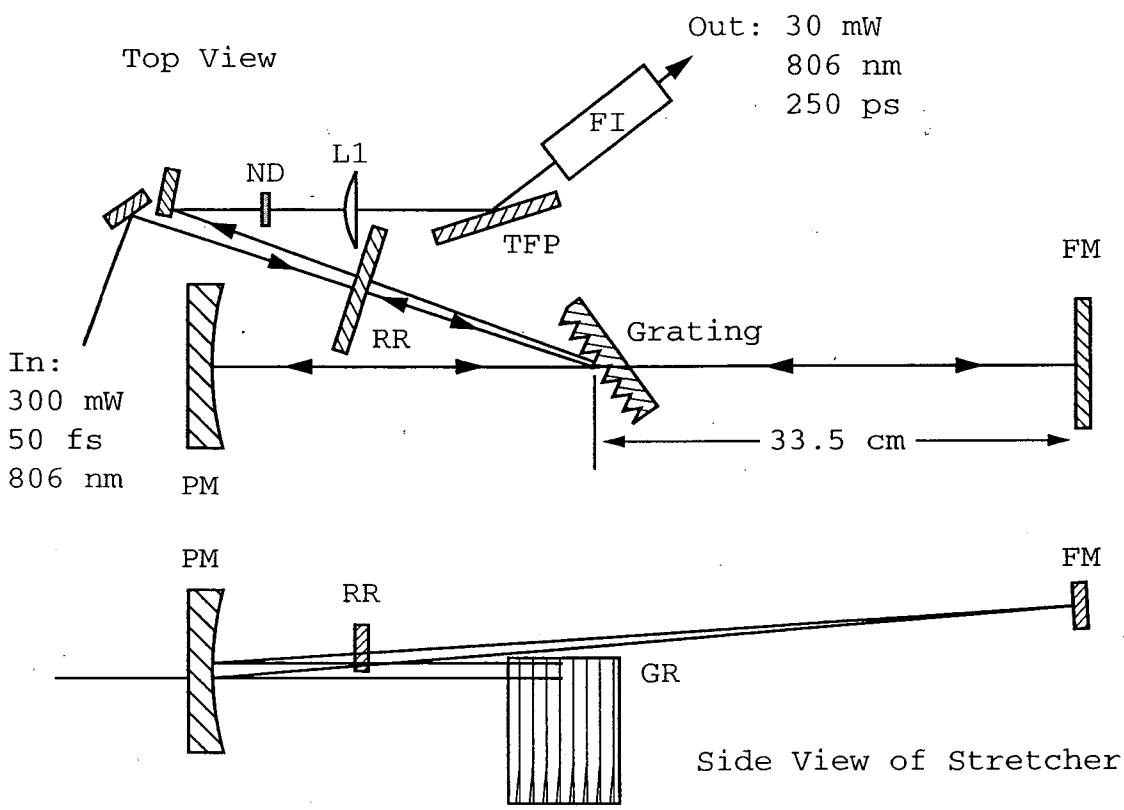


**Figure 4.4** Grating pulse stretcher (not to scale)

| Optic | Description |
|---|---|
| Grating | Gold-coated holographic grating, 1200 g/mm, 110x110 mm ruled surface, $\Theta_i$ = 39.99° |
| PM | Parabolic Mirror, gold-coated, 4.25" diameter, 25.5" f.l. |
| FM | Folding Mirror: Protected silver |
| RR | Retro-Reflector: Protected silver mirror |
| ND | 0.3 Neutral Density Filter |
| L1 | Uncoated Plano-convex lens, 2 m f.l. |
| TFP | Thin Film Polarizer, $T_p$ biased at 800 nm |
| FI | Faraday Isolator |

**Table 4.3** Optics legend for the grating pulse stretcher

fewer optics, thus reducing cost, and furthermore simplifies alignment, ensuring that the input angle to the grating is identical for each pass onto the grating surface. This latter point is important for it ensures that the pulses are not spatially chirped across the face of the pulse[103]. The 1200g/mm, gold-coated holographic grating (Spectrogon) is optimized for Littrow angle (28.6°) operation. Because of the folded geometry of the stretcher design, the input angle to the stretcher is 39.9°, and the stretcher throughput is only about 10%. This is more than enough power, however, to seed the regenerative amplifier. The parameter z for our stretcher is adjusted to 33.5 cm, and the resultant pulses are stretched to 250 ps as measured by a fast photodiode (Amtel) and storage oscilliscope (Tektronics). The full alignment procedure for the stretcher is given in Lukas Hunziker's thesis, and will not repeated in this section[96]. Daily alignment for the stretcher only takes a couple of minutes. First, the vertical alignment of the beam entering the stretcher is checked against an iris that is on the optical table. The horizontal alignment is checked by rotating the grating, making sure that the beam does not walk-off the grating center

position. The grating is then rotated back minimizing the amount of clipping of the beam by the parabolic mirror. Complete realignment of the stretcher, as described in Hunziker's thesis takes 1-2 hours.

The compressor is shown in figure 4.5, with accompaning table 4.4. Similar to the grating stretcher, it uses a pair of mirrors (JML) as a retro-reflector, RR, and a folding mirror ,FM, (JML) in order to fold the design, thus reducing cost and again, ensuring that the grating surfaces are anti-parallel. Unlike the Hunziker design, the compressor in our laser uses a separate grating (Richardson 1200g/mm, gold-coated). This makes it easier to fine-tune the input angle into the compressor. The amount of dispersion introduced by the grating compressor is determined by both the distance between the the RR and the grating surface and the input angle[5]. This distance is controlled by moving the RR, which is mounted on a translation stage (Edmund Scientific), and the input angle is controlled by rotation of the grating (Newport rotation stage).

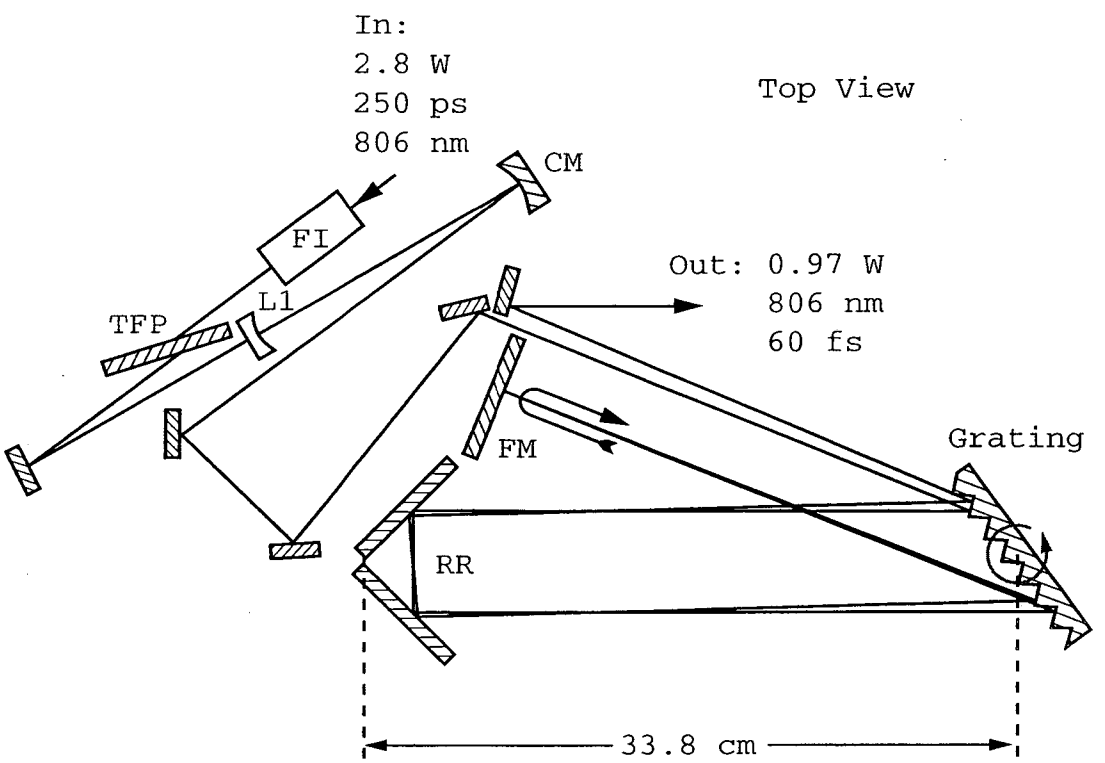


**Figure 4.5** Grating pulse compressor (not to scale)

| Optic | Description |
|---|---|
| L1 | -10 cm f.l. plano-concave lens AR coated at 800 nm |
| CM | High power concave curved mirror 25 cm f.l., >99% reflectivity at 800 nm |
| Grating | Gold-coated blazed grating, 1200 g/mm, 110x110 mm ruled surface, $\Theta_i$ = 40.73° |
| RR | Retro-Reflector: Protected silver mirrors |
| FM | Folding Mirror: Protected silver mirror |

**Table 4.4** Optics legend for the grating pulse compressor

### 4.3.1 Alignment and Optimization of the Compressor

Because of the slight modifications made in the compressor design, a short alignment procedure will be given below.

1. The grating is placed into its mount and is then secured to the rotation stage. It is very important that the grating is properly oriented within the mount with respect to the laser pulses. First, the reflections off of the grating surface must not deviate the beam in the vertical dimension. Second, the grooves of the grating must run perpendicular to the polarization of the laser pulses. This is checked by ensuring that all orders of diffraction from the grating surface lie in the same horizontal plane. Any misalignment with respect to this face-normal rotation will cause spatial chirp in the output pulse.

2. The retro-reflector is carefully aligned using a He:Ne laser. Here it is also critical that the beam is not steered in the vertical direction.

3. The grating is placed on the table and the laser beam is steered into the grating so that it is incident upon the grating surface 1.25 cm from the grating's edge,

and such that the input angle into the grating surface is 40.73°.

4. The retro-reflector is placed on the table so that it reflects the dispersed pulse back onto the grating. The dispersed pulse should now hit the opposite end of grating surface with respect to the input laser beam.

5. The beam then reflects off the grating surface, and should be parallel to the input beam but offset from it in the horizontal plane as shown in figure 4.5. The folding mirror is placed to reflect the dispersed pulse back onto itself, but offset slightly in the horizontal plane. This allows the beam to be picked off by a mirror external to the compressor.

6. With fully amplified pulses entering the compressor, the pulses exiting the compressor are focused with a microscope objective (Melles Griot), and the compressor angle and retro-reflector distance are tuned until a spark can be seen. The intensity of the spark is optimized.

### 4.3.2 Theoretical Considerations for Stretcher/Compressor Performance

Using equations 4.5 and 4.6 along with known values for the dispersion of the optical components system, it

is possible to calculate the overall dispersion in the laser system. Once this is known, the stretcher and compressor geometry can be optimized in attempts to minimize the dispersion across the spectrum of the laser pulses[101, 104-106]. Hunziker carried out such dispersion calculations for this laser system, and his calculated parameters were used to determine the placement of optics in the stretcher/compressor pair[96]. As mentioned above, it is the overall dispersion in the laser system that leads to pulse broadening. These calculations, however, are not exact, and further refinement of the compressor is usually necessary. A simple procedure for the optimization of the compressor following the rough alignment as described in section 4.3.1, is as follows.

1. The microscope objective of step 6 above is removed, and longer focal length lens of 10 cm is put in its place.

2. The focused, compressed pulses are sent into a short (0.5 mm) BBO crystal (CASIX), and the crystal is tuned to maximize the doubled light at 403 nm. The residual 806 nm light is filtered out with a glass filter (Corning), and the 403 nm light is sent to a

photomultiplier tube. The resulting signal is sent to a digital oscilloscope (Tektronix).

3. While monitoring the photomultiplier tube signal on the scope, the retro-reflector distance and the grating input angle are tuned. These two optical components are adjusted to maximize the 403 nm signal.

Daily compressor alignment is also quite easy. Irises on the laser table guide the beam into the compressor. Alignment through these optics takes 1-5 minutes. Complete realignment as outlined above, however, is slightly more tedious but still only takes 1-2 hours. Typically, 1.8 W of light are sent into the compressor, and 0.95-1 W are recovered.

### 4.4 Nd:YAG Pump Laser

The laser used to pump the Ti:sapphire regenerative amplifier is an intra-cavity doubled Nd:YAG laser. This laser consists of a basic Nd:YAG laser with a z-cavity configuration (figure 4.6). Mirrors M2 and M3 reduce the size of cavity mode in the LBO crystal (Skytek) to maximize the doubling efficiency of the laser. In solid-state laser materials such as Nd:YAG, however, a thermal gradient exists across the diameter of the laser rod due the cooling water surrounding the laser crystal that

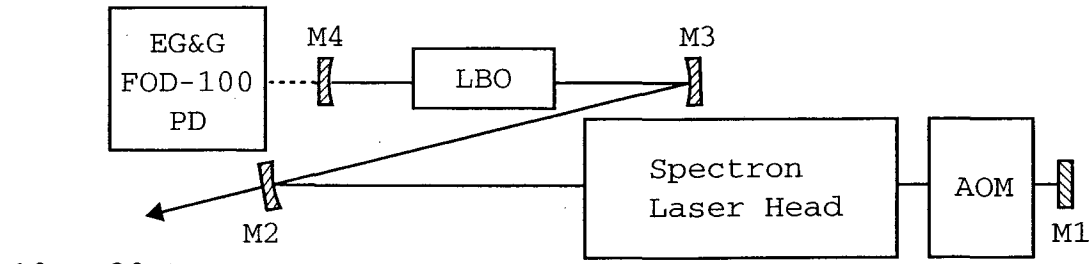


10 - 20 W
532 nm
200 ns
2 kHz
to Regenerative Amplifier

**Figure 4.6** Intra-cavity doubled Nd:YAG laser (not to scale)

| Optic | Description |
|---|---|
| M1 | high power, high reflector at 1064 nm, flat |
| AOM | Acousto-optic modulator |
| Spectron Laser Head | Nd:YAG rod and pumping chamber with single flashlamp |
| M2 | high power, high reflector at 1064 nm, high transmit at 532 nm, 50 cm r.c. |
| M3 | high power, high reflector at 532 and 1064 nm, 20 cm r.c. |
| LBO | LBO doubling crystal 3x3x7 mm |
| M4 | high power, high reflector at 532 and 1064 nm, 10 cm r.c. |

**Table 4.5** Optics legend for the intra-cavity doubled Nd:YAG laser

| Optical Path Length | Distance Between Optics (cm) |
|---|---|
| M1-M2 | 68.5 |
| Nd:YAG-M2 | 35.4 |
| M2-M3 | 35.1 |
| M3-M4 | 19.8 |
| M3-LBO | 9.8 |

**Table 4.6** Optical path lengths for the intra-cavity doubled Nd:YAG laser

leads to thermal lensing inside the laser rod[92]. This lensing property creates mode instabilities inside the doubling crystal which cause the power output to fluctuate, which can lead to optical damage to the LBO crystal. This lensing problem is circumvented by careful choice of mirrors M2 and M3 such that the surface of the laser rod is imaged into the LBO crystal.

This imaging of the Nd:YAG laser rod surface into the crystal for intra-cavity frequency doubling was patented by Kuizenga in 1991[107]. In our laser, M2 and M3 image the rod surface into the LBO crystal according to the telescope equation:

$$md_1 + d_2 / m = f_1 + f_2, \qquad 4.7$$

where $f_1$ and $f_2$ are the focal lengths of the focusing mirrors M2 and M3, respectively, $m = f_2 / f_1$, $d_1$ is the distance between M2 and the laser rod surface, and $d_2$ is the distance between M3 and the center of the LBO crystal. This imaging, known as relay imaging, exactly reproduces the image from the laser rod surface into the LBO crystal in phase and amplitude, with the image reduced by a factor of m[108].

The remainder of the laser design is only slightly modified from that of Hunziker[96]. The laser rod is highly efficient Nd:YAG rod enclosed in a water-cooled pumping chamber (Spectron CW-60 series). The mirrors, described in table 4.5 were purchased from CVI (M1 and M2) and Alpine Research Optics (M3 and M4). Mirrors M3 and M4 are highly reflective at both 1064 and 532 nm, and direct the intra-cavity doubled light out through M2, which is AR coated at 532 nm. The laser is Q-switched with an acousto-optic modulator(AOM) (NEOS N-33027-50-5-I) which is driven by a crystal technologies driver (Model AOQ).

The Nd:YAG laser is typically run at a 2 kHz repetition rate giving 6.9 watts of 532 nm light. Typical pulse widths are 190-200 ns with peak-to-peak intensity fluctuations of 1-2% as measured by a fast photodiode (EG&G FOD-100, -90V Bias; < 1ns rise-time) and a digital oscilloscope (Tektronix). At high pumping intensities, the AOM is unable to hold off lasing from the very efficient laser cavity. At 2 kHz the maximum 532 nm output is 20.4 W with the pulse width shortened to 110 ns. At 1 kHz, the maximum 532 nm output is reduced to 11.1 W in 110 ns.

As mentioned above, intra-cavity doubling is accomplished by a type II LBO doubling crystal (Skytek Corp.). The crystal is cut for phase matching at 35° C ($\theta$=21.7°, $\phi$=90°) and is mounted in a temperature controlled housing shown in figure 4.7. The cylindrical mount holds the LBO crystal, a small 100W (Omega CIR-1012/120) heater and a Copper-Constantan (T-type) thermocouple (Omega TMSS-062G). The heater is controlled by a programmable temperature module (OMEGA CN9000A). To minimize dust and air current problems, the entire pump laser is enclosed in a box. The ambient temperature inside the box was found to lie between 28° and 30° C, and the temperature controller was unable to accurately control the LBO temperature so close to ambient conditions. For this reason, the larger aluminum optical mount is cooled at 20° C. With this new configuration, the temperature of the LBO crystal is maintained at 35.0 ± 0.1° C. The fluctuation of 0.1° C occurs over minutes and causes a long-term power drift of ~2% that is directly correlated to the temperature drift.

### 4.4.1 Daily Operation

The Nd:YAG requires little day-to-day alignment. Typically, the cabinet which powers the single arc lamp

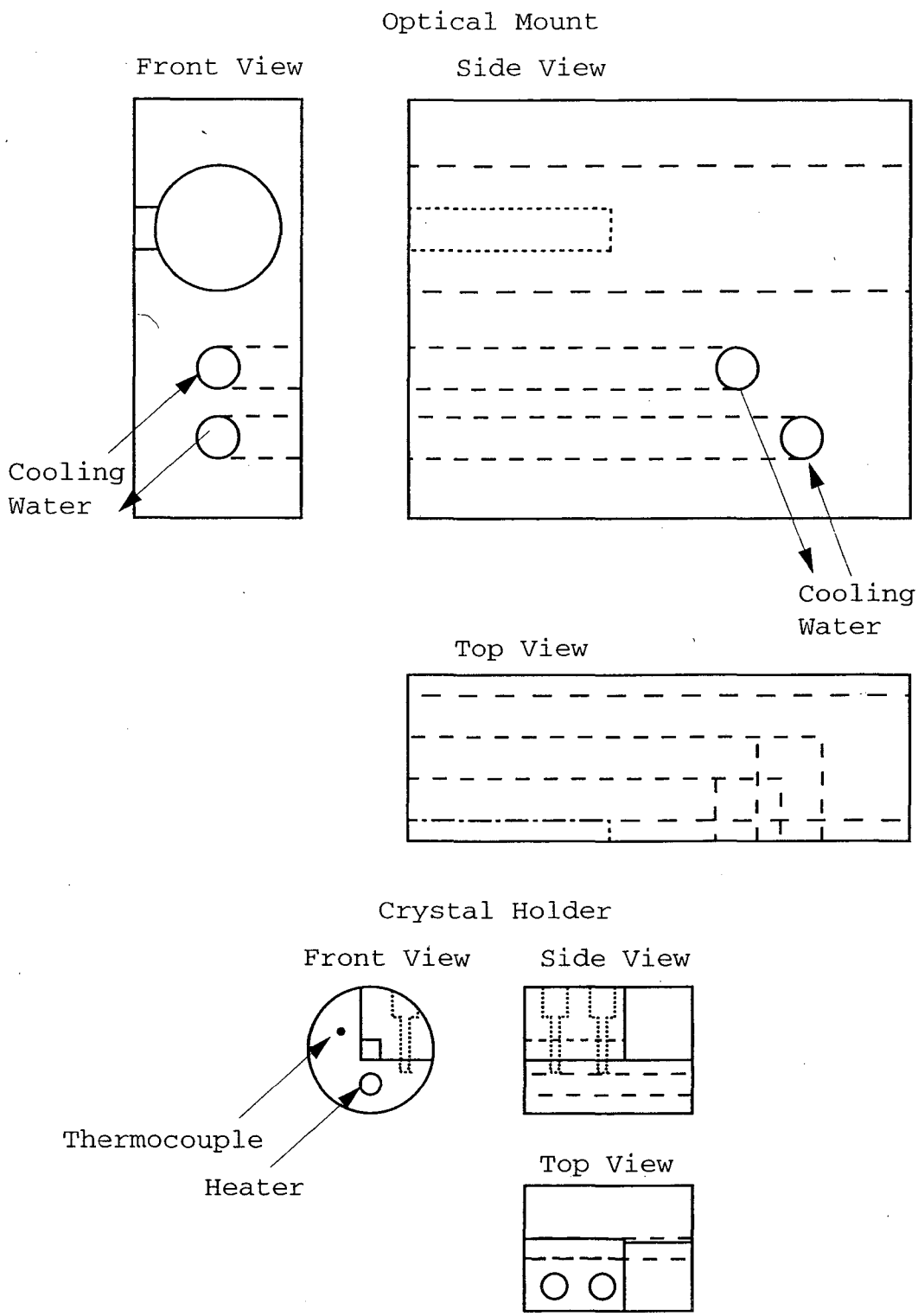


**Figure 4.7** LBO crystal housing (not to scale)

in the Nd:YAG pumping chamber is turned on and the Q-switched laser is warmed up at operational power for 30 minutes. Once warmed up, the crystal mount, attached to a 2-axis tilt stage (New Focus) is adjusted to maximize 532 nm laser output. The end mirror M4 is then adjusted, also to maximize power. This procedure is iterated until an absolute maximum is reached. It may be necessary to adjust the AOM (also attached to a New Focus 2-axis tilt stage) to maximize power or to optimize hold-off. The 1064 nm high reflector, M1, should only be adjusted if the laser cavity mode spots are not centered on the mirrors M2, M3, and M4. Adjustment of this mirror has a large effect on the pointing direction of the output 532 nm beam, and thus may affect the alignment into the regenerative amplifier. In any case, however, daily alignment usually takes less than five minutes after the 30 minute warm-up time.

### 4.4.2 Cavity Alignment

Whenever optics within the cavity are moved or replaced, complete cavity realignment may be required. The following is a general procedure for the realignment of the Nd:YAG laser.

1. The cylindrical LBO crystal holder is slid out from the larger mount, which holds it in place. With the doubling crystal out of the cavity, the remaining cavity optics are placed on the table as shown in figure 4.6. The distances between the optics are given in table 4.6. A He:Ne is used to check the proper alignment of the optics, and that the Nd:YAG rod face is perpendicular to laser cavity in the horizontal and vertical directions.

2. The flat high reflector, M1, is replaced with a 10% output coupler at 1064 nm (CVI), and a high-power power meter is placed after it.

3. The pumping arc lamp is turned on, and using an infrared viewer (FJW Optical Systems) the fluorescence from the Nd:YAG rod is centered on all the mirrors. Fluorescence overlap from one end of the cavity to the other is checked at M1 or M4. The arc lamp power is turned up and the end-mirrors M1 and M4 are adjusted until lasing occurs.

4. Once the cavity is lasing, the laser beam is walked so that the beam is at the center of all the optics. This is done slowly such that the laser remains lasing at all times. First M1 and M4 are adjusted to center the beam on M2. Then M2 and M4 are adjusted in order to

center the beam on M3. Finally, M3 and M4 are adjusted to center the beam on M4. The cavity power is then maximized by walking the beam with M1 and M4. The whole procedure is iterated until the beam is centered on each of the optics. If the beam is not centered on M2 when the laser is at maximum power, then M2 should be moved, and the procedure carried out until the cavity beam is centered on this mirror.

5. The face of the AOM should be nearly perpendicular to the cavity beam in both the horizontal and vertical planes. When adjusting the tilt of the AOM, the angle with respect to the cavity beam can be observed by looking at the surface reflection off the AOM at or near M4. If it is adjusted very far, the cavity alignment in step 4 should be checked.

6. The laser is then Q-switched at 1064 nm. The Q-switched output can be monitored with the power meter and a fast-photodiode. Because of thermal lensing, the cavity alignment might change, in which case, the alignment procedure in step 4 should be undertaken while Q-switched. At full power, the Nd:YAG laser with the 10% output coupler should be able to produce 77-78 W of 1064 nm at 3.0 kHz.

7. The laser arc lamp and the Q-switch are turned off, and the 10% output coupler is replaced with the 1064 nm high reflector. The lamp is turned back on and slowly turned up until the laser begins to lase. The 532 nm output coupler, M2, is only about ~99% reflective at 1064 nm, and thus will act like an ~1% output coupler. Once lasing, M1 is adjusted to maximize power through M2.

8. The arc lamp is again turned off, and the LBO crystal housing is slid back into its mount. The distance from the crystal surface to M3 is checked. The arc lamp is turned on, but is kept at low power, below lasing threshold. The LBO crystal mount is then adjusted such that the fluorescence from the Nd:YAG is centered on the crystal. The LBO heater and thermocouple are attached to the temperature controller, and allowed to reach a stable 35° C.

9. The arc lamp power is slowly turned up until lasing threshold is reached. For CW operation, this is usually around 10.5 A of current to the arc lamps. The LBO crystal position is checked again to make sure that the cavity mode is centered inside the crystal and that the LBO crystal surface is nearly perpendicular to the cavity mode.

10. At this point, the laser is Q-switched again. The crystal angle and mirror M4 are adjusted to maximize the 532 nm light output. If the beams are not centered on the mirrors M2, M3, and M4, then the procedure in step 4 can be undertaken again with the LBO crystal in the cavity. Care must be taken, however, to ensure that the cavity beam does not clip the side of the LBO mount while walking the beam.

11 Power is maximized by iteratively adjusting M4, the LBO crystal angle and the Q-switch angle.

12. The polarization of the 532 nm light is controlled by the rotation of the cylindrical LBO holder within its mount. The output polarization can be checked with a linear polarizer and the crystal mount can be rotated to achieve the desired rotation. In order to pump the regenerative amplifier, a polarization in the plane of the optical table is desired (p-plane).

Complete alignment as described above usually takes a couple of days up to a week to complete. The most difficult part is the accurate placement of the optical components. Once the placement of the optical components has been established, total realignment usually takes no more than one day.

### 4.4.3 Pumping Chamber Modifications

The cavity beam is enclosed by tubes between M1 to M2 in order to protect the expensive Nd:YAG rod and AOM faces from stray dust particles. These beam tubes were installed after the laser rod surface was burnt by a piece of dust. The stainless steel chamber, which houses the Nd:YAG rod, was modified to allow the rod to be easily removed for repolishing and recoating. The newly designed laser head is shown in figure 4.8. The tapered Teflon or Delron o-rings are made by the machine shop. The taper in these o-rings allows the soft material to compress, thus forming a watertight seal between the YAG rod and the pumping chamber head. The laser head is assembled by slipping one o-ring around the Nd:YAG rod, then sliding the rod without a ring through the opening in the laser head until it comes through on the side. The second o-ring is placed on this end of the YAG rod and very carefully, the o-rings are worked by hand into the grooves machined into the face of the pumping chamber. The retaining rings are then placed over the laser rod and are very slowly screwed into the head assembly. These retaining rings create the final seal,

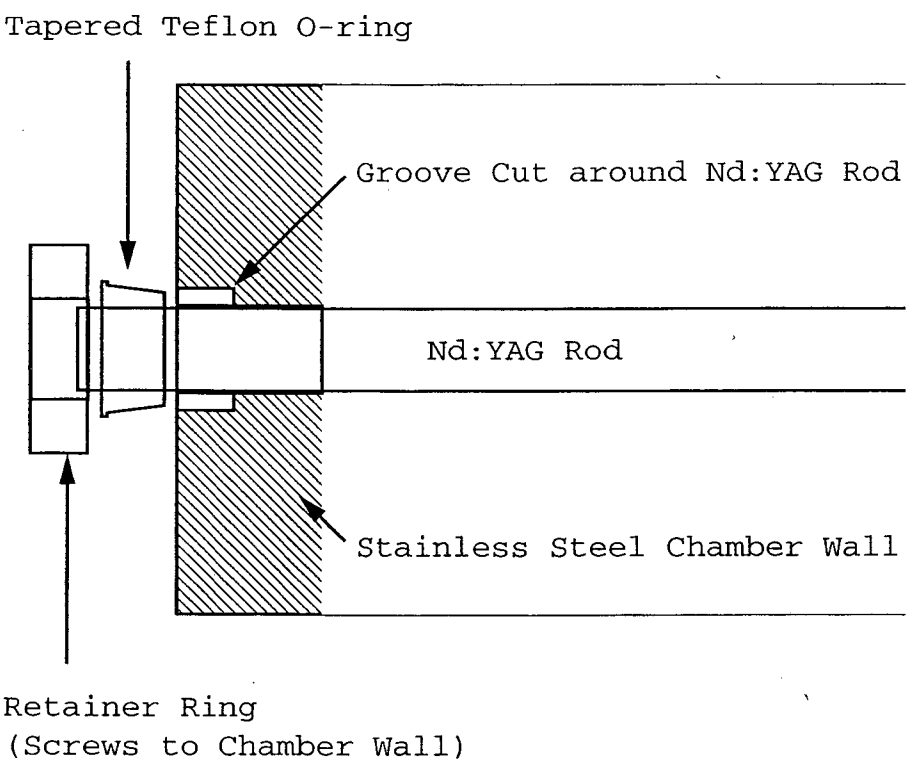


**Figure 4.8** Nd:YAG laser housing modifications (not to scale)

and therefore must be tightened slowly on alternate sides to ensure a proper seal.

### 4.5 Ti:Sapphire Regenerative Amplifier

As mentioned above, regenerative CPA of ultrafast laser pulses was first demonstrated by Mourou in 1991[93]. Since then, other CPA schemes have been built, including multi-pass amplifiers at different repetition rates, cw-pumped regenerative amplifiers, and regenerative amplifiers with different internal dispersion-compensation[5, 105, 106, 109-112]. Our Ti:sapphire regenerative amplifier is based on the design from Hunziker, which in turn was based on a design from the Wilson group at the University of California, San Diego[96]. The laser cavity, shown in figure 4.9, is also in a z-configuration. A description of the optical components appears in table 4.7. Each of the cavity mirrors has a highly reflective coating for wavelengths between 760 and 820 nm. Mirrors M1 (CVI) and M2 (Alpine Research Optics) have an anti-reflective coating for 532 nm. The Ti:sapphire crystal (Atramet) is cut at the Brewster angle ($\Theta_{Brewster}$), has a figure of merit > 300, and is doped with 0.1% Titanium by weight. The crystal sits in a water-cooled mount made of copper by Professor Yong

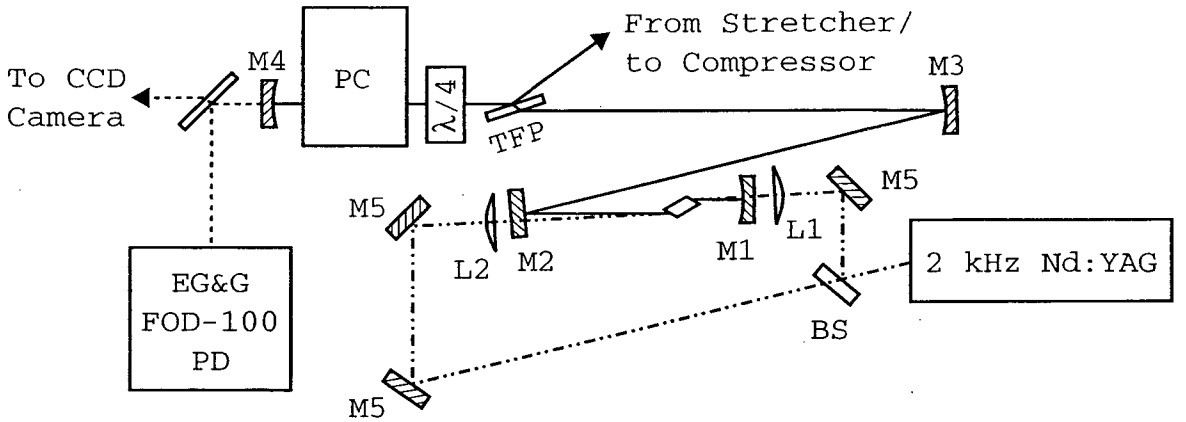


**Figure 4.9** Ti:sapphire regenerative amplifier (not to scale)

| Optic | Description |
|---|---|
| M1 | high power, high reflector centered at 800 nm, 100 cm r.c., AR Coated 532 nm |
| crystal | Ti:sapphire crystal; 25x2x3 mm |
| M2 | high power, high reflector centered at 800 nm, flat, 532 nm AR coated |
| M3 | high power, high reflector centered at 800 nm, 100 cm r.c. |
| M4 | high power, high reflector centered at 800 nm, 400 cm r.c. |
| λ/4 | 1/4 wave plate, AR coated at 800 nm |
| PC | Lasermetrics Pockels Cell |
| TFP | Thin film polarizer, centered at 800 nm |
| L1 | 10 cm fl plano-convex lens, AR coated 532 nm |
| L2 | 10 cm fl plano-convex lens; AR coated 532 nm |
| M5 | 532 nm flat high power, high reflectors |
| BS | high power 56/44 (%R/%T) beam splitter |

**Table 4.7** Optics legend for the Ti:sapphire amplifier

| Optical Path Length | Distance Between Optics (cm) |
|---|---|
| M1-crystal | 6.7 |
| crystal-M2 | 9.4 |
| M2-M3 | 37.1 |
| M3-M4 | 65.0 |
| L1-crystal | 12.7 |
| L2-crystal | 11.5 |

**Table 4.8** Optical path lengths for the Ti:sapphire regnerative amplifier

Chen. A thin layer (0.1 mm Aldrich) of Indium is compressed between the copper mount and the crystal to ensure good thermal contact between the crystal and its housing.

The optics used to switch pulses in and out of the cavity for amplification are the thin film polarizer, Pockel's cell, and $\lambda/4$ plate. The thin film polarizer (TFP) (Alpine Research Optics), used to reflect pulses into and out of the cavity, has coatings optimized to transmit p-polarized light between wavelengths of 740 and 860 nm. The $\lambda/4$ plate (Lasermetrics) rotates the polarization of the cavity pulse, and the Pockel's cell (Lasermetrics) controls the switching of pulses in and out of the cavity. Both of these optics have an anti-reflective coating for wavelengths between 740 and 860 nm. When the Pockel's cell is off, each pulse from the oscillator is reflected off the TFP, is rotated by the $\lambda/4$ plate, reflects off the mirror, M4 (CVI), and passes through the $\lambda/4$ plate again. At this point the polarization has been rotated 90° and the pulse passes through the TFP, reflects off M3, M2, and M1, going through the crystal twice before coming back through the TFP. The pulse then passes through the $\lambda/4$ plate twice

more, rotating its polarization by another 90° before being reflected out of the cavity by the TFP. Thus, without voltage supplied to the Pockel's cell, each pulse from the stretcher goes through one complete cavity round trip.

To switch pulses into and out of the amplifier cavity, a static voltage is applied to the Pockel's cell after the pulse has passed through the TFP once. The static voltage applied to this crystal creates a $\lambda/4$ rotation within the Pockel's cell, such that when the pulse returns after having passed through cavity, its net rotation is 0° and is thus trapped in the cavity as long as the voltage is applied to the Pockel's cell. Furthermore, because there is no net rotation present, any new pulses from the stretcher which are reflected into the cavity while the Pockel's cell voltage is on are immediately reflected out.

The regenerative amplifier is pumped by the Nd:YAG laser described in section 4.4. The output from the pump laser is split by a 56/44 beamsplitter (CVI), and is directed into the Ti:sapphire amplifier crystal via high-power dielectric mirrors, M5 (Alpine Research Optics) and lenses L1 and L2 (Newport). Like the oscillator, and

Nd:YAG, the Ti:Sapphire amplifier is enclosed in a box which sits beneath a clean-air filter (Envirco, MAC 10, 2x4 ft. HEPA filter).

### 4.5.1 Cavity Alignment

The alignment procedure for the Ti:sapphire cavity is described below and is mainly based on the procedure found Lukas Hunziker's thesis[96]. The distances between the optical components can be found in table 4.8. The procedure below takes about two three days to complete and about one week to completely optimize the placement of all the optics. Once this is done, however, alignment involving the replacement of a single optic, due to laser burns or scratches, usually takes less than a day.

1. The beamsplitter and one M5 mirror for the short pump arm (56% reflected) is placed on the table. With the Nd:YAG power turned down as low as it will go, the pump beam is set up level to the table. The lens, L1, is attached to a translation stage, and is placed such that it does not alter the direction of the beam horizontally or vertically for the length of its travel.

2. The mirror M1 is placed such that it does not deviate the beam. The Ti:sapphire crystal is then placed on the table. The reflected 532 nm light is measured and

minimized to get the crystal near Brewster's angle and the surface reflection is checked to make sure that it does not deviate the pump beam in the vertical direction. The remaining mirrors, M2, M3 (Alpine Research Optics), and M4 as well as the TFP and Pockel's cell are placed on the table. For initial alignment, the mirror M4 is replaced with a 2 m f.l., 10% output coupler (CVI).

3. The power in the pump beam is increased to 7 W. With the IR viewer, the fluorescence spots from the Ti:sapphire are aligned on the center of the cavity optics. The cavity end mirrors M1 and M4 are then walked until lasing occurs.

4. The angle of incidence of the cavity mode to the TFP is adjusted until it is 72°.

5. The cavity mode is then walked with mirrors M1 and M4 until cavity power is a maximum. Care must be taken to ensure that the cavity beam does not clip the edges of the Pockel's cell. This could cause damage to the electrical element that supplies voltage across the Pockel's cell crystal.

6. The cavity mode is centered on the mirror M3 by adjusting M2 and M4, and then on M4 by adjusting M3 and

M4. The beam should remain level to the table at the height of the pump beam and the crystal surface.

7. The face of the crystal is checked to make sure that it is perpendicular in the vertical sense with respect to the cavity beam. This is done by looking at the weak reflections of the cavity beams off the Ti:sapphire crystal surfaces with the IR viewer. The crystal mount should be shimmed so that the height of the reflections from each of the crystal faces is the same and does not deviate from the vertical plane of the cavity beam.

8. Steps 4 through 7 are iterated until an absolute maximum is reached. The surface reflections off the face of the laser crystal of the pump beam and the cavity beam should be overlapped vertically, and nearly overlapped horizontally. There should be a slight horizontal offset due to differences in the index of refraction in Ti:sapphire between 532 nm and the red cavity mode[113].

9. The M4 output coupler is replaced with the highly reflective mirror. The amplifier cavity is pumped again, and the power coupled out through the TFP is maximized following the procedures in steps 4 through 7.

10. A CCD camera is set up to view the leakage light through M4. Set the camera to look at the cavity beam

approximately 2 m away from M4, and mark the position of the beam on the on the monitor, or in the plane upon which it is viewed (a simple cross-hair target will suffice).

11. The $\lambda/4$ plate is inserted into the cavity. Its angle is adjusted such that its surface does not deviate the beam, and then it is rotated so that the regenerative amplifier cavity stops lasing.

12. The pump laser is blocked, and with two mirrors external to the cavity, a seed pulse from the stretcher is directed into the cavity via the TFP such that it exactly overlaps the amplifier cavity beam. The seed beam is collinear to the cavity when two spots are observed to land directly upon the cross-hair target. One spot is due to the first reflection off of M4 and the other is due to the first round trip through the cavity.

13. Proper $\lambda/4$ rotation by the Pockel's cell is determined using an Isogyre pattern. First the $\lambda/4$ wave plate is removed. A linear polarizer is placed before the TFP and transmission through the polarizer is minimized. The polarizer is then moved behind the aperture of the Pockel's cell opposite the TFP. This exit aperture is then covered with a piece of Scotch tape or a piece of

lens tissue. The combination of tape and polarizer should produce an Isogyre pattern which looks like a cross that is surrounded by a halo. The pitch and azimuth controls on the Pockel's cell are adjusted to make this Isogyre pattern as well defined as possible. A cross-hair target can then be aligned to this cross. The proper $\lambda/4$ rotation can then be found by applying a voltage to the Pockel's cell and turning up the voltage until the Isogyre pattern is rotated by 45°. Once this is done, the polarizer and tape are removed and the seed beam is blocked.

14. The $\lambda/4$ plate is re-inserted and the pump laser is unblocked. The $\lambda/4$ plate is adjusted to inhibit lasing. The Ti:sapphire laser can now be Q-switched. By applying a static voltage pulse following the pump laser pulse arrival, build-up inside the amplifier cavity occurs. This light can be dumped by turning-off the Q-switch voltage. With 4.5 W of 532 nm pump light at 2 kHz, a Q-switch gate width of 180 ns, and $\lambda/4$ Pockel's cell voltage of 3.5 kV, 1.0 W light at 800 nm is generated.

15. The weaker pump arm is now aligned to the cavity. With the pump laser turned down, two high-power mirrors M5 are placed and the beam is steered to the cavity beam

at mirror M2, the crystal surface, and at some distance away from the Ti:sapphire crystal by looking at the reflection off the crystal face. Lens, L2, is placed in the cavity so that it does not steer the pump beam. Fine adjustments are made to the pump beam position in order to overlap it with the strong pump beam, and the cavity mode. With the weak beam now aligned and the strong beam blocked, the Pockel's cell is turned on and the voltage gate is increased until the lasing occurs. Once lasing is achieved, the pump beam can be walked with the M5 mirrors to maximize the power. With 3.6 W of 532 nm pump light at 2 kHz, a Q-switch gate width of 300 ns, and $\lambda/4$ Pockel's cell voltage of 3.5 kV, 540 mW of light at 800 nm are generated.

16. Both arms are now unblocked. With a 3.8 W in the weak pump arm, at 2 kHz, a Q-switch gate width of 80 ns, and $\lambda/4$ Pockel's cell voltage of 3.5 kV, 2.2 W of red light are generated. When the laser is pumped with both arms, it may be necessary to slightly adjust the cavity alignment due to thermal lensing in the Ti:sapphire crystal. Once power is maximized with the cavity mirrors, the pump beams should be tweaked slightly to

ensure optimal overlap of the pump beams with the cavity beam.

Daily alignment of the amplifier usually begins by optimizing the unseeded regen cavity. This mainly involves the adjustment of mirror M4 along with the electronic timing, as described below. Once the unseeded cavity mode is optimized, the stretched pulses from the oscillator are aligned into the cavity according to the procedure in step 12, above. Once the amplifier is seeded, the alignment into the compressor is adjusted, and the final amplified power is measured. This entire process requires less than 10 minutes. This is a significant improvement over the previous dye laser amplifier mentioned in the introduction, which normally took an hour or more to align each time the laser was started.

### 4.5.2 Electronic Timing

A simplified block diagram of the control electronics for the laser system is shown in figure 4.10, and the timing information regarding these electronics is shown in figure 4.11. There is a 2 kHz square wave generator whose signal is sent to the AOM Q-switch of the Nd:YAG laser. A 532 nm Q-switched laser pulse is

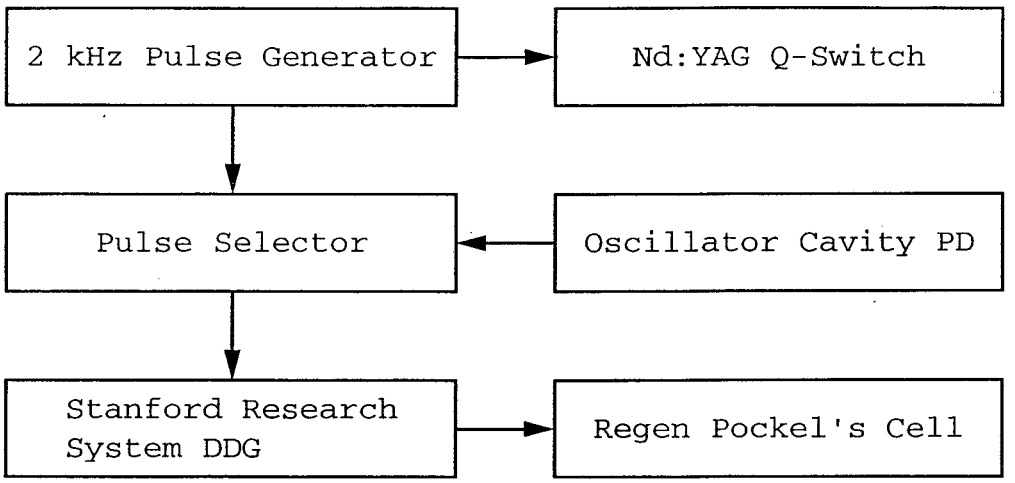


**Figure 4.10** Electronic connections (BNC)

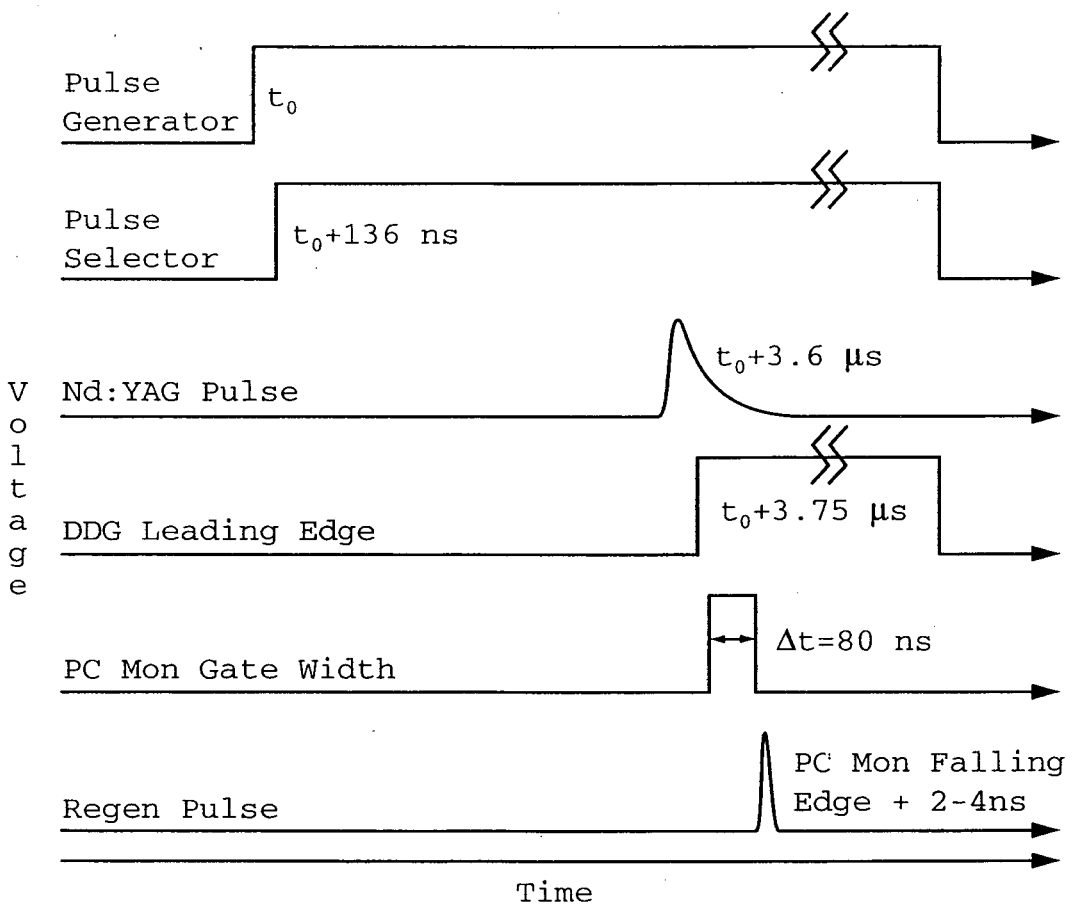


**Figure 4.11** Pulse timing diagram

generated approximately 3-3.5 μs after this initial trigger. The YAG pulse that is generated has a timing jitter of ±20 ns. This pulse train determines the repetition rate of the pump laser, and hence the amplifier. The amplifier, however, must not only be synched to the pump laser, but to the oscillator as well. This is accomplished with the module labeled pulse selector in the figure. The pulse selector sends a positive TTL signal ~136 ns after the first oscillator pulse that follows the trigger sent to the Nd:YAG laser. This selector-signal is sent into a Stanford Research Systems digital delay generator (DDG, SRS DG535). The DDG generates pulses with a variable time delay in respect to the aforementioned input pulse which are then sent to the Pockel's cell high voltage driver in order to initiate a $\lambda/4$ voltage gate across the Pockel's cell, as mentioned in the previous section. The delay is set such that Pockel's cell gate voltage is along the trailing edge of Nd:YAG pulse, offset by 100-200 ns from its peak. This avoids problems due to the timing jitter of the pump pulse. The width of the high-voltage gate, and hence the build-up time of the amplifier, is controlled by the Pockel's cell high-voltage supply.

## 4.6 Laser Performance

The previous dye-amplified laser system that was described in chapter 2 and the introduction to this chapter typically took hours or even days and weeks to align each time the laser was started. One significant advantage to this new solid-state laser is its ease of use on a daily basis. As can be seen from the above sections, the laser can be turned on and optimized in approximately one hour, complete realignment can be accomplished in a couple of days, and wiping the table clean and starting over would take perhaps one or two months given the instructions contained in this chapter. Of course, this last number presumes that all the optics and mounts are available to the builder and that the builder has extensive experience with laser alignment and optimization. Nevertheless, the time saved in the daily operation of this laser should allow graduate students to focus more on experiments rather than troubleshooting an unstable laser system.

Typical operating parameters for each of the lasers is given in table 4.9. The Nd:YAG is typically run at less than 10 W average power. At this power, the Pockel's cell gate widths are 85 and 60 ns when the laser

| Laser | Power | Rep. Rate | Pulse Width | λ(nm) |
|---|---|---|---|---|
| Oscillator | 300 mW | 88.1 MHz | 50 fs | 806 |
| After Stretcher | <30 mW | 88.1 MHz | 250 ps | 806 |
| Nd:YAG | 8.6 W | 2 kHz | 200 ns | 532 |
| Regen (Unseeded) | 2.3 W | 2 kHz | 9-10 ns | 806 |
| Regen (Seeded) | 1.8 W | 2 kHz | 250 ps | 806 |
| After Compressor | 950 mW | 2 kHz | | 806 |

**Table 4.9** Laser output parameters

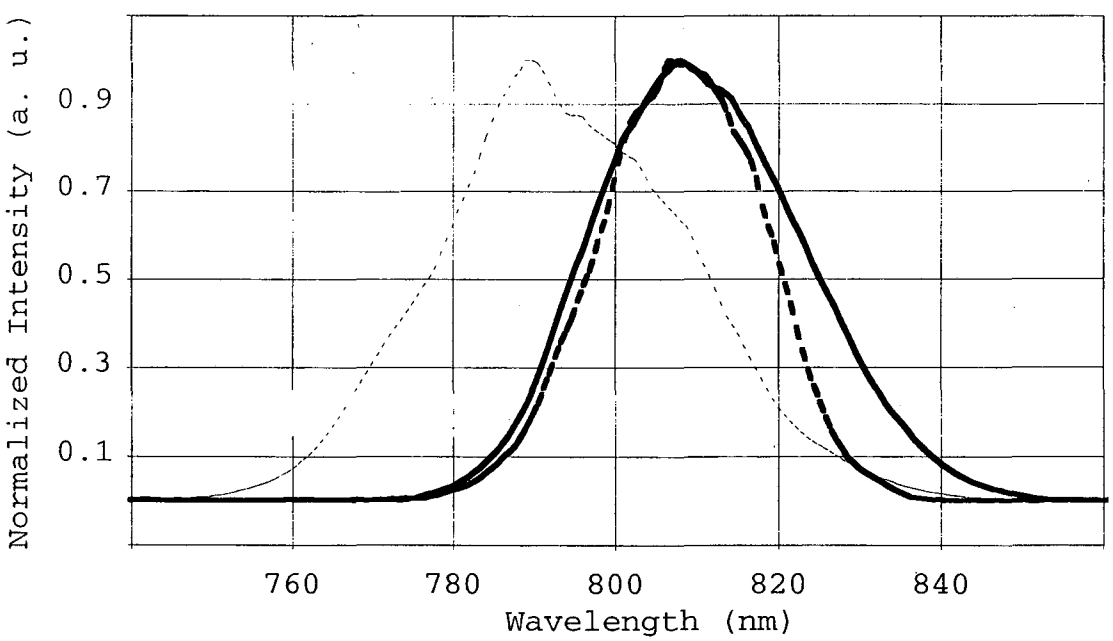


**Figure 4.12** Laser output spectra after: ——— oscillator, — — compressor, - - - - unseeded regen

is run unseeded and seeded by the oscillator, respectively. The round-trip cavity time for the regenerative amplifier is 8.8 ns, which means that each amplified pulse is trapped in the regenerative amplifier for 8 cavity round trips. Spectra of the mode-locked oscillator, the amplified and compressed amplifier, and the unseeded, Q-switched amplifier appear in figure 4.12. There are two interesting observations to make from the spectra. The first is that the spectrum of the compressed pulses is nearly identical to the oscillator pulses, and only slightly narrowed on the red end of the spectrum. This narrowing is due to clipping in the stretcher and the reflectivity of the optics in the regenerative amplifier, which dies off at 820 nm. The second feature to note is that the spectra for the Q-switched amplifier is shifted to the blue with a maximum intensity at 790 nm, the gain maximum of Ti:sapphire [114]. The theoretical transform limit for the compressed pulses, based on equation 4.2, is 40 fs.

## 4.7 Conclusions

Due to time-constraints, I unfortunately will not be able to use this laser system for what it was originally intended. The amplified output is currently being sent

to a commercial optical parametric amplifier (OPA) (Quantronix TOPAS) to generate signal and idler pulses of light in the near infrared. These two pulses are then mixed in a $AgGaS_2$ crystal, generating the difference frequency between signal and idler pulses, which lies in the mid-infrared. A portion of the amplified output is also sent into two more non-linear crystals in order to generate the third harmonic output (266 nm) of the fundamental beam (800 nm). In the near future, we will also have a linear 32-element mercury-cadmium-telluride (MCT) mid-infrared detector that is capable of operating at kilohertz repetition rates. With these components, numerous 266 nm pump-tunable mid-infrared probe experiments will be possible. The details of these post-amplifier frequency conversion devices as well as the experiments that will be carried out with them will be described in future theses from graduate students in the group.

# Appendix

# Computer Code for the Brownian Motion Ligand Rearrangement Simulation

## A1.1 Simulation Engine

The code for the Brownian motion simulation was written in the C programming language for use on the UNIX workstations in the laboratory. As mentioned in chapter 3, the coding algorithms are based on the text of Allen and Tildesley's book[80]. Slightly different coding was used to determine the rearrangement statistics for the different alcohols: methanol, ethanol, 1-propanol, and 2-propanol. These differences are described in section A1.2. The code for random walk through n-propanol appears below (please note that comments are written with the standard C-code convention and the C++ convention):

```
/*
 * n_propanol.vk2.c
 *
 *    Brownian Motion simulator for rearrangement of n_propanol at
 *    a transition metal center - Simon's model for non-random
      hopping is
 *    included in it.  You compile code for random hopping by sending
```

```
 *    the word RANDOM to the preprocessor.  In absence of the
      preprocessor,
 *    the non-random hopping is compiled.
 *    Can take into account coordination of carbon or hydrogen
      statistics
 *    by including (or not including) the preprocessor word CSTAT.
 *    Including the preprocessor CSTAT command uses carbon statistics
 *
 */
// 10/4/2001 removed potential offset
/*  6/6/2000 Altered to take into account non-random hops  */
/*  6/2/2000 Added Binary read/write  */
/*  6/1/2000 Trying to solve problem with symmetric potentials */
/*  This version seems to replicate older versions by Haw, plus the
 *  code is MUCH more compact, less redundant, and possibly faster!*/
/*  Haw's Notes:
 * 990723 - Done with velocity selection in Borders Cafe, Emeryville.
 *          Next, cooling time simulation/termination condition.
 * Notes:
 * 990728 -
 *          1. 1.0 g/mol <-> 1.0 au;
 *          2. 1.0 kT    <-> 0.8314 au Angstrom^2 / ps^2
 * 991006 -
 * 991018 - Modify the program such that after escape, the system
 *          picks up a new site, instead of retrieving from a site
      list.
 *
 * 000131 - Remove the above modification.  If a particle escapes
      from a
 *          well, it moves to the next random one.
 */


/*******************************
*        Header Files          *
*******************************/

#include <stdio.h>
#include <stdlib.h>
#include <stddef.h>
#include <math.h>
#include <string.h>
```

The simulation begins by declaring all variables and initialing the global constants for the simulation. As described in the code, the base units used in the code are ps, Å, and g/mole. The conversion of Boltzmann's

constant as well as the conversion of centipoise into simulation units is given in the code.

```
/*******************************
*   Global Macro Definition   *
*******************************/

#define      SITE_MAX 7      /* maximal sites a molecule can travel */
#define      TIME_MAX 100000  /* maximal time delay */
#define      TRAJECTORY_MAX 1000  // maximum number of trajectories
#define      N_MAX 512        /* maximum number of particles */
/*******************************
 *  Global Variable Definition *
 *******************************/

const double PI   = 3.14159265358979323846;
const double L    = 3.2;        /* site-site distance = 3.2 A */
const double T_R = 298.15;     /* Room temperature */
const double K_B = 0.8314;     /* Boltzmann constant in the simulation
                                   units(S.U.)*/
const double ETA_AU = 60.22137; /* conversion from cP to S.U. */
double       E_p = 83.33;        /* excess energy from the pump */
double       Ua1 = 3.635;        /* well depth of alkyl site */
double       Ua2 = 2.625;        //  well depth alkyl site
double       Ua3 = 0.0;          //  well depth of third alkyl site
double       Ub  = 19.84;        /* well depth of hydroxyl site */
double       H   = 0.05;     /* the macroscopic viscosity */
double       dt  = 0.001;    /* the time increment (ps) */
double       H0  = 1.0;      /* initial viscosity (cp) */
double       Hf  = 0.3;      /* final viscosity (cp) */
double       tau = 25.0;     /* vibrational cooling time */
double       T0  = 1.39;     // initial temperature
long int     N   = 25;       // number of particles in simulation

double       eta;            //  friction constant eq. 9.13 Allen & T.
double       kT  = 1.0;      /* thermal energy */

/*******************************
 *  Global Function Definition *
 *******************************/
double       rand3(long int *seed_flag); //random  number generator
double       gauss(void);                //gaussian deviate generator
/*  calculates the force on simulation particle  */
double force(double [], double, double *, int);
/*  calculates deviate for position and velocity  */
void stochastic(double, double, double, double *,double *);
/*  sorts potential in ascending numerical order  */
void piksrt(double arr[4]);

/*******************************
*     Main Program Begins     *
*******************************/
```

```
int main(int argc, char *argv[])
{
  /*******************************
   *     Variable Definition     *
   *******************************/
  /*  INPUT AND OUTPUT FILE VARIABLES  */
  const int   file_length = 32;//  maximum file name string length
  char        in_file[80];  //  name of the input file
  char        out_file[80]; //  base name of output file
  char        filename[80]; //  name of output file written to
  FILE        *ifp, *ofp;   //  file pointers - C style
  FILE        *dfp;         //  pointer for trajectory file
  int         index_traj;   //  trajectory index
  register int  index1;     //  index over particles
  register int  index2;     //  another index variable
  int         t_counter;    //  time step counter for output purposes
  double      boltzmann_scale; //  boltzmann scaling factor for
                             //  velocities
  double      tmp1, tmp2, tmp3;  //  temporary storage variables
  double      sigma_r, sigma_r2;// variance and deviate of gaussian r
  double      sigma_v, sigma_v2;// variance and deviate of gaussian v
  double      c_rv;             /* correlation constant of r and v */
  double      dr, dv;       /* stochastic displacements of r and v */
  double      site[SITE_MAX+1]; // potential of mean force array
    /* array containing potential information
       site[i]: value of U at position i  */
  int         s[N_MAX], old_s[N_MAX]; /* site index: says which site
                                         the particle is at  */
  double      U[4];           /* array containing well depths
                                 U[0]: hydroxyl site;
                                 U[1..3]: alkyl sites. */
  double      xred;           //  reduced x position
                              //  x -axis projection onto s axis
  double      xinit;          //  temporary position variable
  long int    rand_flag = 1;  /* rand3 flag - initializes random
                                 number generator */
  double      c0, c1, c2;     //  Integration constants
  double      a[N_MAX], v[N_MAX], x[N_MAX]; /* storage for
                                               acccelleration,
                                               velocity, position */
  double      a_old[N_MAX], v_old[N_MAX], x_old[N_MAX]; /* storage
                                               of  previous values */
  double      t, t_max;  // time index information
  int         output_interval = 1000; //number of steps between write
  double      e_total = 0.0;    // total energy
  double      pes, e_k, e_pes;  // potential, kinetic, and sum of
                                // potential energies
  double      m = 192.0;        /* Molecular weight for Cr(CO)5 */
  int       trajectory;     //  number of trajectories
  int    complete = 0;      /* an integeter to indicate if the
                               simulation is over */
  long int    num_jumps, num_back;  // hopping statistics
```

This part of the code prints the information for the current version of the code to the standard output. Notice the C-preprocessor calls "#ifdef." The version of the code is determined by specific preprocessor directives during compilation. Details for the compilation are given below.

```
  /*******************************
   *     PRINT VERSION INFO       *
   *     n-Propanol - V2          *
   *******************************/
  fprintf(stdout,"Program n_propanol.\n");
  fprintf(stdout,"Brownian Motion Simulator.\n");
  fprintf(stdout,"Random cooordination Version 2.0.\n");
#ifdef CSTAT
  fprintf(stdout,"Carbon Statistics.  ");
#else
  fprintf(stdout,"Hydrogen Statistics.  ");
#endif  //CSTAT
#ifdef RANDOM
  fprintf(stdout,"Random Hopping.\n");
#else
  fprintf(stdout,"Non-random Hopping.\n");
#endif  //RANDOM
  /*****************************************************************/
```

The program then reads the command line to determine the filename that contains all the parameters for the simulation. If a filename is not given, the filename "temp" is read. If this filename is not present, then the program quits.

```
   /*******************************
   *     Read Input Files         *
   *******************************/
  if (argc == 1){
    strcpy(in_file,"temp");
  }
  else if (argc == 2){
    if (strlen(argv[1]) > file_length){
```

```
    fprintf(stderr,"bm_simulator (file_in) must be less than ");
    fprintf(stderr,"%i characters long.\n",file_length);
    exit(1);
  }  //end if
  else{
    strcpy(in_file,argv[1]);
  }  //end else
}  // end else if
else {
  fprintf(stderr,"Usage: bm_simulator file_in(opt)\n");
  exit(1);
}

/*  Actually Read in data  */
ifp = fopen( in_file, "r" );
if (ifp == NULL){
  fprintf(stderr,"Error:  Can not open the file: %s\n",in_file);
  exit(1);
}
// READ IN SET-UP PARAMETERS
fscanf( ifp, "%s\n", out_file );
fscanf( ifp, "%i\n", &trajectory );
fscanf( ifp, "%li\n", &N );
fscanf( ifp, "%i\n", &output_interval );
fscanf( ifp, "%lf\n", &E_p );
fscanf( ifp, "%lf\n", &Ua1 );
fscanf( ifp, "%lf\n", &Ua2 );
fscanf( ifp, "%lf\n", &Ua3 );
fscanf( ifp, "%lf\n", &Ub );
fscanf( ifp, "%lf\n", &Hf );
fscanf( ifp, "%lf\n", &dt );
fscanf( ifp, "%lf\n", &H0 );
fscanf( ifp, "%lf\n", &T0 );
fscanf( ifp, "%lf\n", &tau );
fclose( ifp );

/* Some error checking */
if (N > N_MAX)
  N = N_MAX;
if (trajectory > TRAJECTORY_MAX)
  trajectory = TRAJECTORY_MAX;
/*  assign potential values to U array */
U[0]     = Ub;
/*  Checks to see that Ua's are assigned properly  */
/*  Wells are always deepest near the alkyl potential */
U[1] = Ua1;
U[2] = Ua2;
U[3] = Ua3;

/* sorts the potentials into ascending order */
piksrt(U);
```

Again, we use C-preprocessor calls to create the output files.

```
  /*******************************
   *    Write Parameter Files    *
   *******************************/
#ifdef RANDOM
#ifdef CSTAT
  strcpy( filename, out_file );
  strcat( filename, ".cr.parm" );
#else
  strcpy( filename, out_file );
  strcat( filename, ".hr.parm" );
#endif  //CSTAT
#else //NonRandom
#ifdef CSTAT
  strcpy( filename, out_file );
  strcat( filename, ".cn.parm" );
#else
  strcpy( filename, out_file );
  strcat( filename, ".hn.parm" );
#endif  //CSTAT
#endif  //RANDOM
  ofp = fopen( filename, "w" );

  fprintf( ofp, "Output filename          : %s\n", out_file );
  fprintf( ofp, "Number of trajectories   : %i\n", trajectory );
  fprintf( ofp, "Number of particles      : %li\n", N );
  fprintf( ofp, "Output interval          : %i\n", output_interval );
  fprintf( ofp, "Excess energy (kT)       : %f\n", E_p );
  fprintf( ofp, "Alkyl potential (alpha)  : %f\n", Ua1 );
  fprintf( ofp, "Alkyl potential (beta)   : %f\n", Ua2 );
  fprintf( ofp, "Alkyl potential (gamma)  : %f\n", Ua3 );
  fprintf( ofp, "Hydroxyl potential       : %f\n", Ub );
  fprintf( ofp, "Final viscosity (cp)     : %f\n", Hf );
  fprintf( ofp, "Time increment (ps)      : %f\n", dt );
  fprintf( ofp, "Initial viscosity (cp)   : %f\n", H0 );
  fprintf( ofp, "Initial temperature (K)  : %f\n", T0 );
  fprintf( ofp, "Vibrational cooling time: %f\n", tau );
  fprintf( ofp, "Hopping Distance         : %f\n", L );
  fprintf( ofp, "Particle mass (g/mol)    : %f\n", m );
  fclose( ofp );

  /*  Prepare the output data file for writing  */
  //  Open it and KEEP it open
#ifdef RANDOM
#ifdef CSTAT
  strcpy( filename, out_file );
  strcat( filename, ".cr.dat" );
#else
  strcpy( filename, out_file );
  strcat( filename, ".hr.dat" );
```

```
#endif  //CSTAT
#else //NonRandom
#ifdef CSTAT
  strcpy( filename, out_file );
  strcat( filename, ".cn.dat" );
#else
  strcpy( filename, out_file );
  strcat( filename, ".hn.dat" );
#endif  //CSTAT
#endif  //RANDOM

  dfp = fopen( filename, "wb" );


      /*****************************************************************
      ******
*****************************************************************/
```

Next, we initialize all the variables prior to running the simulation. This is where the integration constants for the numerical solution to Langevin's equation appear.

```
  /*******************************
   *       Initialization        *
   *******************************/
  num_jumps = 0;
  num_back = 0;
  kT = 1.0;
  eta = H0 * ETA_AU;                    /* velocity damping constant */
  kT = K_B * T_R;                       /* Boltzmann Constant * T_R */

  /*  Calculate magnitude of position deviate  */
  tmp1     = eta * dt;
  tmp2     = 3 - 4 * exp( - tmp1 ) + exp( - 2 * tmp1 );
  tmp3     = ( 2 - tmp2 / tmp1 ) / tmp1;
  sigma_r2 = tmp3 * kT / m * dt * dt;
  sigma_r  = sqrt( sigma_r2 );

  /*  Calculate magnitude of velocity deviate */
  tmp2     = 1 - exp( - 2 * tmp1 );
  sigma_v2 = tmp2 * kT / m;
  sigma_v  = sqrt( sigma_v2 );

  /*  Calculate correllation coefficient  */
  tmp2     = 1 - exp( - tmp1 );
  tmp2     = tmp2 * tmp2;
  tmp3     = dt * kT / m / tmp1 * tmp2;
  c_rv     = tmp3 / sigma_r / sigma_v;
```

```
/*  Determine Integration Constants  */
c0        = exp( - tmp1 );
c1        = ( 1 - c0 ) / tmp1;
c2        = ( 1 - c1 ) / tmp1;

/*******************************
 *      Simulation Begins      *
 *******************************/
/*  Assign variable values which do not change over trajectory  */
t_max = TIME_MAX;
boltzmann_scale = sqrt( K_B * T_R / m );
```

The following lines generate the potential energy surface that the transition metal fragment experiences.

```
/***** Create the potential-of-mean-force array *****/
site[0] = 0;
for ( index2 = 0; index2 < 4; ++index2 ) {
  /*  The following two lines of code generate a symmetric potental
      well for n-propanol  */
  site[4-index2] = U[4 - index2 - 1];
  site[4+index2] = U[4 - index2 - 1];
}
```

Here, we begin the simulation. We run random walk trajectories over all the particles in the simulation. When all of the particles have been trapped in the deep alcohol potential, we call that a single trajectory. A number of trajectories (usually 6-10) are run to gather statistics.

```
for ( index_traj=1; index_traj <= trajectory; ++index_traj ) {

  //  Initialize Variables
  t_counter = output_interval;        // set counter to record
    values
  /*  Zero Energies  */
  e_k = 0.0;
  e_pes = 0.0;
  complete = 0;
  /*  helpful output */
  fprintf(stdout,"Beginning trajectory %i\n",index_traj);
  fflush(stdout);
```

```
/*******************************
 *      Initial Conditions     *
 *******************************/

/***** Assign initial velocities *****/
pes = 0.0;

/********** Loop over every particle to **********/
/* (1) assign initial velocity;                  */
/* (2) assign a random array to each particle.   */
/*************************************************/
for ( index1 = 0; index1 < N; ++index1 ) {
```

Next, we determine the initial solvation statistics. The solvation is dependent upon the statistics of the simulation, namely, the number of carbon-based or the number of hydrogen-based binding sites. Here we use the preprocessor directives to determine the coding for the solvation.

```
      /*  These next 5 lines properly take into account the
          statistics for generating the randomly solvated species */
#ifdef CSTAT  // using carbon stats to determine solvation statistics
      xred = 8.0 * rand3(&rand_flag) + 1.0;
      xred = floor(xred);
      if (xred > 7.0)
        xred = 4.0;
#else   //  using hydrogen stats to determine solvation statistics
      xred = rand3(&rand_flag);
      //  3 in 9 chance that you will coordinate to the end gamma
      carbon
      if ( (xred >= 0.0) && (xred < (1.0/3.0)) )
        xred = 4.0;
      //  2 in 9 chance that you will coordinate to the beta carbon
      else if ( (xred >= (1.0/3.0)) && (xred < (5.0/9.0)) )
        xred = 3.0;
      //  2 in 9 chance that you will coordinate to the alpha carbon
      else if ( (xred >= (5.0/9.0)) && (xred < (7.0/9.0)) )
        xred = 2.0;
      //  rest of probability (2 in 9) that you will be hydroxyl
      bound
      else
        xred = 1.0;

#endif  // CSTAT
```

```
      /***** Current site *****/
      s[index1] = (int)(xred);
      old_s[index1] = s[index1];

      /***** Initial position, velocity, and accelleration *****/
      x[index1] = x_old[index1] = xred * L;
      v[index1] = v_old[index1] = boltzmann_scale * gauss();
      a[index1] = 0.0;

      a_old[index1] = force( site, xred, &pes, s[index1] ) / m;

      e_pes = e_pes + pes;
    }  /* end loop over particles - Initialization */
    //  Reset the time at the beginning of each trajectory
    t = 0.0;


      /*****************************************************************
      ****/
    /* only write out the potential energy surface  and the site
       information if debug option is defined in the preprocessor
       and index_traj == 1                                            */
/*******************************************************************/
/*******************************************************************/

    //  Can probably cut this line
    kT = K_B * T_R;                    /* Boltzmann Constant * T_R */

    /*  Loop through particles RUNNING THE SIMULATION ! */
```

The following loop is the heart of the simulation, and references are made to the book by Allen and Tildesley[80]. The code loops over each of the particles, moves the particles, and then recalculates the site information. This site information is then used to determine the force on the particle, which is in turn used to calculate the velocity. The calculation of the position and velocity steps are based on a modified velocity-Verlet algorithm.

```
while ( (complete < N) && (t < t_max) ) {

  /*  allows for viscosity to change over time  */
  H = (H0 - Hf) * exp( -t/tau ) + Hf;
  eta = H * ETA_AU; /* velocity damping constant */

  /*  Recalculate position deviate  */
  tmp1     = eta * dt;
  tmp2     = 3 - 4 * exp( - tmp1 ) + exp( - 2 * tmp1 );
  tmp3     = ( 2 - tmp2 / tmp1 ) / tmp1;
  sigma_r2 = tmp3 * kT / m * dt * dt;
  sigma_r  = sqrt( sigma_r2 );

  /*  Recalculate velocity deviate  */
  tmp2     = 1 - exp( - 2 * tmp1 );
  sigma_v2 = tmp2 * kT / m;
  sigma_v  = sqrt( sigma_v2 );

  /*  Recalculate correllation coefficient  */
  tmp2     = 1 - exp( - tmp1 );
  tmp2     = tmp2 * tmp2;
  tmp3     = dt * kT / m / tmp1 * tmp2;
  c_rv     = tmp3 / sigma_r / sigma_v;

  /*  Recalculate integration constants  */
  c0       = exp( - tmp1 );
  c1       = ( 1 - c0 ) / tmp1;
  c2       = ( 1 - c1 ) / tmp1;

  /*  Zero Energies  */
  e_k = 0.0;
  e_pes = 0.0;
  complete = 0;

  /*  Loop over particles and update the positions, velocities,
      accellerations, etc.  */
  for ( index1 = 0; index1 < N; ++index1 ) {

    /*******************************
     *       Stochastic Force      *
     *******************************/
    stochastic( sigma_r, sigma_v, c_rv, &dr, &dv );
    /*************************************************************
     *      Move Formula 9.24a Allen & Tildesley                 *
     *************************************************************/
    x[index1]=x_old[index1]+ \
             c1*v_old[index1]*dt+c2*a_old[index1]*dt*dt+dr;

    /*  Determine Site  */
    xred = x[index1] / L;
    if (floor( xred ) == floor( xred + 0.5 ))
      s[index1] = (int) floor( xred );
    else
      s[index1] = 1 + (int) floor( xred );
```

Here we determine if the particle has hopped onto a new site. If it has, then the code places the particle onto a new binding-site potential well, based on the statistics determined by calls to the preprocessor.

```
        /***** If new site != old site, change site *****/
        if ( s[index1] != old_s[index1] ) {
          ++num_jumps;
          if (old_s[index1] == 1 || old_s[index1] == 7) {
            ++num_back;
          }
#ifdef RANDOM  // if we are randomly hopping then:
        /*  These next few lines properly take into account the
         *  statistics for generating the randomly solvated species
         *  These lines are only included if RANDOM is sent to
         *  the preprocessor.
         */

#ifdef CSTAT  // using carbon statistics
          xinit = 4.0 * rand3(&rand_flag) + 1.0;
          xinit = floor(xinit);
#else   // CSTAT-using hydrogen statistics
          xinit = rand3(&rand_flag);
        //  3 in 9 chance that you will coordinate to the end carbon
          if ( (xinit >= 0.0) && (xinit < (3.0/9.0)) )
            xinit = 4.0;
        //  2 in 9 chance that you will coordinate to the beta carbon
          else if ( (xinit >= (3.0/9.0)) && (xinit < (5.0/9.0)) )
            xinit = 3.0;
        //  2 in 9 chance that you will coordinate to the alpha-C
          else if ( (xinit >= (5.0/9.0)) && (xinit < (7.0/9.0)) )
            xinit = 2.0;
        //  rest of probability (2 in 9) that you will be OH bound
        //  assume two lone pairs are equivalent to 2-H's
          else
            xinit = 1.0;

#endif  // CSTAT

#else   //  RANDOM -- can still hop but only to s[i] +/- 1
        //  THIS IS FOR NON-RANDOM HOPPING
#ifdef CSTAT  /* THESE COORDINATION STATISTICS ARE ONLY TRUE FOR
     * CARBON SOLVATION !!!!! */
          xinit = rand3(&rand_flag);
    //  50 / 50 chance of hopping to the next site
          if ( (xinit >= 0.0) && (xinit < 0.50) && (old_s[index1] <\
                SITE_MAX))
```

```
        xinit = (double)(old_s[index1]) + 1.0;
      //  50 / 50 chance of hopping to previous site except if
      //    s[i] = 1
      else if (s[index1] > 1)
        xinit = (double)(old_s[index1]) - 1.0;
      //  only if supposed to be negative but s=1
      else
        xinit = (double)(old_s[index1]) + 1.0;
```

For non-random hopping using hydrogen statistics, we assume that the "hop" event carries the metal fragment to the hydrogen on another carbon. This is not necessarily true. In fact, the metal fragment could hop to another hydrogen on the same carbon, but the rearrangement would then take significantly longer. This is discussed in chapter 3. We also count the number of times a particle hops over the barrier, and whether or not the particle hops back through diffusion.

```
#else   //  CSTAT - USE HYDROGEN STATISTICS
      //  FOLLOWING CODE SAYS THAT S[INDEX1] MUST BE +/- 1 of
      //  OLD_S[INDEX1]
      //  COULD ALSO ARGUE THAT YOU CAN JUMP ONTO ANOTHER
      // HYDROGEN ON
      //  THE SAME CARBON, BUT THAT WILL HAVE TO COME LATER!!!
      if (old_s[index1] == 4){
        xinit = 3.0;
      }
      //  From beta can go to gamma with 3 / 5 chances
      else if (old_s[index1] == 3 || old_s[index1] == 5){
        xinit = rand3(&rand_flag);
        if ( (xinit >= 0.0) && (xinit < (3.0/5.0)) )
          xinit = 4.0;
        else
          xinit = 2.0;
      }
      //  from alpha can jump to O or beta with equal prob.
      else if (old_s[index1] == 2 || old_s[index1] == 4){
        xinit = rand3(&rand_flag);
        if ( (xinit >= 0.0) && (xinit < (1.0/2.0)) )
          xinit = 3.0;
```

```
            else
              xinit = 1.0;
          }

          else      // old_s[index1] == 1 or 5
            xinit = 2.0;

#endif  // CSTAT - non-random
#endif  //  RANDOM

          /* determines the x - offset (not at bottom of well
             anymore) */
          /*  x-offset is just x[0] - (double)(s[i]) */
          /* and assigns x-value based on new s[i] */
          xred = (xinit + xred - (double)(s[index1]) );
          x[index1] = xred * L;
          /*  assigns new s-value */
          s[index1] = (int)(xinit);

          /*  Now we just let the particle change
           *  positions with the following line: */
          old_s[index1] = s[index1];
        }  /*  end if s[index1] != s_old[index1]  */

        /*******************************
         *     Deterministic Force     *
         *******************************/
        a[index1] = force(site, xred, &pes, s[index1] ) / m;

      /*************************************************************
       *     Update Velocity - Formula 9.24b Allen and Tildesley   *
       *************************************************************/
        v[index1]=c0*v_old[index1]+
                  (c1-c2)*dt*a_old[index1]+c2*a[index1]*dt+dv;

        /*  Update old values of the position, velocity, and
            accelleration  */
        x_old[index1] = x[index1];
        v_old[index1] = v[index1];
        a_old[index1] = a[index1];
```

The next lines record how many particles are trapped in the deep hydroxyl potential at any given time. We use this number to determine if the simulation is finished.

```
        /*  if particle is in the hydroxyl well it is most likely
            trapped */
        if ( site[s[index1]] == Ub )
          complete++;
```

```
        /*  sum up kinetic and potential energies  */
        e_k = e_k + v[index1] * v[index1];
        e_pes = e_pes + pes;

      }  //  End sum over particles

      /******************************
       *      Calculate Results      *
       ******************************/

      //  correct kinetic energy
      e_k *= (0.5 * m);
```

Here, every output_interval number of time steps, the number of particles trapped in the hydroxyl well and the simulation energy is recorded to file.

```
      if ( t_counter >= output_interval ) {

        t_counter = 0;  // reset counter
        e_k = e_k/kT;
        e_pes = e_pes/kT;
        /******************************
         *        Output Results       *
         ******************************/
        fwrite(&t, sizeof(double), 1, dfp);
        fwrite(&complete, sizeof(int), 1, dfp);
        fwrite(&e_k, sizeof(double), 1, dfp);
        fwrite(&e_pes, sizeof(double), 1, dfp);
      }

      ++t_counter;  //  Update counter
      t += dt;      //  Increment time axis

    }       /*  end while-loop which runs simulation  */
            } /* End of for index_traj, TRAJECTORY_MAX */
  //  CLOSE Output file
  fclose( dfp );
```

At the end of the simulation we output the total energy, and the hopping statistics for the Markov process.

```
  /******************************
   *        Output Results       *
   ******************************/
  //  sum kinetic and potential energy
  e_total = e_k + e_pes;
```

```
  fprintf(stdout, "Simulation ends at E_total = %f.\n", e_total );
  //  calculate the average number of hops/particle
  tmp1 = ((double)(num_jumps)) / ((double)(N*trajectory));
  fprintf(stdout, "Average Number of hops = %f.\n", tmp1);
  tmp1 = ((double)(num_jumps-num_back)) / ((double)(N*trajectory));
  fprintf(stdout, "Average Number of hops from alkyl-bound = %f.\n",\
          tmp1);

  return 0;
} /* End of main() */
```

The following function, stochastic, calculates a pair of numbers sampled from a bivariate Gaussian distribution in order to determine the random deviate in the Brownian motion simulation[80, 115].

```
/*******************************
 *        stochastic()         *
 *******************************/
/* sigma_r: gaussian deviate for position    */
/* sigma_v: gaussian deviate for velocity    */
/* c_rv   : correlation between r and v      */
/* dr     : calculated position displacement */
/* dv     : calculated velocity displacement */
void stochastic( double sigma_r, double sigma_v, double c_rv, double
      *dr, double *dv )

{
  double          x1, x2;

  x1  = gauss();
  x2  = gauss();
  *dr = sigma_r * x1;
  *dv = sigma_v * (c_rv * x1 + sqrt( 1 - c_rv * c_rv ) * x2 );

} /* End of dr_g() */
```

The following function, force, calculates the potential and the associated force experienced by an individual particle.

```
/*******************************
 *          force()             *
 *******************************/

double force(double site[SITE_MAX+1], double xred, double *pes, int s
      )
{
  double          V;      // potential energy value
  double          ans;    // return value

  ans = 2 * PI * site[s] * sin( (2 * xred + 1) * PI );
  V = site[s] * ( cos( ( 2 * xred + 1 ) * PI ) - 1 );

  *pes = V;   //  offset - bottom of deepest well
  *pes = *pes * K_B * T_R;

  ans = ans * ( K_B * T_R ) / L;

  return ans;

} /* End of force() */
```

Function piksrt simply sorts the individual potential values into ascending order. This assures that the potential model that we generate has the proper statistics.

```
/*  sorts alkyl potentials in descending numerical order  */
void piksrt(double arr[4])
{
  int index1,index2;
  double tmp;

  //  Only sorts arr[1..3] - the alkyl values
  for (index2 = 2; index2 < 4; ++index2) {
    tmp = arr[index2];
    index1 = index2 - 1;
    while (index1 > 0 && arr[index1] < tmp) {
      arr[index1 + 1] = arr[index1];
      --index1;
    }
    arr[index1 + 1] = tmp;
  }
}
```

The random number generator used in the simulations was based on a the rand3() code given by Press et. al.[44]. It was slightly modified to use a random seed from the C-library rand() function. Random Gaussian deviates were calculated based on a routine given in *Computer Simulations of Liquids*[80]. The code for both functions appears below:

```
/*****************************************************************
 *  Rand.c:                                                      *
 *  Source for a random number generator and random gaussian     *
 *  deviate generator from:                                      *
 *  "Numerical Recipies in C: The Art of Scientific Computing"   *
 *  2nd edition, by W.H Press, S.A. Teukolsky, W.T. Vetterling,  *
 *  and B.P. Flannery, 1994, pages 283, and 289                  *
 *---------------------------------------------------------------*
 *  Function:   long double rand3(int *seed_flag)                *
 *                  *seed_flag < 0 initialize otherwise return   *
 *                  a random variable on 0..1                    *
 *  Function:   long double gauss(int *seed_flag)                *
 *                  returns a random gaussian deviate with       *
 *                  variance of 1.0.  If *seed_flag is < 0       *
 *                  we re-initialize the rand class variable     *
 *                                                               *
 *****************************************************************/

/*  Local includes  */
#include <math.h>
#include <time.h>
#include <stdlib.h>
#include <limits.h>


/*  Here are the constant variables for the randomizer */
const long int MBIG = 1000000000;
const long int MSEED = 161803398;
const long int MZ = 0;
const double FAC = (1.0 / 1000000000.0 );

double rand3(long int *seed_flag)
{
  /*  Integers which determine which of ma[i] values to use
      in order to create random deviates    */
```

```
static long int inext, inextp;
/*  The array which holds the numbers which are manipulated
    into the random deviates  */
static long int ma[56];
/*  initialization flag - at start-up it is set to false = 0 */
static long int iff = 0;
/*  variables for initializing the ma[56] */
long int mj, mk;
/*  The value used to calculate the seed - temporary variable */
double      double_seed;
/*  The seed for the library function rand() */
time_t      seed;
/*  index variables used in initialization loops */
int         index_1, index_2, index_3;

/* initializtion begins by sending *idum as < 0 OR if the first
    running
   of the function occurs ( iff == 0 ) */
if (*seed_flag < 0 || iff == 0) {

  /*  set flag to TRUE  */
  iff = 1;

  /*  Here, we are going to generate a seed from the standard
    rand function, but first we have to seed the library
    rand() function */
  seed = time(NULL);
  srand(seed);
  while (1){
    /*  Get a random number for double_seed */
    double_seed = (double)(rand());
    /*  Make sure that double_seed > 0  */
    if (double_seed > 0.0)
    break;
  }

  /*  double_seed can have a maximum value of RAND_MAX
      We can't have the seed value of double_seed > MSEED
      so we'll make sure that double_seed is at least < MSEED /
    10,000 */

  double_seed =
    double_seed/((double)(RAND_MAX))*((double)(MSEED))/10000.0;

  /*  Now, initialize the other variables, mj & ma */
  mj = MSEED - ((long int)(double_seed));
  mj = mj % MBIG;
  /*  Initialize the last value of ma */
  ma[55] = mj;
  mk = 1;

  /*  Initialize the rest of the ma array */
  for (index_1 = 1; index_1 < 55; ++index_1) {
      index_2 = (21 * index_1) % 55;
```

```
        ma[index_2] = mk;
        mk = mj - mk;
        if (mk < MZ)
            mk = mk + MBIG;
        mj = ma[index_2];
    }

    /*  "Warm-up" the generator  */
    for (index_3 = 1; index_3 <= 4; ++index_3)
        for (index_1 = 1; index_1 <= 55; ++index_1) {
            ma[index_1] = ma[index_1] - ma[1+(index_1 +30) % 55];
            if (ma[index_1] < MZ)
                ma[index_1] = ma[index_1] + MBIG;
        }
    inext = 0;
    inextp = 31;
    *seed_flag = 1;
  }

  /*  Increment inext & inextp */
  ++inext;
  ++inextp;

  /*  Check on array index bounds & fix if necessary  */
  if (inext == 56) inext = 1;
  if (inextp == 56) inextp = 1;

  /*  GENERATE NEW RANDOM NUMBER SUBTRACTIVELY!!!  */
  mj = ma[inext] - ma[inextp];
    /*  Check to make sure it is in range */
  if (mj < MZ)
    mj = mj + MBIG;
  /*  Store new number */
  ma[inext] = mj;
//  OUTPUT DEVIATE
  return ((double)(mj) * FAC);
}

/*******************************
 *         gauss()             *
 *******************************
 * Returns a number that conforms to a Gaussian
 * distribution with mean 0 and variance 1
 * The algorithm was taken from Allen and Tildesley pp. 347*/

double gauss(void)
{
  const double    a1 = 3.949846138;
  const double    a3 = 0.252408784;
  const double    a5 = 0.076542912;
  const double    a7 = 0.008355968;
  const double    a9 = 0.029899776;

  double          sum, r, r2, ans;
```

```
  int              index;
  long int         rand_flag = 1;

  sum = 0.0;
  for ( index=1; index<=12; ++index )
    sum += rand3(&rand_flag);
  r  = ( sum - 6.0 ) / 4.0;
  r2 = r * r;
  ans = (((( a9 * r2 + a7 ) * r2 + a5 ) * r2 + a3 ) * r2 + a1 ) * r;

  return ans;

} /* End of gauss() */
```

Finally, a sample Makefile which is used to compile the n-propanol code appears below. It works on the computer workstations running LINUX. Comments describe how the file can be altered to compile the different versions of the code as well as how to compile the code on a DEC workstation running alpha, DEC's proprietary UNIX operating system.

```
#
# Makefile for g++ compiler
# n_propanol code
#
CC = cc
# The following CFLAGS line is for optimization of carbon
# statistics and random hopping
# TO COMPILE OTHER CODES, REMOVE RANDOM FLAG, CSTAT FLAG,
# OR BOTH AND THEN RE-MAKE THE CODE
CFLAGS = -O2 -Wall -DRANDOM -DCSTAT
# The following CFLAGS line is for debugging complilation
#CFLAGS = -g -O2 -Wall -DDEBUG
# The following CFLAGS ARE FOR VERBOSE OPERATION
#CFLAGS = -DVERBOSE
# The following flags are for operation on the DEC
# CFLAGS = -O2 -D#####
LIBS = -lm
SRC = n_propanol.vk2.c rand.c
OBJ = n_propanol.vk2.o rand.o

all : n_propanol
```

```
n_propanol: $(OBJ)
        $(CC) $(CFLAGS) $(LIBS) -o n_propanol_cr $(OBJ)

n_propanol.vk2.o: n_propanol.vk2.c
        $(CC) $(CFLAGS) -c n_propanol.vk2.c

rand.o: rand.c
        $(CC) $(CFLAGS) -c rand.c

clean:
        rm $(OBJ)
```

### A1.2 Differences in Code

As discussed in chapter 3, the different binding sites of the individual alcohols have unique binding energies. This site-specific structure is incorporated into the potential energy surfaces of the different simulations. Furthermore, the statistical nature of the "hopping" process is also unique to the different alcohols. The main code variations, therefore, appear in the code that controls the generation of the potential energy surface, the initial solvation statistics, and determining how the transition metal fragment "hops". Slight differences appear in how the input and output files are formatted, but these have been left of the following discussion. The initial solvation statistics are based on the number of alkyl or hydroxyl binding sites. The exact number of these sites is arbitrary, and only affects the scaling pre-factor in the Williams-Watt

equation. For this reason these code differences are also left out below.

### A1.2.1 Generation of the Potential Energy Surface

Because 2-propanol and ethanol both have an alpha carbon, a beta carbon, and a hydroxyl binding site, the potential energy surface is identical for the two alcohols. The differences arise from the values for U[i] read into the program. The potential generation is as follows:

```
/***** Create the potential-of-mean-force array *****/
  site[0] = 0;
  for ( index2 = 0; index2 < 3; ++index2 ) {
    /*  The following two lines of code generate a symmetric potental
        well for ethanol -- same for isopropanol, just the solvation
        statistics change  */
    site[3-index2] = U[3 - index2 - 1];
    site[3+index2] = U[3 - index2 - 1];
  }
```

Methanol has only one alkyl binding site, and the resulting code is simply:

```
/***** Create the potential-of-mean-force array *****/
  site[0] = 0.0;
  for ( index2 = 0; index2 < 2; ++index2 ) {
    /*  The following two lines of code generate a symmetric potental
        well for ethanol */
    site[2-index2] = U[2 - index2 - 1];
    site[2+index2] = U[2 - index2 - 1];
  }
```

### A1.2.2 Calculating Hopping Statistics

In this simulation, each particle walks along the potential energy surface described in the previous section. When a particle crosses the top of a barrier, it is assigned to a new site along the potential energy surface. The exact details of how this is accomplished are determined by whether or not the particle is randomly hopping between all sites and by the solvation statistics of the model, e.g. carbon or hydrogen. The code for 2-propanol is as follows:

```
/***** If new site != old site, change site *****/
        if ( s[index1] != old_s[index1] ) {
          /*  add to total number of jumps  */
          num_jumps = num_jumps + 1;
          /*  if old site was a bound one, count it as special  */
          if ((old_s[index1] == 1) || (old_s[index1] == 5))
            num_back = num_back + 1;
#ifdef RANDOM  // if we are randomly hopping then include the
               // following code:
        /*  These next few lines properly take into
         *  account the statistics
         *  for generating the randomly solvated species
         *  These lines are only included if RANDOM is sent to
         *  the preprocessor.
         */
#ifdef CSTAT  // using carbon statistics to determine solvation
              // statistics
          xinit = 8.0 * rand3(&rand_flag) + 1.0;
          xinit = floor(xinit);
          if (xinit > 5.0)
            xinit = 3.0;
#else   //  using hydrogen statistics to determine solvation
          xinit = rand3(&rand_flag);
          //  6 in 9 chance that you will hop to the end carbón
          if ( (xinit >= 0.0) && (xinit < (6.0/9.0)) )
            xinit = 3.0;
          //  1 in 9 chance that you will hop to the alpha carbon
          else if ( (xinit >= (6.0/9.0)) && (xinit < (7.0/9.0)) )
            xinit = 2.0;
          //  rest of probability (2 in 9) will be hydroxyl bound
```

```
          else
            xinit = 1.0;
#endif  // CSTAT
#else   // RANDOM -- can still hop, but only to s[i] +/- 1
/* THE FOLLOWING LINE IS COMMENTED OUT b/c CSTAT AND HSTAT ARE SAME*/
//#ifdef CSTAT
              /* THESE COORDINATION STATISTICS ARE ONLY TRUE FOR
               * CARBON SOLVATION !!!!! */
              /*   STATISTICS ARE STANGE FOR ISO_PROPANOL BECAUSE IT
                   is a branched alcohol so hopping off the alpha
                   carbon is wierd   */
          //  if we are on the beta carbon, can only go to alpha
          if (old_s[index1] == 3)
            xinit = 2.0;
          //  if we are on the OH and happen to come off, can only
          //  go to the adjacant alpha carbon
          else if ((old_s[index1] == 1) || \
                   (old_s[index1] == SITE_MAX))
            xinit = 2.0;
          else {
            xinit = rand3(&rand_flag);
          //  1 / 3 chance of hopping to the hydroxyl
            if ( (xinit >= 0.0) && (xinit < (1.0/3.0) ) )
              xinit = 1.0;
            else
              xinit = 3.0;
          }
#endif  //  RANDOM

          /* determines the x - offset (not at bottom of well
      anymore) */
          /*  x-offset is just x[0] - (double)(s[i]) */
          /* and assigns x-value based on new s[i] */
          xred = (xinit + xred - (double)(s[index1]) );
          x[index1] = xred * L;
          /*  assigns new s-value */
          s[index1] = (int)(xinit);
```

The code for ethanol appears as:

```
/***** If new site != old site, change site *****/
        if ( s[index1] != old_s[index1] ) {
        // count-up hops
          ++num_jumps;
          if ( (old_s[index1] == 1) || (old_s[index1] == 5) )
            num_back = num_back + 1;
#ifdef RANDOM  // if we are randomly hopping then include the
      following code:
          /*  These next few lines properly take into account the
           *  solvation statistics
           *  for generating the randomly solvated species
           *  These lines are only included if RANDOM is sent to
```

```
           *  the preprocessor.
           */
#ifdef CSTAT  // using carbon statistics to determine solvation
          xinit = 3.0 * rand3(&rand_flag) + 1.0;
          xinit = floor(xinit);
#else   //  using hydrogen statistics to hop solvation statistics
          xinit = rand3(&rand_flag);
          //  3 in 7 chance that you will hop to the end carbon
          if ( (xinit >= 0.0) && (xinit < (3.0/7.0)) )
            xinit = 3.0;
          //  2 in 7 chance that you will hop to the alpha carbon
          else if ( (xinit >= (3.0/7.0)) && (xinit < (5.0/7.0)) )
            xinit = 2.0;
          //  rest of probability (2 in 7) that you will be OH bound
          else
            xinit = 1.0;
#endif  // CSTAT

#else   // RANDOM -- can still hop, but only to s[i] +/- 1
/* HERE AGAIN, WE MAKE NO DISTINCTION BETWEEN NON-RANDOM HOPPING
   FOR HYDROGEN AND CARBON STATISTICS!!!! */
/*#ifdef CSTAT   THESE COORDINATION STATISTICS ARE ONLY TRUE FOR
               * CARBON SOLVATION !!!!! */
          xinit = rand3(&rand_flag);
         //  50 / 50 chance of hopping to the next site
          if ( (xinit >= 0.0) && (xinit < 0.50) && \
                (old_s[index1] < SITE_MAX))
            xinit = (double)(old_s[index1]) + 1.0;
          //  50 / 50 chance of hopping to previous site except if
          //  s[i] = 1 (OH-bound)
          else if (old_s[index1] > 1)
            xinit = (double)(old_s[index1]) - 1.0;
          //  only if supposed to be negative but s=1
          else
            xinit = (double)(old_s[index1]) + 1.0;
#endif  //  RANDOM
```

Solvation in methanol was run only with carbon statistics. The methanol simulations were only run in order to characterize the simulation engine and compare results to Kramers' theory. Random and non-random hopping models were incorporated into the methanol code.

### A1.3 Work-up of the Simulation Data

The data generated by the above simulations were processed with two programs. The first was a program named bindataworkup, which sorts out all the data along a single time axis using a quicksort routine, and then calculates the average number and standard deviation of hydroxyl-bound particles at each time step. Bindataworkup was written in the C++-programming language using standard routines, and thus the code is not reproduced here in this section[44]. The second data-work-up program called mcbmerr2.m, was written in the Matlab programming environment. It minimizes a chi-squared fitting function with a numerical simplex algorithm. Data analyses were based on a Monte-Carlo Bootstrap procedure with 256 simulated data sets[43-45].

### A1.4 Characterization of the Simulation Engine

Numerous tests were run in order to ensure that the simulation engine had been coded correctly. The first set of tests simulated the viscosity dependence for a single barrier crossing with a barrier shown in figure 3.4 and described by the equation:

$$V(x) = V_0\left(\frac{x}{l}\right)^4 - 2\left(\frac{x}{l}\right)^2, \qquad \text{A.1}$$

where $l$ is the distance from the barrier minimum to the barrier maximum along the $x$ axis, and $V_0$ is the barrier height. These runs were fit to the Williams-Watts function, which gave single-exponential rates ($\beta$=1). The rates were then plotted against viscosity and were fit to equation 2.4 in order to obtain the curvature constants $\omega_0$ and $\omega_b$. The fits for two different barrier heights ($\Delta E = 1.0\ k_BT$ and $\Delta E = 5.0\ k_BT$) were in excellent agreement with the predicted curvature of the potential energy surface described in equation 2.12. The data points for the 1.0 kBT barrier rates and fits appear in figure A.1. This figure includes code from both the velocity Verlet and Beeman integration algorithms.

The dependence of the decay rate on the integration time-step was also tested. For these tests, a series of methanol rearrangement simulations were carried out. The results were again fit the Williams-Watts potential. As can be seen in figure A.2, the fit parameters $\tau$ and $\beta$ do not change for integration steps ranging from 1 to 50 fs. The integration step of 0.005 ps was chosen for the simulations runs in chapter 3. In all of these runs the temperature remained within 1% of the initial temperature chosen from a Boltzmann distribution.

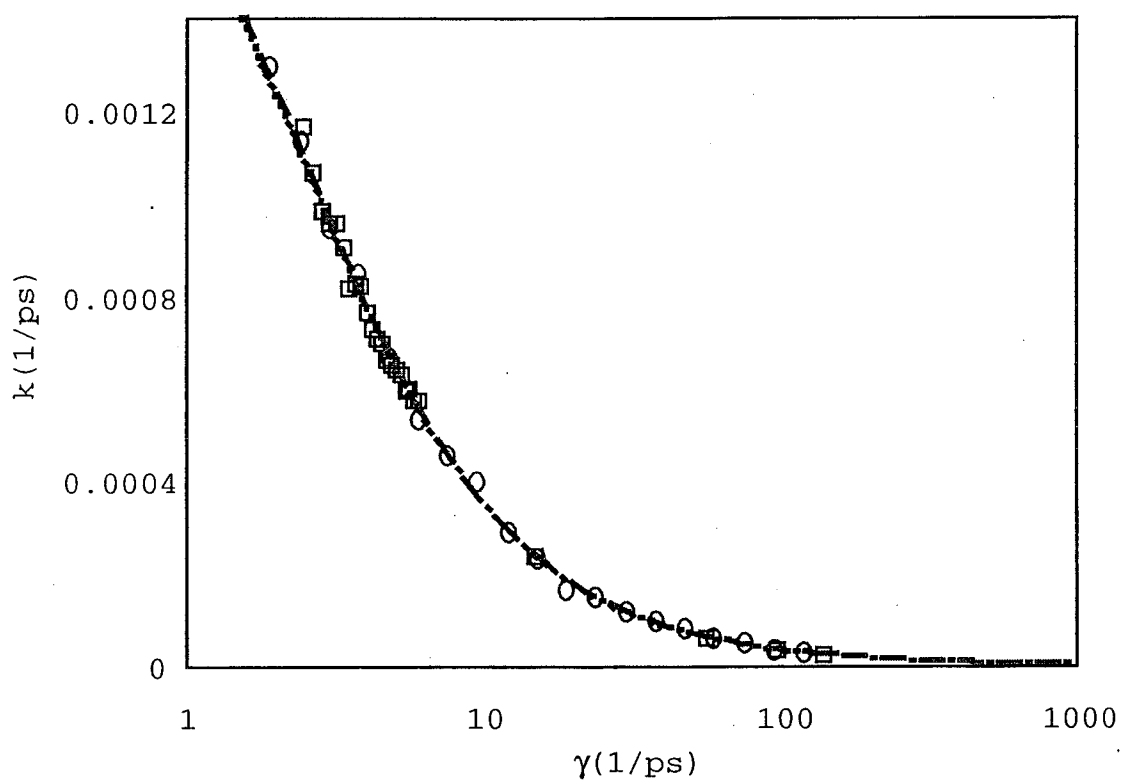


**Figure A.1** Barrier crossing rate versus viscosity for potential given in equation A.1. Both a Beeman, ---□--- , and a velocity Verlet, —○- , integrator were used. The lines are fits to Kramers' equation 3.5.

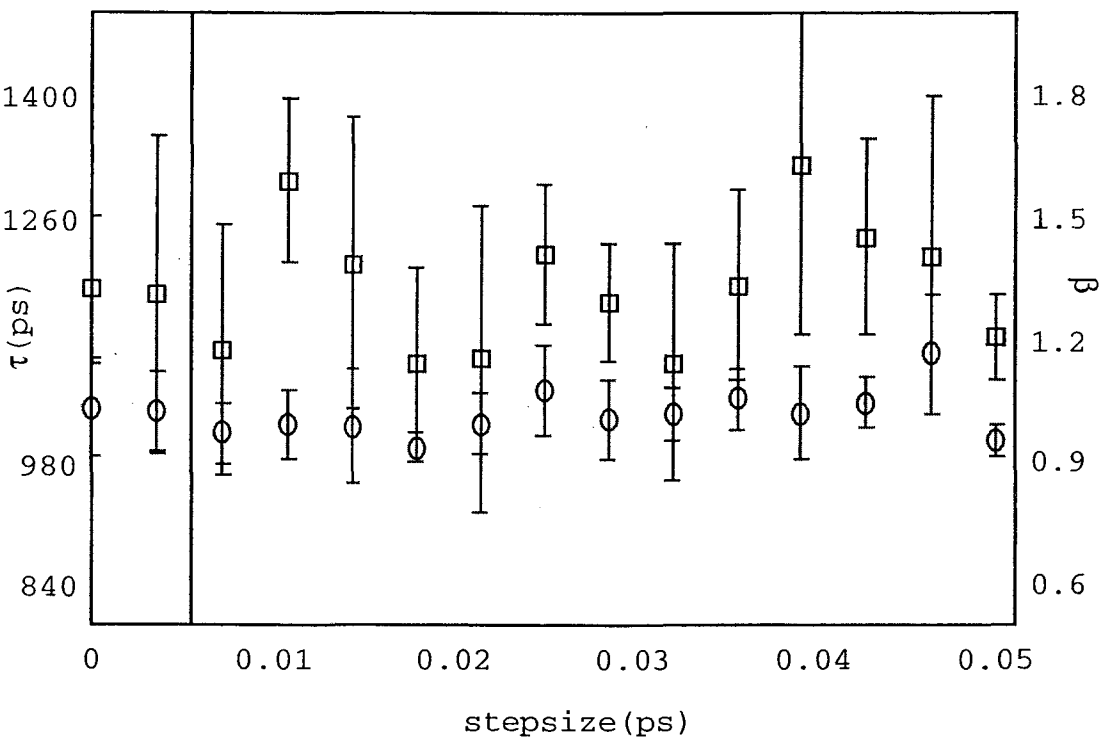


**Figure A.2** Williams-Watts function parameters with errorbars: τ, □ , and β, O , versus integration step-size for single-site methanol rearrangment runs. The vertical line in the figure denotes the time-step value that was used in the remaining simulation runs.

## References


[1] Bromberg, S. E., Yang, H., Asplund, M. C., Lian, T., McNamara, B. K., Kotz, K. T., Yeston, J. S., Wilkens, M., Frei, H., Bergman, R. G. and Harris, C. B. "The Mechanism of a C-H bond Activation Reaction in Room-Temperature Alkane Solution." *Science* **1997**, *278 (5336)*, 260-263.

[2] Yang, H. "Ultrafast Infrared Studies of Chemical Reaction Dynamics in Room-temperature Liquids", Ph.D. Dissertation, University of California, Berkeley, **1999**.

[3] Yang, H., Asplund, M. C., Kotz, K. T., Wilkens, M. J., Frei, H. and Harris, C. B. "Reaction Mechanism of Silicon-Hydrogen Bond Activation Studied Using Femtosecond to Nanosecond IR Spectroscopy and Ab Initio Methods." *J. Am. Chem. Soc.* **1998**, *120 (39)*, 10154-10165.

[4] Kotz, K. T., Yang, H., Snee, P. T., Payne, C. K. and Harris, C. B. "Femtosecond Infrared Studies of Ligand Rearrangement Reactions: Silyl Hydride Products from Group 6 Carbonyls." *J. Organomet. Chem.* **2000**, *596 (1-2)*, 183-192.

[5] Backus, S., Dufree III, C. G., Murnane, M. M. and Kapteyn, H. C. "High Power Ultrafast Lasers." *Rev. Sci. Instrum.* **1998**, *69 (3)*, 1207-1223.

[6] Jetz, W. and Graham, W. A. G. "Silicon-Transition Metal Chemistry. I. Photochemical Preparation of Silyl(Transition Metal) Hydrides." *Inorg. Chem.* **1970**, *10*, 4-9.

[7] Wrighton, M. and Schroeder, M. A. "Structure and Reactivity Relationships in Chromium Carbonyl Photoassisted Hydorgenation of 1,3 Dienes." *J. Am. Chem. Soc.* **1973**, *95*, 5764-5765.

[8] Wrighton, M. and Schroeder, M. A. "Chromium Carbonyl Photocatalyzed 1,4-Hydrosilation of 1,3-Dienes. A Synthesis of Allylsilanes." *J. Am. Chem. Soc.* **1974**, *96*, 6235-6237.

[9] Arndtsen, B. A., Bergman, R. G., Mobley, T. A. and Peterson, T. H. "Selective Intermolecular Carbon-Hydrogen Bond Activation By Synthetic Metal Complexes in Homogeneous Solution." *Acc. Chem. Res.* **1995**, *28 (3)*, 154-162.

[10] Geoffroy, G. L. and Wrighton, M. S.: *Organometallic Photochemistry*; Academic Press: New York, NY; **1979**; pp. 257.

[11] Lian, T. Q., Bromberg, S. E., Asplund, M. C., Yang, H. and Harris, C. B. "Femtosecond Infrared Studies of the Dissociation and Dynamics of Transition Metal Carbonyls in Solution." *J. Phys. Chem.* **1996**, *100 (29)*, 11994-12001.

[12] Joly, A. G. and Nelson, K. A. "Metal Carbonyl Photochemistry in Organic Solvents - Femtosecond Transient Absorption and Preliminary Resonance Raman Spectroscopy." *Chem. Phys.* **1991**, *152 (1-2)*, 69-82.

[13] Joly, A. G. and Nelson, K. A. "Femtosecond Transient Absorption-Spectroscopy of $Cr(CO)_6$ in Methanol - Observation of Initial Excited-States and CO Dissociation." *J. Phys. Chem.* **1989**, *93*, 2876-2878.

[14] Simon, J. D. and Xie, X. "Time-Resolved Studies of Solvation: The Photodissociation of $Cr(CO)_6$ in Pentanol." *J. Phys. Chem.* **1987**, *91*, 5538-5540.

[15] Simon, J. D. and Xie, X. "Photodissociation of $Cr(CO)_6$ in Solution: Direct Observation of the Formation of $Cr(CO)_5(MeOH)$." *J. Phys. Chem.* **1986**, *90*, 6751-6753.

[16] Morse, J. M., Parker, G. H. and Burkey, T. J. "Enthalpy of CO Dissociation from $M(CO)_6$ (M=Cr, Mo,W)

in Alkane Solvent: Determination of Intermolecular Agostic Bond Strengths." *Organometallics* **1989**, *8*, 2471-2474.

[17] Yu, S.-C., Xu, X., Lingle, R. and Hopkins, J. B. ."The Role of Vibrational Energy in the Ultrafast Photodissociation of $Cr(CO)_6$." *J. Am. Chem. Soc.* **1990**, *112*, 3668-3669.

[18] Xie, X. and Simon, J. D. "Photodissociation of $Cr(CO)_6$ in 1-Propanol and 2-Propanol: Effect of Solvent Structure on the Mechanism of $Cr(CO)_5(OHR)$ from Photogenerated $Cr(CO)_5(ROH)$." *J. Am. Chem. Soc.* **1989**, *93*, 291-293.

[19] Xie, X. and Simon, J. D. "Picosecond Time-Resolved Absorption Studies of the Solvation of $Cr(CO)_5$ in Alcohols: A Unimolecular Kinetic Model for the Formation of $Cr(CO)_5(OHR)$ from Photogenerated $Cr(CO)_5(ROH)$." *J. Am. Chem. Soc.* **1990**, *112*, 1130-1136.

[20] Burkey, T. J. "Thermochemistry of Silane Substitution of CO on Metal Carbonyl Complexes. Interaction of Silanes with Metal Centers." *J. Am. Chem. Soc.* **1990**, *112 (23)*, 8329-8333.

[21] Zhang, S., Dobson, G. R. and Brown, T. L. "Flash-Photolysis Studies of the Photochemical Reactions of Silanes with Cromium Hexacarbonyl." *J. Am. Chem. Soc.* **1991**, *113 (18)*, 6908-6916.

[22] Zhang, S. L., Zang, V., Bajaj, H. C., Dobson, G. R. and Vaneldik, R. "Octahedral Metal Carbonyls .72. Volumes of Activation For Solvent Displacement in (Solvent)$Cr(CO)_5$, (Solvent)$Mo(CO)_5$, (Solvent)$W(CO)_5$ Transients Generated from $M(CO)_6$ via Pulsed Laser Flash Photolysis." *J. Organomet. Chem.* **1990**, *397 (3)*, 279-289.

[23] Zhang, S. and Dobson, G. R. "Octahedral Metal Carbonyls .70. Competitive Mechanisms for Displacement by 1-Hexene of Normal-Heptane from the Photogenerated [(Normal-Heptane)$Cr(Co)_5$] Transient." *Inorg. Chim. Acta.* **1989**, *165 (1)*, 11-12.

[24] Zhang, S. L. and Dobson, G. R. "Octahedral Metal Carbonyls .74. Estimates of Solvent Metal Bond Strengths in (Solvent)$M(Co)_5$ Complexes (Solvent = Benzene (M = Mo, W) and Tetrachloromethane (M = Cr))." *Inorg. Chim. Acta.* **1991**, *181 (1)*, 103-109.

[25] Zhang, S., Bajaj, H. C., Zang, V., Dobson, G. R. and Vaneldik, R. "Volumes of Activation for Solvent

Displacement Reactions on Pentacarbonylchromium(0) - Comparison of Data for Pure and Mixed Solvents." *Organometallics* **1992**, *11 (11)*, 3901-3903.

[26] Zhang, S. L. and Dobson, G. R. "Octahedral Metal Carbonyls .79. Mechanism of the Reaction of Photogenerated (Solvent)$Cr(CO)_5$ Intermediates With Lewis Bases (L) in Binary and Ternary Solvent/L Mixtures (Solvent = Fluorobenzene, Chlorobenzene, Normal-Heptane - L = 1-Hexene, Piperidine)." *Organometallics* **1992**, *11 (7)*, 2447-2452.

[27] Ladogana, S., Nayak, S. K., Smit, J. P. and Dobson, G. R. "The Kinetics and Mechanism of Ligand Exchange in Photogenerated ($\eta^1$-bromobenzene)$Cr(CO)_5$/alkene Systems." *Inorg. Chim. Acta.* **1998**, *267 (1)*, 49-54.

[28] Ladogana, S., Nayak, S. K., Smit, J. P. and Dobson, G. R. "Mechanism of Linkage Isomerization in ($\eta^1$-5-chloropentene)pentacarbonylchromium(0)." *Inorg. Chem.* **1997**, *36 (4)*, 650-655.

[29] Dobson, G. R., Asali, K. J., Cate, C. D. and Cate, C. W. "Octahedral Metal Carbonyls .78. Mechanism of Alkane Displacement by 1-Hexene from (Alkane)$W(CO)_5$ Complexes (Alkane=Cyclohexane, N-Heptane) -

Estimates of the Alkane-W Bond Strengths in Condensed Media." *Inorg. Chem.* **1991**, *30 (23)*, 4471-4474.

[30] Dobson, G. R. and Zhang, S. L. "Mechanism of Displacement of Alkanes from Photogenerated (alkane) $Cr(CO)_5$ Complexes." *J. Coord. Chem.* **1999**, *47 (3)*, 409-416.

[31] Rector, K. D., Kwok, A. S., Ferrante, C., Tokmakoff, A., Rella, C. W. and Fayer, M. D. "Vibrational Anharmonicity and Multilevel Vibrational Dephasing from Vibrational Echo Beats." *J. Chem. Phys.* **1997**, *106 (24)*, 10027-10036.

[32] Myers, D. J., Urdahl, R. S., Cherayil, B. J. and Fayer, M. D. "Temperature Dependence of Vibrational Lifetimes at the Critical Density in Supercritical Mixtures." *J. Chem. Phys.* **1997**, *107 (23)*, 9741-9748.

[33] Asbury, J. B., Ghosh, H. N., Yeston, J. S., Bergman, R. G. and Lian, T. Q. "Sub-Picosecond IR Study of the Reactive Intermediate in an Alkane C-H Bond Activation Reaction by $CpRh(CO)_2$." *Organometallics* **1998**, *17 (16)*, 3417-3419.

[34] Lian, T., Bromberg, S. E., Yang, H., Proulx, G., Bergman, R. G. and Harris, C. B. "Femtosecond IR

Studies of Alkane C-H Bond Activation By Organometallic Compounds - Direct Observation of Reactive Intermediates in Room Temperature Solutions." *J. Am. Chem. Soc.* **1996**, *118 (15)*, 3769-3770.

[35] Yang, H., Kotz, K. T., Asplund, M. C. and Harris, C. B. "Femtosecond Infrared Studies of Silane Silicon-Hydrogen Bond Activation." *J. Am. Chem. Soc.* **1997**, *119 (40)*, 9564-9565.

[36] Yang, H., Kotz, K. T., Asplund, M. C., Wilkens, M. J. and Harris, C. B. "Ultrafast Infrared Studies of Bond Activation in Organometallic Complexes." *Acc. Chem. Res.* **1999**, *32 (7)*, 551-560.

[37] George, M. W., Dougherty, T. P. and Heilweil, E. J. "UV Photochemistry of $[CpFe(CO)_2]_2$ ($Cp=\eta^5-C_5H_5$) Studied by Picosecond Time-Resolved Infrared Spectroscopy." *J. Phys. Chem.* **1996**, *100 (1)*, 201-206.

[38] Grubbs, W. T., Dougherty, T. P. and Heilweil, E. J. "Vibrational Energy Redistribution in $Cp^*-Ir(CO)_2$ ($Cp^*=\eta^5$-Pentamethylcyclopentadienyl) Studied by Broadband Transient Infrared Spectroscopy." *Chem. Phys. Lett.* **1994**, *227 (4-5)*, 480-484.

[39] Dougherty, T. P. and Heilweil, E. J. "Ultrafast Transient Infrared Absorption Studies of $M(CO)_6$ (M=Cr, Mo or W) Photoproducts in n-Hexane Solution." *Chem. Phys. Lett.* **1994**, *227 (1-2)*, 19-25.

[40] Dougherty, T. P., Grubbs, W. T. and Heilweil, E. J. "Photochemistry of $Rh(CO)_2$(Acetylacetonate) and Related Metal Dicarbonyls Studied by Ultrafast Infrared Spectroscopy." *J. Phys. Chem.* **1994**, *98 (38)*, 9396-9399.

[41] Dougherty, T. P. and Heilweil, E. J. "Transient Infrared Spectroscopy of $(\eta^5\text{-}C_5H_5)Co(CO)_2$ Photoproduct Reactions in Hydrocarbon Solutions." *J. Chem. Phys.* **1994**, *100 (5)*, 4006-4009.

[42] Bethune, D. S. "Dye Cell Design for High-Power Low-Divergence Excimer-Pumped Dye-Laser." *Appl. Opt.* **1981**, *20*, 1987.

[43] Bard, Y.: *Nonlinear Parameter Estimation*; Academic Press: Orlando, FL; **1974**; pp. 341.

[44] Press, W. H., Teukolsky, S. A., Vetterling, W. T. and Flannery, B. P.: *Numerical Recipies in C*; 2nd ed.; Cambridge University Press: New York, NY; **1994**; pp. 994.

[45] Efron, B. and Tibshirani, R. J.: *An Introduction to the Bootstrap*; Chapman & Hall: New York; **1993**; pp. 436.

[46] Arrivo, S. M., Dougherty, T. P., Grubbs, W. T. and Heilweil, E. J. "Ultrafast Infrared Spectroscopy of Vibrational Co-Stretch Up-Pumping and Relaxation Dynamics of $W(CO)_6$." *Chem. Phys. Lett.* **1995**, *235 (3-4)*, 247-254.

[47] Hamm, P., Ohline, S. M. and Zinth, W. "Vibrational Cooling after Ultrafast Photoisomerization of Azobenzene Measured by Femtosecond Infrared Spectroscopy." *J. Chem. Phys.* **1997**, *106 (2)*, 519-529.

[48] Schubert, U., Müller, J. and Alt, H. G. "Hydrido Silyl Complexes. 9. Cr, H, Si Three-Center Bonding in $C_6Me_6(CO)_2Cr(H)SiHPh_2$." *Organometallics* **1987**, *6 (3)*, 469-472.

[49] Hay, P. J. "Electronic States of $Cr(CO)_5$." *J. Am. Chem. Soc.* **1979**, *100*, 2411-2417.

[50] Snee, P. T., Yang, H., Kotz, K. T., Payne, C. K. and Harris, C. B. "Ultrafast Infrared Studies of the Reaction Mechanism of Silicon-Hydrogen Bond

Activation by $\eta^5$-CpV(CO)$_4$." *J. Phys. Chem. A* **1999**, *103 (49)*, 10426-10432.

[51] Snee, P. T., Payne, C. K., Kotz, K. T., Yang, H. and Harris, C. B. "Triplet Organometallic Reactivity under Ambient Conditions: An Ultrafast UV Pump/IR Probe Study." *J. Am. Chem. Soc.* **2001**, *123 (10)*, 2255-2264.

[52] Simon, J. D. and Peters, K. S. "Picosecond Photochemistry of Cr(CO)$_6$: Solvation and Dynamics of the Primary Intermediate." *Chem. Phys. Lett.* **1983**, *98*, 53-56.

[53] Hill, R. H. and Wrighton, M. S. "Oxidative Addition of Trisubstituted Silanes to Photochemically Generated Coordinatively Unsaturated Species ($\eta^4$-$C_4H_4$)Fe(CO)$_2$, ($\eta^5$-$C_5H_5$)Mn(CO)$_2$, and ($\eta^6$-$C_6H_6$)Cr(CO)$_2$ and Related Molecules." *Organometallics* **1987**, *6 (3)*, 632-638.

[54] Hill, R. H. and Palmer, B. J. "Mechanism of the Photochemical Cis Trans Isomerism of ($\eta^5C_5Me_5$)Re(CO)$_2$me$_2$, ($\eta^5C_5Me_5$)Re(CO)$_2$Cl$_2$, ($\eta^5C_5Me_5$)Re(CO)$_2$Br$_2$, ($\eta^5C_5Me_5$)Re(CO)$_2$I$_2$." *Organometallics* **1989**, *8 (7)*, 1651-1655.

[55] Yang, P.-F. and Yang, G. K. "Haloalkanes as Ligands. Spectroscopic and Energetic Studies of $CpMn(CO)_2XR$." *J. Am. Chem. Soc.* **1992**, *114*, 6937-6938.

[56] Sun, X. Z., Grills, D. C., Nikiforov, S. M., Poliakoff, M. and George, M. W. "Remarkable Stability of $(\eta^5\text{-}C_5H_5)Re(CO)_2L$ (L equals n-heptane, Xe, and Kr): A Time-Resolved Infrared Spectroscopic Study of $(\eta^5\text{-}C_5H_5)Re(CO)_3$ in Conventional and Supercritical Fluid Solution." *J. Am. Chem. Soc.* **1997**, *119 (32)*, 7521-7525.

[57] Klassen, J. K., Selke, M., Sorensen, A. A. and Yang, G. K. "Metal-Ligand Bond Dissociation Energies in $CpMn(CO)_2L$ Complexes." *J. Am. Chem. Soc.* **1990**, *112*, 1267-1268.

[58] Zaric, S., Couty, M. and Hall, M. B. "Ab Initio Calculations of the Geometry and Vibrational Frequencies of the Triplet State of Tungsten Pentacarbonyl Amine: A Model for the Unification of the Preresonance Raman and the Time-Resolved Infrared Experiments." *J. Am. Chem. Soc.* **1997**, *119 (12)*, 2885-2888.

[59] Yang, G. K., Vaida, V. and Peters, K. S. "Application of Time-Resolved Photoacoustic

Calorimetry to Cr-L Bond Enthalpies in $Cr(CO)_5$-L." *Polyhedron* **1988**, *7 (16/17)*, 1619-1622.

[60] Lewis, K. E., Golden, D. M. and Smith, G. P. "Organometallic Bond Dissociation Energies: Laser Pyrolysis of $Fe(CO)_5$, $Cr(CO)_5$, $Mo(CO)_5$, and $W(CO)_6$." *J. Am. Chem. Soc.* **1984**, *106 (14)*, 3905-3912.

[61] Kramers, H. A. "Brownian Motion in a Field of Force and the Diffusion Model of Chemical Reactions." *Physica* **1940**, *7*, 284.

[62] Hänggi, P., Talkner, P. and Borkovec, M. "Reaction-rate Theory: Fifty Years after Kramers." *Rev. Mod. Phys.* **1990**, *62 (2)*, 251-341.

[63] McQuarrie, D. A.: *Statistical Mechanics*; Harper & Row: New York; **1976**; pp. 641.

[64] Payne, C. K., Snee, P. T., Yang, H., Kotz, K. T., Schafer, L. L., Tilley, T. D. and Harris, C. B. "Intramolecular Rearrangements on Ultrafast Timescales: Femtosecond Infrared Studies of Ring Slip in $(\eta^1\text{-}C_5Cl_5)Mn(CO)_5$." *J. Am. Chem. Soc.* **2001**, *123 (30)*, 7425-7426.

[65] *Jaguar 3.5;* Schroedinder, Inc.: Portland, OR, 1998

[66] Becke, A. D. "Density-Functional Thermochemistry. 3. The Role of Exact Exchange." *J. Chem. Phys.* **1993**, *98 (7)*, 5648-5652.

[67] Lee, C. T., Wang, W. T. and Parr, R. G. "Development of the Colle-Salvetti Correlation-Energy Formula into a Functional of the Electron-Density." *Phys. Rev. B* **1988**, *37 (2)*, 785-789.

[68] Stephens, P. J., Devlin, F. J., Chabalowski, C. F. and Frisch, M. J. "Ab Initio Calculation of Vibrational Absorption and Circular Dichroism Spectra Using Density Functional Force Fields." *J. Phys. Chem.* **1994**, *98 (45)*, 11623-11627.

[69] Glukhovtsev, M. N., Bach, R. D. and Nagel, C. J. "Performance of the B3LYP/ECP DFT Calculations of Iron-Containing Compounds." *J. Phys. Chem. A* **1997**, *101 (3)*, 316-323.

[70] Ricca, A. and Bauschlicher, C. W. "A Comparison of Density Functional Theory with Ab Initio Approaches for Systems Involving First Transition Row Metals." *Theor. Chim. Acta* **1995**, *92 (2)*, 123-131.

[71] Schmidt, M. W., Baldridge, K. K., Boatz, J. A., Elbert, S. T., Gordon, M. S., Jensen, J. H., Koseki, S., Matsunaga, N., Nguyen, K. A., Su, S. J., Windus,

T. L., Dupuis, M. and Montgomery, J. A. "General Atomic and Molecular Electronic Structure System." *J. Comput. Chem.* **1993**, *14 (11)*, 1347-1363.

[72] Francl, M. M., Pietro, W. J., Hehre, W. J., Binklet, J. S., Gordon, M. S., Defrees, D. J. and Pople, J. A. "Self-Consistent Molecular-Orbital Methods. 23. A Polarization-Type Basis Set for 2nd-Row Elements." *J. Chem. Phys.* **1982**, *77 (7)*, 3654-3665.

[73] Hay, P. J. and Wadt, W. R. "Abinitio Effective Core Potentials for Molecular Calculations - Potentials for K to Au Including the Outermost Core Orbitals." *J. Chem. Phys.* **1985**, *82 (1)*, 299-310.

[74] Hehre, W. J., Ditchfield, R. and Pople, J. A. "Self-Consistent Molecular-Orbital Methods. 12. Further Extensions of Gaussian-Type Basis Sets for Use in Molecular-Orbital Studies of Organic-Molecules." *J. Chem. Phys.* **1972**, *56 (5)*, 2257-2261.

[75] Xantheas, S. S. "On the Importance of the Fragment Relaxation Energy Terms in the Estimation of the Basis Set Superposition Error Correction to the Intermolecular Interaction Energy." *J. Chem. Phys.* **1996**, *104 (21)*, 8821-8824.

[76] Zaric, S. and Hall, M. B. "Ab Initio Calculation of the Geometries and Bonding Energies of Alkane and Fluoroalkane Complexes with Tungsten Pentacarbonyl." *J. Phys. Chem. A* **1997**, *101 (25)*, 4646-4652.

[77] Wagner, C. and Kiefhaber, T. "Intermediates Can Accelerate Protein Folding." *Proc. Natl. Acad. Sci. USA* **1999**, *96*, 6716-6721.

[78] Edwards, D. M. F., Madden, P. A. and McDonald, I. R. "A Computer Simulation Study of the Dielectric Properties of a Model of Methyl Cyanide." *Mol. Phys.* **1984**, *51 (5)*, 1141-1161.

[79] Allen, M. P. "Brownian Dynamics Simulation of a Chemical Reaction in Solution." *Mol. Phys.* **1980**, *40 (5)*, 1073-1087.

[80] Allen, M. P. and Tildesley, D. J.: *Computer Simulations of Liquids*; Oxford University Press: New York; **1994**; pp. 385.

[81] Beeman, D. "Some Multistep Methods for Use in Molecular-Dynamics Calculations." *J. Comput. Phys.* **1976**, *20 (2)*, 130-139.

[82] Hansen, J. P. and McDonald, I. R.: *Theory of Simple Liquids*; 2nd ed.; Academic Press Inc.: London; **1986**; pp. 556.

[83] Bauer, D. R., Brauman, J. I. and Pecora, R. "Molecular Reorientations in Liquids. Experimental Test of Hydrodynamic Models." *J. Am. Chem. Soc.* **1974**, *96 (22)*, 6840-6843.

[84] Waldeck, D. H., Lotshaw, W. T., McDonald, D. R. and Fleming, G. R. "Ultraviolet Picosecond Pump-Probe Spectroscopy with a Synchronously Pumped Dye Laser. Rotational Diffusion of Diphenyl Butadiene." *Chem. Phys. Lett.* **1982**, *88 (3)*, 297-300.

[85] *CRC Handbook of Chemistry and Physics*; 74th ed.; Lide, D. R., Ed.; CRC Press: Boca Raton, FL, **1994**.

[86] Viswanath, D. S. and Natarajan, G.: *Data Book on the Viscosity of Liquids*; Hemisphere Publishing Corporation: New York; **1989**; pp. 990.

[87] Straub, J. E., Borkovec, M. and Berne, B. J. "Non-Markovian Activated Rate Processes: Comparison of Current Theories with Numerical Simulation Data." *J. Chem. Phys.* **1986**, *84 (3)*, 1788-1794.

[88] Lindsey, C. P. and Patterson, G. D. "Detailed Comparison of the Williams-Watts and Cole-Davidson Functions." *J. Chem. Phys.* **1980**, *73 (7)*, 3348-3357.

[89] Klimov, D. K. and Thirumalai, D. "Viscosity Dependence of the Folding Rates of Proteins." *Phys. Rev. Lett.* **1997**, *79 (2)*, 317-320.

[90] *Ultrashort Laser Pulses. Generation and Applications*; 2nd. ed.; Kaiser, W., Ed.; Springer-Verlag: New York, **1993**; Vol. 60, pp. 492.

[91] Harris, A. L. "Picosecond Spectroscopy of Chemical Reactions in Liquids", Ph.D. Dissertation, University of California, Berkeley, **1985**.

[92] Koechner, W.: *Solid-state Laser Engineering*; 5 ed.; Springer: New York; **1999**.

[93] Squier, J., Salin, F., Mourou, G. and Harter, D. "100-fs Pulse Generation and Amplification in Ti:$Al_2O_3$." *Opt. Lett.* **1991**, *16 (5)*, 324-326.

[94] Martinez, O. E. "3000 Times Grating Compressor with Positive Group Velocity Dispersion: Application to Fiber Compensation in 1.3-1.6 μm Region." *IEEE J. Quantum Electron.* **1987**, *QE-23 (1)*, 59-64.

[95] Treacy, E. B. "Optical Pulse Compression with Diffraction Gratings." *IEEE J. Quantum Electron.* **1969**, *QE-5 (9)*, 454-458.

[96] Hunziker, L. E. "Femtosecond Measurements of Gas Temperatures Using Raman Induced Polarization

Spectroscopy", Ph.D. Dissertation, University of California, Berkeley, **1997**.

[97] Spence, D. E., Kean, P. N. and Sibbett, W. "60-fsec Pulse Generation from a Self-mode-Locked Ti-sapphire Laser." *Opt. Lett.* **1991**, *16 (1)*, 42.

[98] Murnane, M. M., Kapteyn, H. C., Huang, C. P., Asaki, M. T. and Garvey, D. *Mode-Locked Ti:Sapphire Laser. Designs and Guidelines for Constructing a Mode-Locked Ti:Sapphire Laser.* Rev. 1.6. Washington State University: Pullman, WA; 1992; pp. 32.

[99] *Ultrashort Laser Pulse Phenomena. Fundamentals, Techniques, and Applications on a Femtosecond Time Scale*; ed.; Diels, J.-C. and Rudolph, W., Eds.; Academic Press: New York, **1996**;, pp. 581.

[100] Le Blanc, C., Baubeau, E., Salin, F., Squier, J. A., Barty, C. P. J. and Spielmann, C. "Toward a Terawatt-Kilohertz Repetition-Rate Laser." *IEEE J. Quantum Electron.* **1998**, *4 (2)*, 407-413.

[101] Lemoff, B. E. and Barty, C. P. J. "Quintic-phase-limited, Spatially Uniform Expansion and Recompression of Ultrashort Optical Pulses." *Opt. Lett.* **1993**, *18 (19)*, 1651-1653.

[102] Martinez, O. E., Gordon, J. P. and Fork, R. L. "Negative Group-velocity Dispersion Using Refraction." *J. Opt. Soc. Am. A* **1984**, *1 (10)*, 1003-1006.

[103] Martinez, O. E. "Grating and Prism Compressors in the Case of Finite Beam Size." *J. Opt. Soc. Am. B* **1986**, *3 (7)*, 929-934.

[104] Barty, C. P. J., Guo, T., Le Blanc, C., Raksi, F., Rose-Petruck, C., Squier, J., Wilson, K. R., Yakovlev, V. V. and Yamakawa, K. "Generation of 18-fs, Multiterawatt Pulses by Regenerative Pulse Shaping and Chirped-Pulse Amplification." *Opt. Lett.* **1996**, *21 (9)*, 668-670.

[105] Joo, T., Jia, Y. and Fleming, G. R. "Ti:sapphire Regenerative Amplifier for Ultrashort High-power Multikilohertz Pulses without an External Stretcher." *Opt. Lett.* **1995**, *20 (4)*, 389-391.

[106] Wynne, K., Reid, G. D. and Hochstrasser, R. M. "Regenerative Amplification of 30-fs Pulses in Ti:sapphire at 5 kHz." *Opt. Lett.* **1994**, *19 (12)*, 895-897.

[107] Kuizenga, D. J. *"Intra-cavity Beam Relay for Optical Harmonic Generation"* Patent #5,025,446, Laserscope, U.S.A, **1991**.

[108] Hunt, J. T., Glaze, J. A., Simmons, W. W. and Renard, P. A. "Suppression of Self-focusing through Low-Pass Spatial Filtering and Relay Imaging." *Appl. Opt.* **1978**, *17 (13)*, 2053-2057.

[109] Zhou, J., Huang, C.-P., Shi, C., Murnane, M. M. and Kapteyn, H. C. "Generation of 21-fs Millijoule-energy Pulses by Use of Ti:sapphire." *Opt. Lett.* **1994**, *19 (2)*, 126-128.

[110] Zhou, J., Huang, C.-P., Murnane, M. M. and Kapteyn, H. C. "Amplification of 26-fs, 2-TW Pulses near the Gain-Narrowing Limit in Ti:Sapphire." *Opt. Lett.* **1995**, *20 (1)*, 64-66.

[111] Le Blanc, C., Grillon, G., Chambaret, J. P., Migus, A. and Antonetti, A. "Compact and Efficient Multipass Ti:sapphire System for Femtosecond Chirped-pulse Amplification at the Terawatt Level." *Opt. Lett.* **1993**, *18 (2)*, 140-142.

[112] Lenzner, M., Spielmann, C., Wintner, E., Krausz, F. and Schmidt, A. J. "Sub-20-fs, Kilohertz-

Repetition-Rate Ti:sapphire Amplifier." *Opt. Lett.* **1995**, *20 (12)*, 1397-1399.

[113] Reid, G. D., Personal Communication. Ti:sapphire Regenerative Amplifier Construction Diagram.

[114] Moulton, P. F. "Spectroscopic and Laser Characteristics of Ti:$Al_2O_3$." *J. Opt. Soc. Am. B* **1986**, *3 (1)*, 125-132.

[115] Chandrasekhar, S. "Stochastic Problems in Physics and Astronomy." *Rev. Mod. Phys.* **1943**, *15*, 1-89.

ERNEST ORLANDO LAWRENCE BERKELEY NATIONAL LABORATORY
ONE CYCLOTRON ROAD | BERKELEY, CALIFORNIA 94720

Prepared for the U.S. Department of Energy under Contract No. DE-AC03-76SF00098

ACE270
LBL Libraries